Università degli Studi di Padova

Dipartimento di Ingegneria Civile, Edile e Ambientale

Scuola di Dottorato di Ricerca

in Scienze dell'Ingegneria Civile e Ambientale

XXXVI Ciclo

FATIGUE AND CYCLIC LOADINGS IN CONCRETE MATERIALS

Coordinator: *Prof. Massimiliano Ferronato*

Supervisor: *Prof. Gianluca Mazzucco*

Co-Supervisor: *Dr. Beatrice Pomaro*

Ph.D. student : *Dongmo Beaudin Freinrich*

ACKNOWLEDGEMENT

First and foremost, I wish to thank my supervisor **Prof. Gianluca Mazzucco**. It is an honor to be one of his PhD students. He has taught me with dedication, since the very beginning. I am grateful to him for his contributions and his tireless guidance. Without him, this work could not be accomplished. I would like to thank my co-supervisor **Dr. Beatrice Pomaro**, for the continuous support and encouragements during the three years.

I would like to thank **Prof. Carmelo Maiorana** and **Prof. Esoh Elame**, for guiding me through my academic and professional careers since my postgraduate studies.

I would like to thank **Prof. Valentina Salomoni** and all the members of our research group for their continuous presence and support. They have been a source of collaboration, as well as friendship.

Last but not least, I would like to thank my friends and my family for all their love and encouragement.

Summary

The goal of the work is to propose a robust 3D constitutive model of concrete, based on existing plasticity and damage models, which are extended to include long-term effects and fatigue behaviour. Specifically, the accumulation of plastic strains inside the complex heterogeneous structure of concrete materials, is considered as the main physical mechanism underlying the non-linear creep behaviour and the fatigue degradation. Moreover, the proposed model must account for non-linear characteristics of concrete materials, such as permanent deformations, stiffness degradation and recovery, pressure dependency, and stress concentration effects in a unified manner.

To this aim, in a first step, plasticity and continuum damage mechanics are coupled altogether with a creep model to account for long-term effects. Then the plastic-damage model is extended to account for fatigue behaviour. In the coupled model, the fatigue failure is explained by the progressive accumulation of inelastic strains and the evolution of micro-cracks, as the size of the elastic domain decreases. In particular, the constitutive model allows for plastic flow and damage accumulation, even for stress states initially below the yield surface.

The plastic-damage model considers the pressure dependent Ménétrey-Willam yield surface, extended to incorporate a scalar damage variable which is responsible for the reduction in size of the yield surface as the material undergoes damage. In order to account for the different damage mechanisms in tension and compression, two different damage components are defined using exponential laws as suggested by Mazars, for both tension and compression. A stiffness recovery function is defined to catch the increase of stiffness due to the closure of cracks as the mechanical load reverses from tension to compression. The creep formulation of the model considers the B3 model

of Bažant and Baweja, in which aging is incorporated through the solidification theory. In order to account for fatigue degradation and accumulation, even for stress state initially below the yield surface, a modified formulation of the Ménétrey-Willam yield surface is proposed in this work. The proposed fatigue model considers an extension of the modified Ménétrey-Willam yield function, to include a fatigue degradation function that represents the effects of the cumulative and irreversible micro-structural degradation as the number of cycles increases. An appropriate internal variable for fatigue is selected, in order to allow for strength degradation for stress states initially below the yield surface.

The numerical implementation of each component of the model and their coupling are discussed. In particular, the plastic-damage and fatigue component is implemented considering a two-step algorithm, with an elastic-predictor step, followed by a plastic correction. On the other side, the creep model is implemented by means of the exponential algorithm proposed by Bažant. The coupling is done assuming a scenario in which the load increment is applied instantaneously at the beginning of the time interval into consideration. Then, The derivation of the elasto-plastic consistent tangent operator and, of the visco-elasto-plastic constitutive tangent operator are discussed. A "return to apex" procedure is described to account for situations in which the return-mapping vector does not intersect the yield surface.

Each component of the model is calibrated and validated against experimental results. Specifically, the plastic-damage model has been calibrated and validated against tri-axial compression tests, considering different levels of confinement. The calibration and validation of the creep model requires the determination of the number of Kelvin units for the basic and drying creep components of the B3 model, for a more accurate reproduction of creep curves. With regards to the fatigue model, the effects of the stress range and of the confinement level in multi-axial stress states were assessed in the fatigue response of concrete materials, by considering relevant experimental tests from the literature. The proposed model is able to catch non-linear features of the mechanical behaviour of concrete such as the stiffness degradation and post-peak softening behaviour. Furthermore, it can reproduce the experimental three-stage pattern of the fatigue curves, for concrete specimen subjected to multi-axial stress conditions.

Then experimental tests were performed at the meso-scale, in which the coarse aggregates and the cement matrix are differentiated.Interestingly, a principal aspect of the proposed model is its capability to account for local material deterioration at the meso-scale, even when the macro-mechanical load is below the yield limit. In particular, by studying the interaction between the aggregates and the cement matrix at the meso-scale, it comes out that the proposed model is able to account for non-linear creep or tertiary stage creep, which is not included in the B3 model of Bažant and Baweja, and without considering additional parameters related to creep. This can be attributed to the growth and coalescence of plastic regions that develop at the interface between the stiffer aggregates and the creeping mortar. The tests performed at the meso-scale of the coupled model prove the soundness of the proposed model to reproduce the non-linear mechanical behaviour of concrete subjected to generic 3D stress states under monotonic, creep and fatigue loadings.

NOMENCLATURE

a	=	slope of the fatigue degradation function;
A, B	=	constant parameters of the plastic potential function;
A_c, B_c	=	calibration parameters in compression of the Mazars' damage model;
A_t, B_t	=	calibration parameters in tension of the Mazars' damage model;
$C_0(t,t'), C_d(t,t',t_0)$	=	basic and drying creep terms, respectively, of the B3 model;
$\boldsymbol{D}^{ep}$	=	elasto-plastic tangent operator;
$\boldsymbol{D}^{ve}$	=	visco-elastic tangent operator;
$\boldsymbol{D}^{vep}$	=	visco-elasto-plastic tangent operator;
E	=	stiffness modulus;
E_μ	=	stiffness modulus of the spring of the μ-th Kelvin unit;
e	=	material eccentricity;
f	=	yield surface;
f_c	=	compression strength;
f_t	=	tensile strength;
g_p	=	plastic potential;
G_f	=	fracture energy;
h	=	spatial average of pore relative humidity;
I	=	identity tensor in Voigt notation: $[1,1,1,0,0,0]^T$;
I_1	=	first invariant of the stress tensor;
J_2, J_3	=	second and third invariants of the deviatoric stress tensor;
$J(t,t^{'})$	=	creep compliance function;
l_c	=	characteristic length;
m	=	number of Kelvin units for basic creep;
m_d	=	number of Kelvin units for drying creep;
q	=	hardening/softening parameter $q = q_h q_s$;
q_1, q_2, q_3, q_4, q_5	=	constant parameters of the B3 creep model;
q_h	=	hardening parameter;
q_{h0}	=	initial value of the hardening parameter;

q_f = fatigue degradation function;

q_s = softening parameter;

$Q(t,t^{'})$ = aging visco-elastic function of the B3 creep model;

r = elliptic function controlling the shape of the yield surface;

s_0 = initial value of the stiffness recovery function;

s_{ij} = deviatoric stress tensor components;

t = current age of concrete;

t' = loading age of concrete;

t_0 = time at which drying of concrete starts;

t_s = softening slope;

V^e = volume of the finite element;

w_c = crack band width;

$\boldsymbol{\varepsilon}^p$ = plastic strain tensor;

$\boldsymbol{\varepsilon}^{ve}$ = visco-elastic strain tensor;

δ = Kronecker delta $(\delta_{ij} = 1 \text{ if } i = j;\ \delta_{ij} = 0 \text{ if } i \neq j)$;

ε = uniaxial strain;

$\boldsymbol{\varepsilon}^c$ = creep strain tensor;

ε_{creep} = uniaxial creep strain;

$\boldsymbol{\varepsilon}^e$ = elastic strain tensor;

η_μ = viscosity of the dashpot of the μ-th Kelvin unit;

κ = equivalent plastic strain (volumetric plastic strain);

κ_c = equivalent plastic strain for compression damage;

κ_{c0} = initial value of the equivalent plastic strain for compression damage;

κ_f = crack band equivalent plastic strain;

κ_t = equivalent plastic strain for tension damage;

κ_{t0} = initial value of the equivalent plastic strain for tension damage;

κ_{1D} = plastic volumetric strain at maximum compression load in uniaxial condition;

γ_f = internal variable foe fatigue evolution;

γ_t = threshold value of $gamma_f$ for fatigue activation;

$\dot{\gamma}$	=	plastic multiplier;
σ	=	uniaxial stress;
$\boldsymbol{\sigma}$	=	stress tensor;
$\boldsymbol{\sigma}^{ep}$	=	elasto-plastic stress tensor;
σ_{ij}	=	stress tensor components;
$\boldsymbol{\sigma}^{tr}$	=	trial stress tensor;
$\boldsymbol{\sigma}_i^{tr}$	=	principal component of the trial stress tensor;
τ_μ	=	retardation time of the μ-th Kelvin unit;
ν	=	Poisson's coefficient;
ω	=	scalar damage variable with stiffness recovery;
ω^*	=	total scalar damage variable;
ω_c	=	scalar damage variable in compression;
$\omega_{c,max}$	=	maximum value of damage in compression;
ω_t	=	scalar damage variable in tension;
$\omega_{t,max}$	=	maximum value of damage in tension;
(ξ, ρ, θ)	=	Haigh-Westergaard coordinates;

List of Figures

List of Tables

Contents

Chapter 1

Introduction

1.1 Motivation and background

Concrete structures such as bridges, highway pavements, or machine foundations, which are subjected to cyclic loads, can fail at stress levels far below the ones observed during monotonic loads. Therefore, understanding the mechanisms behind the fatigue failure of concrete structures is relevant for a better prediction of the fatigue life of such structures. The study of the fatigue behaviour of concrete has received increased attention during the last century [1]. However, there is still no comprehensive model that could explain and predict the fatigue behaviour of concrete. This could be ascribed to two main factors. The first factor is the complex heterogeneous structure of concrete materials. In fact, the complex interaction between the different phases that compound concrete materials lead to a remarkably non-linear behaviour under mechanical loading, such as mechanical degradation, permanent deformations, creep, etc. The second factor regards the multiple parameters that influence the fatigue behaviour of concrete such as stress levels, loading rate and waveform, moisture, and temperature, just to mention a few. This enhances the high variability of fatigue test results.

From experimental studies [2–7], concrete fatigue failure is related to the gradual and permanent structural changes that occur inside the complex heterogeneous material. It may result in the

nucleation and coalescence of micro-cracks, until meso- or even macro-cracks are formed. Depending on the scale of the defects, one can distinguish between two main types of fatigue regime: Low-Cycle Fatigue (LCF), and High-Cycle Fatigue (HCF). According to Lemaitre et al. [8], LCF occurs under repeated high level cyclic loads, with a stable growth of meso-scale to macro-scale cracks until failure. On the other side, HCF occurs under a large number of repeated cycles with stress levels much lower than the LCF. HCF damage is driven by a progressive accumulation of defects that initiate at a micro- or nano-scale, making such a fatigue failure difficult to study [8, 9]. The transition number of cycle to failure between LCF and HCF is usually considered as 10^3 to 10^4, especially for high strength concrete [1, 9, 10].

For many years, fatigue life of concrete has been modelled using lifetime-based approaches. They are phenomenological approaches in which mechanical quantities such as the residual strength, the maximum strain, or the modulus of deformation are expressed as a function of the number of cycles performed [1, 11–17]. In this kind of approach, fatigue damage approximation is commonly based on a linear accumulation of damage with the number of cycles, such as the Palmgren-Miner rule, where the total damage is estimated as the sum of the ratio of the number of cycles to the estimated fatigue life, for each stress level. Despite the simplicity of the linear damage accumulation rule, experimental tests on concrete reported in the literature have shown that the fatigue damage of concrete is actually non-linear. In particular, by evaluating the effect of loading sequence on fatigue damage accumulation, Lei et al. [18] have shown that the concrete cumulative damage factor obtained using the Palmgren-Miner rule can be lower than unity in high-to-low loading sequence and greater than unity in low-to-high loading sequence. Hence, overly-conservative or non-conservative predictions can be obtained using the Palmgren- Miner rule. Moreover, the experimental nature of lifetime-based approaches makes it impossible to understand the complex mechanisms of fatigue damage, and additional effects such as permanent deformations, thermal loads, aging, creep and shrinkage cannot be coupled with such models in a unified formulation.

The development of the continuum damage mechanics (CDM) has proven to be a powerful tool to study the damage of concrete materials. It postulates the material homogeneity over a suitable representative volume element of concrete, which size is relevant compared to the micro-cracks size.

Coupling between the classical plasticity theory and continuum damage mechanics can provide a strong framework to simulate the non-linear behaviour of concrete under cyclic loads [19]. A suitable yield condition, a flow rule, and a hardening/softening rule, are amongst the necessary components required to build a plasticity model. For concrete-like materials, plasticity models are based on pressure-sensitive yield surface and non-associated flow rule. The damage part is usually formulated in the framework of isotropic scalar damage, and required the definition of a damage loading function with the corresponding equivalent strain and its evolution law. Lee et al. [20] have proposed a plastic-damage model in which the elasto-plastic response and the degradation damage response are decoupled. The plastic formulation of the model uses a modified version of the Lubliner's yield function [21], and the damage formulation is based on the fracture energy. The Lee and Fenves model has been extensively used in the literature to simulate tensile and compressive cyclic loadings [22–24]. Grassl et al. [25] have proposed a coupled plasticity-damage model of concrete suitable for predicting the mechanical behaviour in axial, bi-axial, tri-axial cyclic compressions, and in uniaxial cyclic tension. The model uses an adapted version of the modified Leon model [26] formulated in the Haigh-Westergaard effective stress space. The damage evolution is controlled by the plastic strain and the evolution law for the scalar damage variable is assumed to have an exponential form. In order to account for crack opening/closure effect during cyclic loading, the previous model has been improved [27], by considering a decomposition of the total damage variable into a compression and tension part.

Many other researchers have coupled plasticity and continuum damage mechanics in order to model the cyclic behaviour of concrete [19, 28–33]. However, these models present some limitations for the fatigue modeling of concrete, especially when the comparison is made between HCF and LCF. In fact, the stress level to reach failure in HCF are much lower than the one in LCF, as the fatigue behaviour is driven by a progressive accumulation of microscopic defects. The fatigue failure in HCF can occur for stress levels below the yield surface. As a consequence, constitutive models for HCF must allow for plastic flow or damage accumulation, for stress states inside the yield surface. The previous coupled plastic-damage models could be suitable for capturing the fatigue failure of concrete in the LCF, where the stress levels during cyclic loading lie outside of the elastic domain,

but they need to be extended for a proper modelling of HCF [9, 34].

In order to reproduce the mechanical behaviour that brittle materials exhibit during HCF, Lemaitre et al. [8] have proposed a two-scale model. The model is grounded on the physical observation that, even though the stress at the level of the representative volume element (meso-scale) is inside the elastic domain during HCF, the local stress (micro-scale) can lie outside the elastic domain, due to local heterogeneities. In order to catch this scale effect, the two-scale model considers a "weak" inclusion that represents the micro-defect inside the representative volume element at the meso-scale. The overall elasto-plastic behaviour is the same at both scales, but only the weak inclusion is allowed to damage, while the matrix surrounding it can remain elastic. The coupling between the two scales is done by relating the plastic strains at the micro-scale to the strains at the meso-scale level through an appropriate localisation law. Although this model can predict fatigue failure, its extension to the micro-scale requires to determine additional material parameters, and to solve further equations.

Marigo [35] has proposed a fatigue damage model that can describe realistically LCF and HCF failures. In this formulation, the yield concept is replaced by an irreversible loading-unloading condition, and the model allows for damage growth for stress states below the damage surface. The damage equivalent strain is usually defined so that damage increases during the loading phases and no further damage occurs during the unloading phases of the cyclic load. The model usually required the definition of a gauge function taking values between 0 and 1, that is an alternative to the yield function, and of a continuous and increasing function evaluated at the gauge function, that allows for damage below the damage surface. Recently, many scholars have used the Marigo's formulation to simulate the fatigue behaviour of brittle materials [31, 34, 36, 37]. Although these models can fairly well simulate the HCF behaviour of concrete, none of them take into account the creep behaviour of concrete. In fact, Experimental results [38–40] corroborate the idea that it exists an evident correlation between creep and damage of concrete, especially with regards to concrete structures subjected to long-term loads. Physically, the strain mismatch between the creeping cement matrix and the stiffer aggregates can generate local stresses in the matrix higher than the macro-scale stresses, leading to damage [41]. This aspect is relevant for HCF, in which fatigue failure

can occurs after several cycles. In the literature, some researchers have used phenomenological creep models combined with damage to simulate the behaviour of concrete materials [41–45]. However, none of these models is able to simulate the plastic, creep and damage behaviour of concrete, including multi-axial stress states and local confinement effect in a comprehensive manner.

More recently, Oneschkow et al. [6] have proposed a finite element approach with a gradient-enhanced equivalent strain-based damage model combined with a fatigue model in order to simulate the fatigue behaviour of concrete. The model uses a gradient-enhanced equivalent strain measure in order to overcome mesh-dependency issues. The fatigue model is obtained, extending the classical damage criterion by including a strength reduction function that is suitable to describe the initial damage processes, but also the stable damage-growth phase of fatigue. As the number of cycles increases, the threshold for which static damage occurs gradually decreases, and damage can occur even for stress levels below the damage surface.

Another challenging aspect that characterizes concrete modeling is related to the material heterogeneity, and the interaction between its different phases. In fact, a homogeneous or macro-scale modeling of concrete is rather a coarse representation of its structural geometry, and it does not allow to distinguish the different behaviours of the internal constituents, nor to bring light to the complex interaction between them, such as local confinement effects due to compressive loads [46]. On the other hand, a micro-scale modeling of the heterogeneous internal constituents of concrete leads to very complex constitutive models, with numerous material parameters, often without a physical meaning [47]. A good compromise between the two above-mentioned modelling scale is the meso-scale modelling, in which concrete is modeled as a three-phase material, made of aggregates, the cement matrix and the Interfacial Transition Zone (ITZ) in between. Simpler meso-scale models consider only two phases, made of coarse aggregates and the cement matrix. This meso-scale modeling, especially for a 3D geometry, allows for a more comprehensive simulation of concrete behaviour, with moderate computational costs. Furthermore, the meso-scale modeling can be useful to describe some macro-scopic behaviour of concrete, by having a deeper insight at the local material deterioration that occurs at the interface between the aggregates and the cement matrix[48–50].

Despite the ongoing research on the development of constitutive models in order to reproduce

the mechanical behaviour of concrete under fatigue and cyclic loading, there is still the need of a comprehensive model grounded on a physical basis, and able to capture the main non-linear characteristics that concrete materials exhibit during complex fatigue loads. In this work, a robust 3D visco-elasto-plastic damage model is presented, in order to reproduce the non-linear mechanical behaviour of concrete subjected to creep and fatigue loads in multi-axial stress states. The visco-plastic formulation of the model considers the pressure-dependent Ménétrey-Willam yield function [51], extended to include strength degradation due to static damage. The stiffness degradation and crack-closure effects are accounted for, by a differentiation between tensile and compressive damage with the scalar and isotropic Mazars damage model [52]. The creep formulation considers the B3 model of Bažant and Baweja [53] and a strain additivity hypothesis serves as the foundation for the coupled model. In the proposed fatigue model, the physical micro-structural degradation due to fatigue is interpreted as a gradual reduction of size of the elastic domain as the number of cycles increases. This is achieved by considering an extension of the modified Ménétrey- Willam yield function to include a fatigue softening function that represents the effects of the cumulative and irreversible micro-structural degradation as the number of cycles increases. The fatigue behaviour is driven by an internal variable based on the amount of extension experienced by the material. Numerical tests are performed at the macro- and meso-scales to evaluate the capabilities of the proposed model. Interestingly, the performance of the coupled model is more relevant at the meso-scale, in which local effects can be observed. The study of the bi-phase mesoscale model suggests that, the non-linear creep behaviour of concrete can be attributed to the growth and coalescence of plastic regions that develop at the interface between the stiffer aggregates and the creeping mortar. This non-linear behaviour is not included in the B3 model of Bažant and Baweja. The fatigue tests performed at the meso-scale of the coupled model show premises of the capabilities of the proposed model to reproduce the non-linear mechanical behaviour of concrete subjected to generic 3D stress states under cyclic loadings.

A preliminary step to the development of such a model is the understanding of the micro-mechanical damage processes related to fatigue, that occur inside the complex heterogeneous material structure. Then. a review on the relevant aspects that can affect the fatigue performance of

concrete materials will be performed.

1.2 Fatigue damage processes in the concrete micro-structure

Despite the extensive and ongoing research on the fatigue damage of concrete, the mechanisms behind the fatigue failure and the exact point at which it occurs are still subject of discussion. This could be explained by the complexity of the material structure [10] and the many factors that can influence the fatigue behaviour such as the amplitude, rate and frequency of loading, the minimum and maximum stress levels, the waveform, the moisture and temperature, material strength, just to mention a few [1, 15, 54–57]. However, some fatigue properties of concrete are still widely acknowledged by researchers. Fatigue damage of concrete materials can be described as the gradual and irreversible degradation which occurs due to the nucleation of cracks at the microscopic scale at the cement matrix/aggregates interface, and inside the matrix itself [58–60]. These cracks can grow and coalesce inside the complex heterogeneous structure of concrete, until failure. Experimental evidences with the aid of high resolution techniques [61, 62] have shown that the distribution of cracking that occurs in concrete-like materials subjected to cyclic loading is more complex and extensive with respect to monotonic loading, as shown in Fig. 1.1.

Yang et al. [62] have obtained similar crack distribution by using Micro X-ray Computed Tomography (CT) to rock specimens subjected to monotonic and tri-axial cyclic loadings at failure, as shown in Fig. 1.2. This difference between the monotonic and cyclic crack patterns indicates that, the crack distribution is more diffuse at the macro-scale level in the case of cyclic loads. This micro-cracks can then grow and coalesce, until meso- or even macro-cracks are formed.

Although concrete does not exhibit a fracture pattern with distinguishable properties, Otto er al. [63] have found using a microscope, that the fracture surface of fatigue is remarkably smoother than monotonic loading, and some abrasion can be observed, as shown in Fig. 1.3. However, the extremely small scale at which the physical mechanisms related to fatigue damage occur makes it difficult to investigate the damage process correctly. The resolutions of commercially available instruments are often not sufficient and require the use of specimens of limited size, allowing only

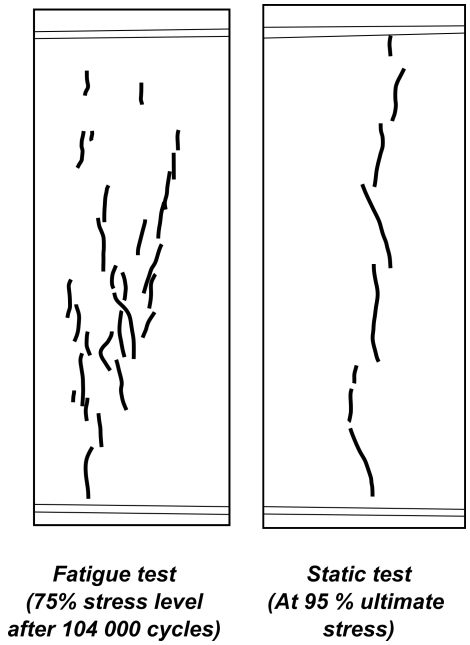

Figure 1.1: Comparison of crack distribution for cyclic (left) and monotonic (right) loadings [61].

for detection of relatively large cracks [59].

Macroscopic damage indicators that can be measured experimentally such as strain, remnant strength or stiffness, can be investigated to understand the micro-mechanical fatigue damage processes. With reference to strain, the total strain can be subdivided into an elastic part and a plastic part. The elastic part can be recovered during the unloading phase. However, the plastic part is irreversible and consequently, will accumulate as the number of cycles of loading increases. Therefore, the accumulated plastic strain can be interpreted as a macroscopic damage indicator intrinsically linked to the permanent micro-structural changes that occur in the material structure [1, 7, 57, 59, 64]. From experimental evidences, the plot of the total accumulated strain with the number of cycles has a typical inverted S-shape that can be subdivided into three stages as shown in Fig. 1.4 [7, 31, 59, 65].

The first stage, also called decay stage, is characterized by a rapid increase of the cumulative inelastic strain with decreasing rate, and last about 10 to 20% of the fatigue life. The second stage, also called steady stage, is characterized by a constant rate of cumulative strain, and corresponds

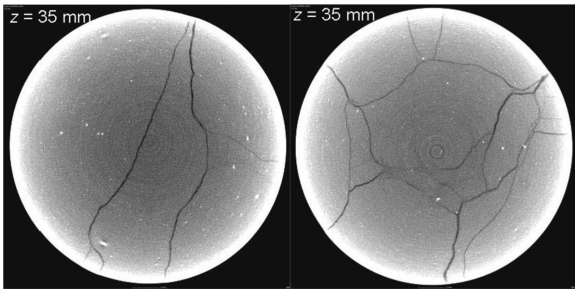

(a) Crack distribution for monotonic loading (left) and tri-axial cyclic loading (right);

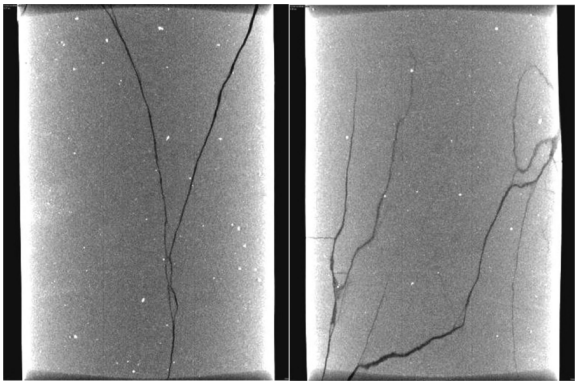

(b) Crack distribution for monotonic loading (left) and tri-axial cyclic loading (right);

Figure 1.2: Micro X-ray CT of horizontal (a), and vertical (b) cross-sections of rock specimens at failure subjected to monotonic and tri-axial cyclic loading [62].

to a steady damage growth. It can last about 60 to 80 % of the fatigue life. Finally, the last stage, also called accelerated stage, is described by an accelerated increasing rate of strain accumulation, corresponding to an abrupt increase of damage, leading to failure. It can last about 10 to 20% of the fatigue life. The transition phases between the different stages is dependent on the maximum stress level and the concrete strength. If the stress level is very high, the second stage could become very short, or even disappear, and we observe the failure of material after a few number cycles due to the rapid and excessive accumulation of inelastic strains [7]. This kind of failure usually corresponds to LCF. On the contrary, whenever the maximum stress level is relatively small, the third stage could not be observed, even after a high number of cycles. This corresponds to HCF, during which the inelastic strains accumulate very slowly [7].

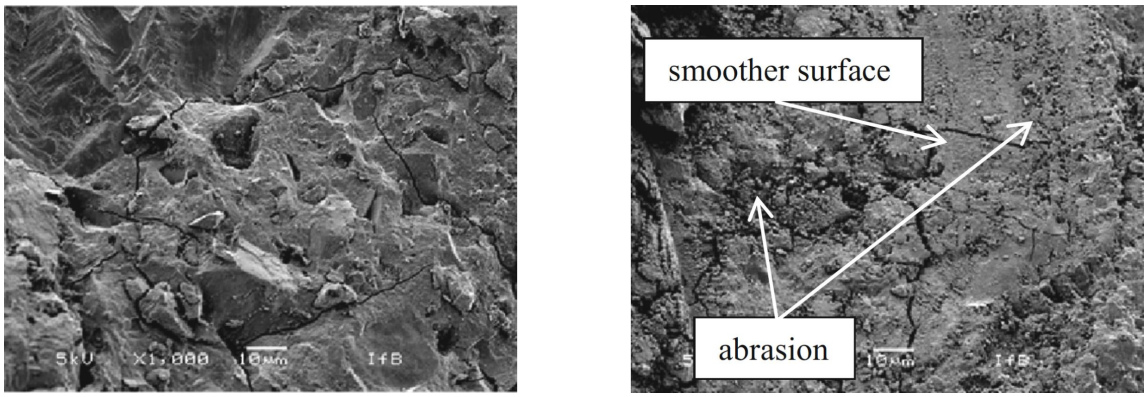

Figure 1.3: Fracture topography for monotonic (left) and cyclic (right) loading [63].

The fatigue failure regime according to the number of cycles to failure is reported in Fig. 1.5, where a super-high-cycle fatigue is shown, although it is considered by many scholars as a special case of HCF [1, 14]. High strength concrete which has a more brittle behaviour with respect to normal strength concrete, exhibits shorter duration for stages 1 and 3, of about 5% [56].

Strain-independent information about the damage mechanisms of concrete subjected to fatigue loading can be obtained using non-destructive techniques such as acoustic emission hits and ultrasonic pulse velocity technique. The first technique is based on the use of acoustic methods to record the vibrations due to the energy release as a consequence of crack formation. The quantitative distribution of the relevant parameters such as the amplitude or the frequency of the acoustic emission hits are used to provide qualitative information on damage propagation [59, 66–68]. The ultrasonic pulse velocity method measures the transit time of ultrasonic pulses through the specimen, which depends on the density and the elastic properties of the material tested. This transit time is affected by the crack opening [69]. Both methods exhibit the same qualitative behaviour as the strain development, that is, the three stages of crack development can be observed, as shown in Fig. 1.6.

By means of fluorescence microscopy with polished sections, and scanning electron microscopy, Thiele et al. [71] have studied the crack development during the three stages of the strain curve. He found that, while the mean crack widths can increase slightly during the transition from the decay

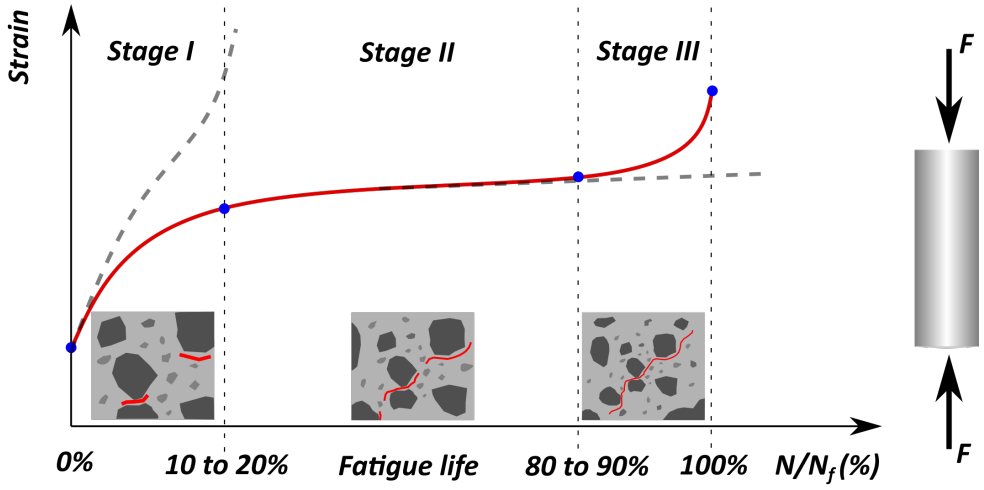

Figure 1.4: Typical three-stage strain accumulation curve for concrete subjected to cyclic loading.

stage to the steady stage, the crack length might decrease during the decay stage, and remain unchanged or increase slowly during the steady phase. However, almost no variation in crack pattern could be detected during the decay and the steady stages, probably due to the extremely small scale on which structural changes occur during these stages. The cracks were oriented in the loading direction during the acceleration stage, with mean values of width in the range of 5.0 µm to 12.5 µm.

The crack growth in concrete due to fatigue is strongly influenced by the interaction between the coarse aggregates and the cement paste. By studying the stress distribution in the concrete micro-structure subjected to monotonically increasing and cyclic compressive loads, Mehmel et al. [72] have shown that the large difference in stiffness between the aggregates and the cement matrix leads to a non homogeneous stress distribution with areas of peak stresses in the cement matrix. The local peak stresses can be much higher that the external stresses imposed and depend on the size and the amount of aggregates, or the ratio of the stiffness of the aggregates and cement matrix. According to [72], the areas of internal peak stresses, located at the interface between the aggregates and the cement matrix, lead to further damage within the cement matrix. This result was confirmed by Oneschkow [6], who has shown experimentally that the coarse aggregates have a detrimental effect on the concrete fatigue behaviour with a higher stiffness degradation,

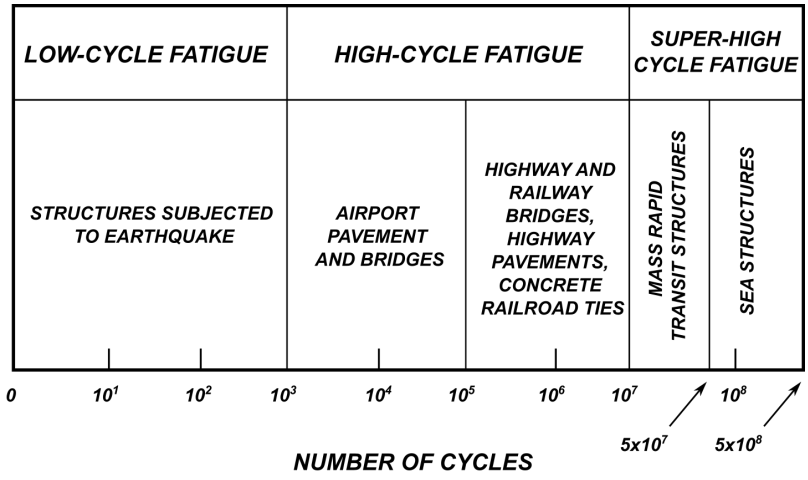

Figure 1.5: Fatigue regime thresholds and corresponding loads/structures [14].

compared to that of the mortar. Despite that, the number of cycles to failure at high level stress between the concrete and mortar specimens where similar. However, he also observed that, for low stress levels, stress redistribution can occur between the stiffer aggregates and the cement matrix, relieving significantly the fatigue sensitive cement matrix. As consequence, concrete specimens have exhibited higher fatigue life than mortar specimens.

1.3 Loading parameters affecting the fatigue behaviour of concrete

Several parameters can influence the fatigue life and behaviour of concrete. Amongst them, are the maximum stress level, the loading amplitude and frequency, the multi-axial stress state, the moisture, and the temperature, just to name a few. In the literature, some authors have studied the effects of these parameters on the fatigue response of concrete, mainly via experimental tests. However, due to the fact that these parameters can interact together, the results are sometimes contradictory, or difficult to interpret [1]. As loading is one of the main factors related to fatigue, this section gives a brief review of the effects of parameters associated to loading, that can influence the fatigue performance of concrete.

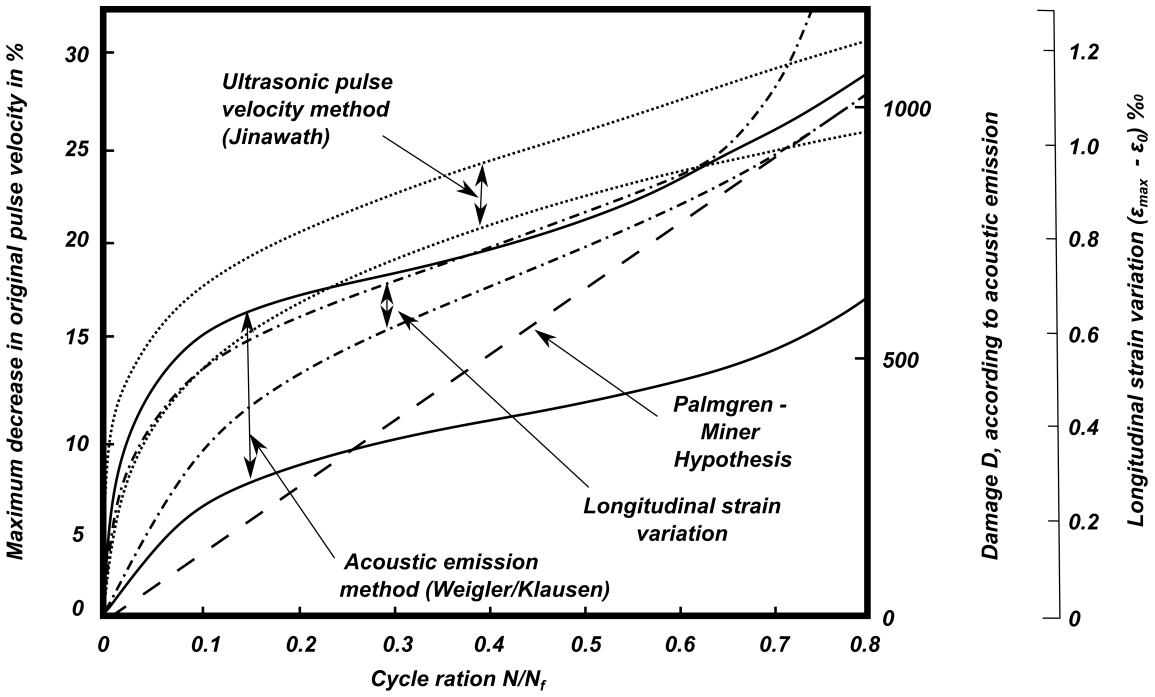

Figure 1.6: Comparison of the fatigue degradation obtained using longitudinal strain measurement, acoustic emission method, and ultrasonic pulse velocity method [70].

1.3.1 Maximum stress level

With regards to the effect of the maximum stress level, several empirical formulae have been developed between the maximum stress level and the logarithmic number of cycles. Most are approximated by a linear relationship, with various levels of accuracy [2–4, 73], and are often used in design codes [74, 75]. Holmen et al. [70] have proposed a non-linear relationship between the stress level and the logarithmic number of cycles, in order to account for the increased standard deviation of regression formulae at low stress levels. In order to account for the different fatigue behaviour in Low-Cycle and High-Cycle regimes, Hsu et al. [76] have proposed different linear approximation formulae for each regime. More recently, Zhang et al. [77] have investigated the effect of the stress level on the fatigue performance of plain concrete based on the energy dissipation method. He found that, the development of strain, stiffness degradation, and fatigue damage, exhibit a three-stage pattern, similar to the one described in Section 1.2. Furthermore, in the secondary stage, the value

of strain rate remains approximately constant, independently of the stress level.

1.3.2 Loading frequency

With regards to the loading frequency there is still no consensus on its influence on the fatigue performance of concrete [1]. This could be ascribed to the combined effects with temperature and stress range [1]. In the past, some experimental investigations have shown little to no effect on the fatigue response, according to the maximum stress level. Works by Mehmel et al. [78], who has considered fatigue tests with frequency range of 0.5 to 1 Hz, and Graf et al. [79], who has considered frequency range of 4.55 to 7 Hz, have shown no effect of loading frequency on fatigue performance, provided that the ratio between the maximum stress level and the static strength was less than 75 %. This observation is supported by the work of Raithby et al. [54], who has found no frequency effect on fully saturated beams, when considering two different sinusoidal load frequencies of 4 and 20 Hz. However, for higher stress levels (from 80 to 95 % of the static strength), Awad et al. [80] have found a reduction of fatigue performance with decreasing rate of loading. In particular, by plotting the rate of loading versus the logarithmic number of cycles, it was found that a reduction of the rate of loading by one order of magnitude can lead to a reduction of the fatigue life by almost one order of magnitude. These observations are consistent with more recent research[15, 56]. Despite the lack of consensus about the effect of frequency on fatigue life of concrete, efforts have been made to develop correlation between the stress level and the number of cycle to failure, including a loading frequency parameter [73, 81].

1.3.3 Lateral confinement

Multi-axial stress states can have a significant effect on the response of concrete materials subjected to repeated loadings. From experimental evidences, it comes out that a confining stress has a beneficial effect on the fatigue performance, especially under compressive cyclic loads [82–85]. Similarly to the monotonic case, Buyukozturk et al. [84] have shown that the failure strains under cyclic loading increase with the confinement level. Taliercio et al. [86] have performed experimental tests on rectangular specimens, considering cyclic confinement pressure in opposition or in phase

with the axial stress. It was found that, specimens in which the axial stress vary in phase with the confining pressure exhibit higher fatigue life, than specimens in which they vary in opposition of phase. Hooi et al. [85], have extended the fatigue life formulation of Aas et al. [2] to include a parameter accounting for the confinement effects. They have shown that the confinement parameter has a similar trend, for monotonic and fatigue tests. This is consistent with the observations from literature [82, 83], that confinement has similar effects on monotonic and cyclic strengths. However, other studies has demonstrated that, when the specimen is subjected to cyclic tensile loads or alternated tensile-compressive loads, the lateral confinement can have detrimental effects on the fatigue strength. By studying tri-axial compression-tension cyclic loadings on tapered prismatic concrete specimens, Song et al. [87] have found out that, the fatigue life and strength under tri-axial loads are both lower that the ones in uni-axial load. In addition, their values decrease, with increasing lateral confinement pressure. Similar observations were made by Wang et al. [88] in the case of pure tension. Overall, the effects of the lateral confinement pressure depend on the nature (compression or tension) of the applied load.

1.3.4 Other parameters associated with loading

Factors related to loading such as loading waveform, rest periods, and multiple stage loading can affect the fatigue response of concrete materials. Tepfers et al. [89] have investigated the response of prismatic specimens of concrete to cyclic compression, considering three different types of waveform: rectangular, triangular, and sinusoidal. As expected, they observed that the fatigue damage occurs faster in the case of rectangular waveform, due to the fact that, the specimen sustains the peak load for a longer period. In addition, the final strain and the number of cycles to failure were higher for the triangular waveform. Similar results were found by a more recent research from Oneschkow et al. [57]. By comparing sinusoidal to triangular loads, they concluded that the waveform can affect both the fatigue life and strain at failure. With regards to rest periods, early investigations [90] have shown that rest periods have beneficial effects on the fatigue performance of concrete materials. Hilsdorf et al. [12] have studied the effect of rest periods on fatigue flexural tests. It came out that, rest periods up to 5 minutes resulted in an increase of fatigue strength, compared

to continuous loading. However, it was observed that, rest periods bigger than 5 minutes have no effects on the fatigue performance, and that the frequency of the rest periods have more effects on the fatigue performance than their duration. The effects of the loading sequence have been studied via fatigue tests with multiple stage loading by Hilsdorf et al. [12], and more recently by Baktheer et al. [91]. They agree that, the sequence of loading affects the fatigue response, and that the linear accumulation of damage of Palmgren-Miner does not fit with experimental results. In order to tackle this issue, Lei et al. [18] have proposed a non-linear rule for damage accumulation during cyclic tests, considering multi-stage loading. A better fitting was found between experimental results and numerical results from the non-linear rule for damage accumulation, with respect to the Miner's rule.

1.4 Research scope and objectives

The present work aims to develop a robust constitutive model for concrete, able to reproduce its mechanical behaviour under long-term and fatigue loads. The proposed model is motivated by the analysis of physical mechanisms underlying the fatigue failure of concrete materials. In particular, the physical micro-structural degradation due to fatigue is interpreted at the progressive accumulation of the irreversible plastic strains observed at the macro-scale. Furthermore, the creep failure is accounted for, by an excessive acculation of plastic strains.

The constitutive model presented herein, combines the plasticity theory, with the continuum damage mechanics, in order to describe the plastic strain evolution inside the material. The plastic formulation of the model considers the pressure-dependent Ménétrey-Willam yield function [46, 51, 92], extended to include strength degradation effect due to static damage. The stiffness degradation is accounted for, by a differentiation between tensile and compressive damages, with the scalar and isotropic damage model of Mazars [52, 93]. In order to catch the increase of stiffness due to the closure of cracks as the mechanical load changes from tension to compression, a stiffness recovery function is included in the formulation of the scalar damage variable. The creep formulation considers the B3 model of Bažant and Baweja [53] and a strain additivity hypothesis serves as the

foundation for the combined model. The fatigue damage is considered by an extension of the modified Ménétrey- Willam yield function to include a fatigue softening function that represents the effects of the cumulative and irreversible micro-structural degradation as the number of cycles increases. The model is able to simulate LCF and HCF, allowing for plastic flow and damage accumulation for maximum stress levels below the initial yielding point. In addition, it is able to account for fatigue relevant parameters, such as loading amplitude, maximum stress levels, and simultaneously takes into account permanent and creep deformations, pressure-dependent effects under multi-axial stress states in a unified manner.

Moreover, the model aims at studying the physical interaction between the different phases that constitute concrete materials, namely, the aggregates and the cement mortar. This is achieved by a meso-scale modelling, in which only coarse aggregates (with nominal size bigger than 5 mm) are considered, for computational cost issues.

1.5 Outline of the dissertation

The remaining part present work is organised as follows.

In Chapter 2, a literature review on constitutive models for concrete, that combine plasticity theories with damage mechanics is provided. A particular attention is made with regards to models capable of simulating cyclic loads. Then a comprehensive review on the constitutive models that incorporate a fatigue damage behaviour is included.

In Chapter 3, the different components of the combined model are described, and the mathematical formulations are provided.

The numerical implementation of each component of the constitutive model is described in Chapter 4, and some relevant aspects regarding the numerical implementation are discussed.

Finally, the numerical results are presented and their juxtaposition with experimental results are discussed in Chapter 5. The extension of the simulation at the meso-scale is considered, for a better insight on the physical interaction between the aggregates and the cement matrix, that constitute the material.

Chapter 2

Literature review

2.1 Motivation and background

For many years, the fatigue behaviour of concrete has been modelled using lifetime-based approaches [1]. They are based on Wöhler curves or S-N curves which are semi-logarithmic curves depicting the life time of the concrete structure expressed in terms of number of cycle of loads prior to failure, as a function of the stress amplitude. These curves were first developed by Wöhler between 1852 and 1870, during the assessment of the fatigue behaviour of railroad steel structures [94, 95]. The early models for concrete where developed by Knut Aas-Jacobsen in 1970 [2] and later improved by Tepfers [73] to account for the influence of the mean stress. He proposed the following expression:

$$S_{\max} = \frac{\sigma_{\max}}{f_c} = 1 - \frac{1}{C_c}(1 - R)\log N \tag{2.1}$$

where

$S_{\max} = \frac{\sigma_{\max}}{f_c}$ is the ratio of the maximum concrete stress to the concrete strength;

$R = \frac{\sigma_{\min}}{\sigma_{\max}}$ is the ration between the minimum and maximum concrete stresses, and N is the number of load cycles.

$C_c = 14,6$ is the value of $\log N$ when $R = S_{\max} = 0$.

Damage approximation in lifetime-based models are commonly based on a linear accumulation of damage with the number of cycles, such as the Palmgren-Miner rule [96, 97]. It states that the energy dissipation of each fatigue cycle is the same under the same stress level, and that fatigue damage is independent of the loading sequence. The total damage is estimated as the sum of the ratio of the number of cycles to the estimated fatigue life, for each stress level. Therefore, the failure criterion is specified as

$$\sum_{i=1}^{k} \frac{n_i}{N_i} = 1, \tag{2.2}$$

where n_i is the number of cycles for the $i-th$ stress level, N_i represents the number of cycles to failure for the $i-th$ stress level, and k is the total number of stress levels. Many researchers have used the linear damage accumulation theory to describe the fatigue of concrete [98, 99].

Despite the simplicity of linear damage accumulation rule, experimental tests on concrete reported in the literature have shown that the fatigue damage of concrete is actually non-linear. In particular, by evaluating the effect of the loading sequence on the fatigue damage accumulation, Lei et al. [18] have shown that the concrete cumulative damage factor obtained using the Palmgren-Miner rule can be lower than unity in high-to-low loading sequence and greater than unity in low-to-high loading sequence. Hence, overly-conservative or non-conservative predictions can be obtained using the Palmgren- Miner rule [18, 86, 100, 101]. Although non-linear damage theories have been developed to tackle the issues of linear damage accumulation [102–107], their experimental nature makes it impossible to understand the complex mechanisms happening under the hood as concrete damages due to fatigue. Furthermore, additional effects such as permanent deformations, thermal loads, aging, creep and shrinkage can not be coupled with such models in a unified formulation. Therefore, there is the need of more sophisticated models, accounting for the above-mentioned effects.

In the following sections, a literature review on plastic damage models accounting for cyclic loadings is presented, with a focus on isotropic damage models, which is the damage formulation adopted in this work. Usually, these models cannot reproduce the behaviour of concrete under cyclic loads of constant amplitude, or under repeated loads in the HCF regime. Next, a comprehensive

review of fatigue models of concrete, accounting for the above-mentioned effect is presented.

2.2 Plasticity models coupled with Continuum Damage Mechanics for cyclic loads

The development of the Continuum Damage Mechanics (CDM) has proven to be a powerful tool to study the damage of concrete materials. It postulates the material homogeneity over a suitable representative volume element of concrete, which size is relevant compared to the micro-cracks size. In the classical approach of CDM, an internal variable is used as a progressive measure of damage. A damage loading surface is defined, and damage starts as soon as the stress state lies on the damage/yield surface. The macroscopic effects of the nucleation and propagation of micro-cracks are the softening of the material which can be modelled by classical plasticity [51, 108–112], and the alteration of the elastic modulus of the material, which can be modeled using the effective stress concept in the CDM [113–116]. Therefore, coupling the plasticity theory and continuum damage mechanics provides a strong framework to simulate the cyclic and non-linear behaviour of concrete [19]. In the literature, many scholars have studied the cyclic behaviour of concrete by means of the CDM. Attempts have been made to couple damage mechanics with other theories of concrete such as plasticity and creep, in order to reproduce holistically the main non-linear features of concrete under mechanical loads. The proposed constitutive models mainly differ by the nature of the damage driving variable and its evolution law, and the shape of the damage/plasticity surface. A well known plastic-damage model of concrete which has been used to simulate the cyclic behaviour of concrete is the one proposed by Lee et al. [20], that has been widely used by researchers [19, 24, 117]. This model combines the classical plasticity theory and isotropic damage theory of Kachanov in a consistent thermodynamical formulation. The attractiveness of the Lee and Fenves model relies on the decoupling between the elasto-plastic response and the degradation damage response, which provides more stability for its numerical implementation [19]. The plastic formulation of the model is based on the yield function proposed by Lubliner et al. [21], modified by Lee and Fenves to account for different strength evolution during cyclic loading under tension and compression. This

is achieved by defining two cohesion variables, a tensile one and a compressive one, as shown in Eq. 2.3

$$F(\bar{\sigma}, \boldsymbol{\kappa}) = \frac{1}{1-\alpha}\left[\alpha \bar{I}_1 + \sqrt{3.\bar{J}_2} + \beta(\boldsymbol{\kappa})\left\langle \hat{\bar{\sigma}}_{\max}\right\rangle\right] - c_c(\boldsymbol{\kappa}), \tag{2.3}$$

where

$$\beta(\boldsymbol{\kappa}) = \frac{c_{\mathrm{c}}\left(\kappa_{\mathrm{c}}\right)}{c_{\mathrm{t}}\left(\kappa_{\mathrm{t}}\right)}(1-\alpha) - (1+\alpha). \tag{2.4}$$

In Eq. 2.3, c_c and c_t are the tension and compression cohesions respectively; α is a dimensionless constants; $\bar{I}_1$ is the first invariant of the effective or undamaged stress tensor; $\bar{J}_2$ is the second invariant of the effective deviatoric stress tensor and $\hat{\bar{\sigma}}_{\max}$ is the largest effective principal stress. $\boldsymbol{\kappa} = (\kappa_c, \kappa_t)$ is the internal variable vector representing the damage states, as described further on. A linear Drucker-Parager type function has been used as the plastic potential function, and a non-associative rule has been used to describe the plastic strain evolution. For the damage formulation of the model,a fracture-energy-based scalar damage variable has been used. In order to account for the different damage behaviours in tension and compression, two damage driving variables, κ_c and κ_t are defined for compression and tension damages respectively. Their evolution law is given as

$$\dot{\boldsymbol{\kappa}}_{\aleph} = \frac{1}{g_{\aleph}} f_{\aleph}\left(\kappa_{\aleph}\right)\dot{\varepsilon}^{\mathrm{p}}, \tag{2.5}$$

where

$$g_{\aleph} = \int_0^{\infty} \sigma_{\aleph} \mathrm{d}\varepsilon^{\mathrm{p}} \tag{2.6}$$

represents the specific fracture energy, defined as the ratio between the fracture energy and the characteristic length; $\aleph \in \{t, c\}$ is a state variable representing the uniaxial tensile and compressive states; $f_{\aleph}$ represents the effective stress response in the uniaxial case. Two damage variables, one in tension $\omega_{\mathrm{t}} = \omega_{\mathrm{t}}\left(\kappa_{\mathrm{t}}\right)$ and one in compression $\omega_{\mathrm{c}} = \omega_{\mathrm{c}}\left(\kappa_{\mathrm{c}}\right)$, have been defined as increasing functions of the corresponding internal driving variables in tension and compression respectively [20]. They can take values between zero and unity. A total scalar damage variable have been defined to account for both tensile and compressive damages

$$\omega = 1 - (1 - \omega_{\mathrm{c}}(\kappa_{\mathrm{c}}))(1 - \omega_{\mathrm{t}}(\kappa_{\mathrm{t}})). \tag{2.7}$$

An important feature that concrete materials under cyclic loads exhibit, especially when it ranges from tension to compression, is the degraded stiffness recovery effect [118]. In fact, when the mechanical load changes from tension to compression, the cracks that were opened during the tensile phase, become closed during the compressive phase. This leads to smaller damaged area, and therefore and increase of stiffness of the material during the transition. In order to account for the crack opening/closure effect during cyclic loads, Lee and Fenves have modified the total damage variable in Eq. 2.7 using a parameter s which values range between zero and unity. The new expression of the total damage variable ω takes the form

$$\omega = 1 - (1 - \omega_{\mathrm{c}})(1 - s(\bar{\boldsymbol{\sigma}})\omega_{\mathrm{t}}), \tag{2.8}$$

where

$$s(\bar{\boldsymbol{\sigma}}) = s_0 + (1 - s_0)\, r(\hat{\bar{\boldsymbol{\sigma}}}) \tag{2.9}$$

is the stiffness recovery parameter; $0 \leq s_0 \leq 1$ is the minimum value of the stiffness recovery parameter; The function $r(\hat{\boldsymbol{\sigma}})$ is defined such that

$$r(\hat{\bar{\boldsymbol{\sigma}}}) = \left(\sum_{\mathrm{i}=1}^{3} \langle \hat{\bar{\sigma}}_{\mathrm{i}} \rangle\right) / \left(\sum_{\mathrm{i}=1}^{3} |\hat{\bar{\sigma}}_{\mathrm{i}}|\right), \tag{2.10}$$

where $\hat{\bar{\sigma}}_{\mathrm{i}}$ is the i-th eigenvalue of the effective stress tensor; $\langle x \rangle = (x + |x|)/2$ denotes the ramp function and $|x|$ is the absolute value of x.

The total stress has been defined using the effective stress concept, and taking into account permanent deformations obtained from the plastic model. Therefore the constitutive relationship has the following form, where the degradation damage and effective elasto-plastic stress responses can be factored

$$\boldsymbol{\sigma} = (1 - \omega_c(\boldsymbol{\kappa}))(1 - s\omega_t(\boldsymbol{\kappa}))\, \boldsymbol{D} : (\boldsymbol{\varepsilon} - \boldsymbol{\varepsilon}^p). \tag{2.11}$$

It is important to note that, in this model, the plasticity formulation is based on the effective or undamaged stress space, offering a greater stability to the numerical algorithm of the coupled plastic-damage model.

By comparing 2-D numerical simulation results with experimental results from [23] for uni-axial cyclic tensile loading and from [22] for uni-axial compressive loading, the Lee and Fenves damage model was able to catch fairly well the softening response of concrete and has shown a good control of dilatancy. Moreover, it was able to describe the stiffness degradation observed experimentally during the cyclic loading in compression and tension. However, the model is unable to catch the experimental closed loops that concrete exhibits when it is subjected to uni-axial cyclic compression or tension loads, during the unloading and the reloading phases. Another comparison between experimental results from cyclic tensile-compressive loading [118] and 2-D numerical numerical simulation results has shown that the model was able to catch with a good precision, the increase in stiffness as the mehanical loading changes from tension to compression.

Omidi et al. [19] have used the Lee and Fenves plastic-damage model to develop a 3-D algorithm for numerical simulations, instead of a 2-D one as in the original formulation of Lee and Fenves. A reformulation of the return-mapping process was necessary to overcome the issue of the singularity at the apex. Therefore, they have used the Drucker-Prager hyperbolic function instead of the linear one of the original model, for the treatment of the apex singularity. The proposed algorithm was able to reproduce well the post-peak behaviour of concrete under cyclic loads.

Another plastic-damage model for cyclic behaviour simulation was proposed by Grassl et al. [25]. As the Lee and Fenves model, the plastic part of the model is formulated in the effective stress space and not in the nominal or damaged stress space. With regards to this aspect, they have shown that for effective stress-based plasticity models, the combination of plasticity and damage does not result in further restriction on the model parameters, because the local uniqueness condition is always satisfied, provided that the softening modulus does not drop below a critical value. However, for nominal stress-based plasticity models, the plastic part must show strong hardening to be in agreement with the local uniqueness conditions. Therefore, they are inappropriate to model softening or low-confined compression of concrete. An adapted version of the modified Leon model

[26] formulated in the Haigh-Westergaard effective stress space has been used as the yield surface. A non associative flow rule with a quadratic form plastic potential has been used to describe the evolution of the plastic strains. The rate of the hardening variable, that controls the evolution of the yield surface is defined as the norm of the plastic strain rate, scaled by a hardening ductility measure. A scalar isotropic damage model is used, in which the damage loading function is given by

$$f_{\mathrm{d}}\left(\boldsymbol{\varepsilon}^{\mathrm{p}}, \kappa_{\mathrm{d}}\right) = \tilde{\varepsilon}\left(\boldsymbol{\varepsilon}^{\mathrm{p}}\right) - \kappa_{\mathrm{d}}. \tag{2.12}$$

In contrast to pure damage models where the damage evolution is controlled by the total strain, in this case, it is controlled by the plastic strain $\boldsymbol{\varepsilon}^{\mathrm{p}}$. The equivalent strain $\tilde{\varepsilon}$ is defined using a rate equation

$$\dot{\tilde{\varepsilon}} = \begin{cases} 0 & \text{if } \kappa_{\mathrm{p}} < 1 \\ \dot{\varepsilon}_{\mathrm{pV}} / x_{\mathrm{s}}\left(\bar{\sigma}_{\mathrm{V}}\right) & \text{if } \kappa_{\mathrm{p}} \geq 1 \end{cases}, \tag{2.13}$$

where $\dot{\varepsilon}_{\mathrm{pV}}$ represents the volumetric plastic strain rate and x_{s} is a softening ductility measure. The evolution law for the damage variable ω is assumed to have the exponential form

$$\omega = 1 - \exp\left(-\kappa_{\mathrm{d}} / \varepsilon_{\mathrm{f}}\right), \tag{2.14}$$

where ε_{f} is a parameter that controls the slope of the softening curve. The superposition between numerical and experimental loading results from [22, 23] has shown that the plastic-damage model was suitable for predicting the failure of concrete in axial, bi-axial and tri-axial cyclic compression, and in uniaxial cyclic tension . Moreover, it was able to describe the stiffness degradation observed experimentally during the cyclic loading in compression and tension. However, as the Lee and Fenves model, it does not capture the experimental closed loops that concrete exhibits under uni-axial cyclic compression or tension loads. Moreover, this model is not able to describe the stiffness recovery effect. In order to include the stiffness recovery effect, Grassl et al. [27] have later improve this model by considering a decomposition of the total damage variable into a compression and a

tension one.

Many other researchers have coupled plasticity and CDM in order to model the cyclic behaviour of concrete [28–33]. However, these models present some limitations for the fatigue modeling of concrete. First of all, they do not take into account the creep behaviour of concrete. In fact, Experimental results [38–40] corroborate the idea that it exists an evident correlation between creep and damage of concrete, especially with regards to HCF for which failure can occurs after several years. In the literature, the most part of concrete models in which the creep behaviour of concrete has been modeled considers a combination between creep and damage only [41, 119, 120]. Usually, combined models including time-dependent effects, damage, and plasticity, are such that, the viscous behaviour of concrete is modelled using rate-dependent plasticity or damage [121–127]. But these models are mere viscous regularization of plastic or damage models in order to optimize the stabilization scheme, rather than creep models based on phenomenological or experimental tests. In the literature, some researchers have used phenomenological creep models combined with damage to simulate the behaviour of concrete materials [41–45]. However, these models are not able to simulate the plastic, creep and damage behaviour effects, including multi-axial stress states and local confinement effect at the same time.

Moreover, the classical plasticity theory, coupled with the Continuum Damage Mechanics, is not sufficient to describe the damage response of brittle material such as concrete, when subjected to loads of low amplitude. In fact, even though such models accurately reproduce the mechanical behavior of concrete under static tension and compression, and cyclic loads of increasing amplitude, they do not predict deterioration during repeating loading–unloading cycles to constant amplitude, when the applied maximum stress lies below the yield/damage surface [34, 36]. It is thus necessary to modify the classical approach of the yield concept, in order to allow for plastic flow or damage accumulation, even for stress states below the yield/damage surface.

2.3 Fatigue damage models of concrete

Several phenomenological and mathematical models have been developed for the numerical simulation of concrete fatigue behaviour and fatigue life prediction. Despite the significant efforts that have been made, the numerical simulation of concrete remains challenging due to its strong heterogeneity and micro-structural complexity. Commonly used models for the fatigue simulation of concrete can be subdivided into four main groups: models based on the lifetime curves, models based Fracture Mechanics, models based on Continuum Damage Mechanics (CDM), and models based on Discrete Element Method (DEM). In the following sections, each group will be described, with a particular attention to models based on CDM, as the framework of the constitutive model presented in this work falls into this category.

2.3.1 Models based on lifetime approach

Models based of lifetime approach are phenomenological models in which analytical and empirical formulae are derived to approximate the strain development [15–17, 128–131], or the damage development[132–134], as functions of the number of cycle of load performed and the number of cycle to failure based on experimental data. The failure criterion is based on the Miner hypothesis of cumulative damage, that assumes the linear accumulation of damage with the cycles of load. For a given stress amplitude, the damage is evaluated as the number of cycles of load performed over the number of cycles of load to failure for the given stress amplitude. The total damage due to a combination of fatigue loads with various stress amplitudes is evaluated as the sum of the partial damages corresponding to each stress amplitude. The failure is reached when the total damage is equal to one [97]. This approach has two main drawbacks. First, experimental evidences show that the damage accumulation in concrete specimen due to fatigue is actually non-linear. Indeed, the miner rule cannot account for the effects of loading sequence, leading to overly-conservative or non-conservative fatigue life prediction [18]. Second, the experimental-based nature of this approach does not allow for a deeper insight in the physical mechanisms behind the fatigue failure of concrete materials and cannot be coupled with additional effects such as creep, shrinkage, strain rate effects,

just to name a few [34].

2.3.2 Models based on Fracture Mechanics

The second group of models consider non-linear fracture mechanics to study the crack propagation in solid bodies. The non-linearity is usually represented at the crack tip where stress concentrations are observed. Models based on Paris law [34] that gives the stable crack growth equation by relating the rate of crack length per cycle to the stress intensity factor, have been widely used to predict the crack propagation in concrete materials [135–138]. However, these models usually study the evolution of a predefined crack of relatively large size, which is incompatible with the heterogeneous nature of concrete in which several micro-crack of various lengths and orientations emerge and grow gradually, until coalescing into a meso- or macro-crack. Therefore, the Paris law was extended to account for size-effect by introducing new model parameters such as the fracture toughness and the brittleness number [139, 140]. Later, Kirane et al. [141] have refined the size-effect for quasi brittle materials through the microplane model, leading to fatigue transitional size values more consistent with the cyclic fracture process zone size. Despite the significant efforts made to simulate the fatigue behaviour of concrete materials through the non-linear fracture mechanics, the localized nature of the crack considered in these models makes this approach non-realistic for concrete like materials [142].

2.3.3 Models based on Continuum Damage Mechanics

In order to overcome the issues related to fracture mechanics, many researchers have used approaches based on continuum damage mechanics to simulate the fatigue behaviour of concrete. It assumes material homogeneity over a representative volume element (RVE), with micro-structural defects which sizes are much smaller than the RVE. The key point of this approach is based on the effect that the micro-defects have on macroscopic physical quantities such as the stiffness, that can be observed on an experimental basis. The extensive employment of this technique to reproduce numerically the concrete fatigue and damage behaviour can be explained by three points. First of all, it is suitable to model materials which contain a lot of micro-defects whose orientation, size

and distribution are a priori unknown, as in concrete. Second, it is particularly useful to model the damage accumulation prior to the formation of macro-cracks. This is especially true for high cycle fatigue of concrete, for which almost no change in the crack pattern during fatigue loading could be detected during the decay and steady stages that account for 90-95 % of the concrete fatigue life. Finally it can be easily coupled with the plasticity theory to account for permanent deformations. Many researchers have combined the theory of plasticity with continuum damage mechanics to reproduce the behaviour of concrete subjected to cyclic loads. Some of them have been described in Section 2.2 [19, 20, 24, 25, 27–33, 50, 93, 117]. In these models, damage accumulates as soon as the stress state lies on the damage or yield surface in the principal stress space. Such models can describe adequately the damage accumulation or permanent strain growth of concrete materials subjected to static compression or tension, or to cyclic loads with increasing amplitude. However, they are unable to predict accurately the damage or plastic strain accumulation of concrete under repeated loading-unloading cycles with constant amplitude. In the case of LCF, in which the maximum applied maximum stress could lie outside the yield/damage surface, the damage or plastic strain would accumulate and saturate only after the first cycle of load. In the case of HCF in which the maximum applied stress lies below the yield/damage surface, neither damage nor plastic strain accumulation will be observed. Therefore, the classical theory of plasticity or damage need to be extended for an accurate prediction of fatigue degradation of concrete material subjected to cyclic loads of constant amplitude. Several approaches have been proposed in literature for the numerical simulation of fatigue damage of concrete materials in the framework of continuum damage mechanics. Some of them are described in the following sections.

2.3.3.1 Marigo's formulation of fatigue damage.

Marigo [35] has proposed a strain-based damage model to accurately described the damage accumulation under repeated loads with a constant stress amplitude below the yield or damage surface. To this aim, the classical yield concept has been replaced by the loading-unloading irreversibility concept. A classical static damage model is described by the damage loading function, the damage

variable evolution law, and the loading-unloading conditions according to the Kuhn-Tucker relations

$$\begin{aligned} & f_d(\boldsymbol{\varepsilon}, \kappa_d) = \tilde{\varepsilon}(\boldsymbol{\varepsilon}) - \kappa_d, \\ & \omega = g_d(\kappa_d), \\ & f_d \leqslant 0, \quad \dot{\kappa}_d \geqslant 0, \quad \dot{\kappa}_d f_d = 0, \end{aligned} \tag{2.15}$$

where f_d is the damage loading function, $\tilde{\varepsilon}$ is an equivalent strain measure, κ_d is the internal variable controlling the damage evolution. ω and g_d are the damage variable and damage function, respectively. The damage loading function can be normalized by defining an equivalent gauge function $\tilde{f}_d$, such that

$$0 \leqslant \tilde{f}_d(\boldsymbol{\varepsilon}, \kappa_d) \leqslant 1. \tag{2.16}$$

If $0 \leqslant \tilde{f}_d(\boldsymbol{\varepsilon}, \kappa_d) < 1$, the state $(\boldsymbol{\varepsilon}, \kappa_d)$ is below the damage surface and no damage occurs. However, if $\tilde{f}_d(\boldsymbol{\varepsilon}, \kappa_d) = 1$, then the state $(\boldsymbol{\varepsilon}, \kappa_d)$ is on the damage surface. If further damage takes place, the consistency condition can be written as $\dot{\tilde{f}}_d(\boldsymbol{\varepsilon}, \kappa_d) = 0$. Combining the consistency conditions with the Kuhn-Tucker relations yield

$$\dot{\kappa}_d = \begin{cases} 0 & \text{if} \quad 0 \leqslant \tilde{f}_d(\boldsymbol{\varepsilon}, \kappa_d) < 1 \\ \\ \langle \frac{\partial \tilde{\boldsymbol{\varepsilon}}(\boldsymbol{\varepsilon}, \kappa_d)}{\partial \boldsymbol{\varepsilon}} : \dot{\boldsymbol{\varepsilon}} \rangle^+ & \text{if} \quad \tilde{f}_d(\boldsymbol{\varepsilon}, \kappa_d) = 1, \end{cases} \tag{2.17}$$

where $\langle x \rangle^+$ represents the positive part of the quantity x, which is equal to zero if $x < 0$ and x if $x \geqslant 0$. The static damage model described till now is unable to predict damage accumulation under cyclic loading of constant amplitude and stress level below the yield surface. In order to extend it to a fatigue damage model, Marigo have proposed to replace the yield concept with a loading-unloading irreversibility concept. Therefore, the constrained damage flow rule reported in Eq. 2.17 is replaced by the unconstrained damage evolution reported here-below

$$\dot{\kappa}_d = H(\tilde{f}_d(\boldsymbol{\varepsilon}, \kappa_d)) \langle \frac{\partial \tilde{\boldsymbol{\varepsilon}}(\boldsymbol{\varepsilon}, \kappa_d)}{\partial \boldsymbol{\varepsilon}} : \dot{\boldsymbol{\varepsilon}} \rangle^+, \tag{2.18}$$

where $H(\tilde{f}_d(\boldsymbol{\varepsilon}, \kappa_d))$, called herein the fatigue function, is any continuous and increasing function of the gauge function, such that $H(0) = 0$ and $H(1) = 1$. It is important to mention that, the quantity $\frac{\partial \tilde{\boldsymbol{\varepsilon}}(\boldsymbol{\varepsilon}, \kappa_d)}{\partial \boldsymbol{\varepsilon}} : \dot{\boldsymbol{\varepsilon}}$ is interpreted as the loading-unloading criterion. In fact, damage evolves when the later is positive and does not accumulate when it is negative. Many choices are possible for the function H. Marigo has proposed a power law for H

$$H(\tilde{f}_d) = (\tilde{f}_d)^n, \tag{2.19}$$

where n is a material parameter. In the special case if which $H(\tilde{f}_d) = \langle \tilde{f}_d - 1 \rangle^+$, the fatigue damage evolution reported in Eq. 2.18 become equivalent to the static damage formulation reported in Eq. 2.17. It is worth to mention that any local static damage model based on a yield concept can be extended to a fatigue damage model, by means of the Marigo's formulation. Many scholars have used the Marigo's formulation for the damage fatigue modeling of concrete [31, 34, 36, 37, 100, 143]. In the works of [37], the damage criterion is formulated in the strain space and the equivalent strain is based on the volumetric energy norm. By using the Marigo's appraoch, the function $H(\tilde{f}_d)$ have been defined using a bi-power law, requiring a total of 3 additional material parameters, $n_1 > 0$, $n_2 > 0$, and $0 < \alpha \leqslant 1$

$$H(\tilde{f}_d) = \begin{cases} \alpha^{n_1} \left(\frac{\tilde{f}_d}{\alpha} \right)^{n_2} & \text{if} \quad 0 \leqslant \tilde{f}_d \leqslant \alpha, \\ (\tilde{f}_d)^{n_1} & \text{if} \quad \alpha \leqslant \tilde{f}_d \leqslant 1. \end{cases} \tag{2.20}$$

In this manner, a greater flexibility in catching the experimental results can be achieved. Despite the fairly well superposition with experimental results, especially with the number of cycles to failure, this model fails to catch the accumulation of permanent strains in the three-stage pattern observed experimentally.

Most recently, Liang et al. [31] has proposed a double-scalar elasto-plastic constitutive model of concrete, able to account for permanent deformations and for damage accumulation even for cyclic loads of constant amplitude with maximum stress below the yield surface. The plastic formulation of the model is based on an empirical plastic flow parameter [144], in which plastic strains are proportional to the effective stress. In this way, the low computational efficiency usually observed

in the classical theory of plasticity due to the large number of iterations can be avoided. On the other hand, the damage formulation of the model is developed in the framework of irreversible thermodynamics, where the damage energy release rate is used as the driving force for the internal damage variable. The extension to the fatigue damage is done using the Marigo's formulation, in which the fatigue function has a power-law. The three-stage pattern of the plastic strain development observed during fatigue degradation is explained by the competition between the damage driving effect and the damage healing effect, due to the growth, and closure of micro-defects, respectively. The model is able to describe fairly well the concrete tensile and shear fatigue behaviour under complex fatigue loads, and can accurately predict the three-stage pattern of permanent strain accumulation.

2.3.3.2 The two-scale model for fatigue damage.

Lemaitre et al. [8] have proposed a two-scale model for damage at the microscale, for the numerical simulation of quasi-brittle failure or high-cycle fatigue. The model is based on the physical observation that, even if the load at the classical scale of the continuum mechanics (mesoscale) is below the conventional yield stress, plasticity and damage can occur at a smaller scale (microscale). The proposed two-scale model is able to account for this scale effect by considering a "*weak*" inclusion at the microscale, inside the RVE at the mesoscale, as shown in Fig. 2.1.

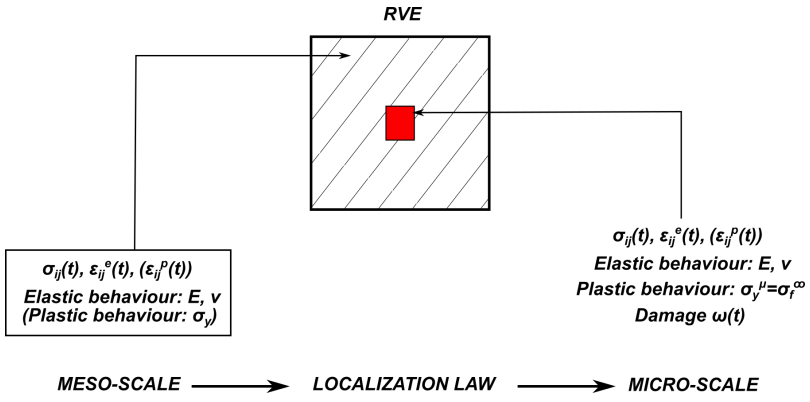

Figure 2.1: Schematic representation of the two-scale damage model.

On the mesoscale, in a general case, a full elasto-visco-plastic model could be considered, while in the specific cases of quasi-brittle failure or high cycle fatigue, only elasticity is considered. However, on the microscale, the "*weak*" inclusion is modelled with a plastic-damage model and it is the only part on the material for which damage is allowed. In the original formulation of the two-scale model, the asymptotic fatigue limit σ_f^∞ is considered as the limit criterion for damage initiation and growth. The damage loading function can consider both isotropic and linear kinematic hardening. In the simplified case in which only kinematic hardening is assumed at the microscale, the following yield criterion has been used

$$f^\mu = \left(\frac{\boldsymbol{\sigma}^\mu}{1-\omega} - \boldsymbol{X}^\mu \right)_{\text{eq}} - \sigma_f^\infty, \tag{2.21}$$

where the superscript μ is used to denote the quantities computed at the microscale. The quantities $\boldsymbol{\sigma}^\mu$ and $\boldsymbol{X}^\mu$ represent the total stress and the microscale back-stress respectively, while ω is the scalar damage variable. The Von-Mises norm is used for the calculation of the equivalent stress for the yield criterion. The microscopic damage growth is governed by the plastic strain rate $\dot{\boldsymbol{\varepsilon}}^p$, and considers the elastic energy density denoted here by Y. It takes the following expression in the rate form

$$\dot{\omega} = \left(\frac{Y}{S} \right)^s \dot{\boldsymbol{\varepsilon}}^p, \tag{2.22}$$

where S and s are the damage material parameters at the microscale. The transition from the mesoscale to the microscale is achieved by means of the d Eshelby–Kröner localization law [145], which relates the total and plastic strains at the mesoscale to the ones at the microscale.

A more suitable formulation of the two-scale fatigue damage for quasi-brittle material has been proposed by Desmorat et al. [146], to account for the fact that a damage growth governed by the plastic strain rate is not always representative of such materials. To tackle this issue, they have proposed for the microscopic formulation of the damage, an evolution law based on the equivalent strain rate or on the generalized Lemaitre's approach of a damage, in which by the main dissipative mechanism is the internal friction encountered in these materials.

Later, Desmorat et al. [147], has extended the two-scale damage model to account for anisothermal effects, and then for thermo-mechanical fatigue. This is a relevant aspect for fatigue modelling

of concrete, since experimental evidences show that, several factors can affect the temperature rise on concrete specimens during cyclic test, especially for HCF testing [148].

The two-scale fatigue damage model of Lemaître and Desmorat model turns out to describe fairly well many non-linear characteristics that concrete materials exhibit under high-cycle fatigue loads such as the mean stress effect, the nonlinear accumulation of damage, initial strain hardening or damage effect and the non-proportional loading effect for bi-axial fatigue.

2.3.3.3 Fatigue models based on bounding surfaces.

The concept of bounding surface has been developed by Dafalias et al. [149] for metals, in order to overcome the inadequacy of classical plasticity models to describe realistically the material response under complex loading paths including cyclic loading. In contrast to classical plasticity models, models based on bounding surface can simulate stress histories with loading-unloading cycles of constant amplitude, because they allow for damage of plastic evolution for stress states below a limit surface, called bounding surface. Furthermore, they have the advantage to capture very well the hysteretic behaviour of material, by allowing for a smoother transition from the elastic range to the elasto-plastic range.

The salient features of bounding surfaces models can be summarized as follows:

1. A yield surface may exists, which encloses the purely elastic domain, similarly to the concept of yield surface in the classical plasticity approach.

2. A bounding surface exists, which is no longer the boundary between elastic and plastic deformations as in the classical plasticity theory, but it encloses the yield surface, which can moves in the stress space, but within the bounding surface. The bounding surface can translate in the stress space, and possibly deform.

3. Any stress state between the yield and the bounding surface is described by a loading surface which can translate, and possibly deform is the stress space according to a selected hardening rule. The hardening rule is usually a function of the plastic modulus H^p. Non-zero strains are allowed inside the bounding surface, by defining the plastic modulus and other material

properties as function of the distances d and d_{max}. d represents the distance between the current stress point on the loading surface and an arbitrarily defined image stress point on the bounding surface, while d_{max} is the distance between the stress point at the initiation of yielding and the image on the bounding surface

$$H^p = \hat{H}^p(d, d_{max}). \tag{2.23}$$

From Eq. 2.23, $H_0^p = \hat{H}^p(0, d_{max})$ represents the plastic modulus when the intersection between the loading surface and the bounding surface occur; $\hat{H}^p(d_{max}, d_{max})$ is the value of the plastic modulus at the initiation of yielding, equal to ∞, for a smooth transition from the elastic to the elasto-plastic region. The function $\hat{H}^p(d, d_{max})$ is an absolutely increasing function of d. In order to get the image stress point on the bounding surface, a proper mapping rule must be defined. Amongst them, the radial mapping method, proposed by Yang et al. [150], in which the image stress point is determined by the intersection of the vector linking the origin of the stress space to the current stress, with the bounding surface. Another mapping rule consists of considering the intersection point of the normal at the current stress on the loading surface, with the bounding surface [151]. If the yield and the bounding surfaces are circular or elliptical in shape, the image point can be obtained by the intersection between the vector linking the center of the yield surface and the current stress point, with the bounding surface [151]. A schematic representation of the radial mapping method is reported in Fig. 2.2.

Many models based on the bounding surface concept have been employed to describe the fatigue behaviour of concrete-like materials [150, 152–159]. They differ in terms of the bounding surface equation, the mapping rule for the image stress point, and the evolution law of constitutive parameters.

The concept of bounding surface was first applied to concrete by Fardis et al. [152]. A bounding surface plasticity model has been developed, in which the bounding surface has a quadratic expression, and shrinks in size once the maximum strain experienced by the material exceeds a predefined

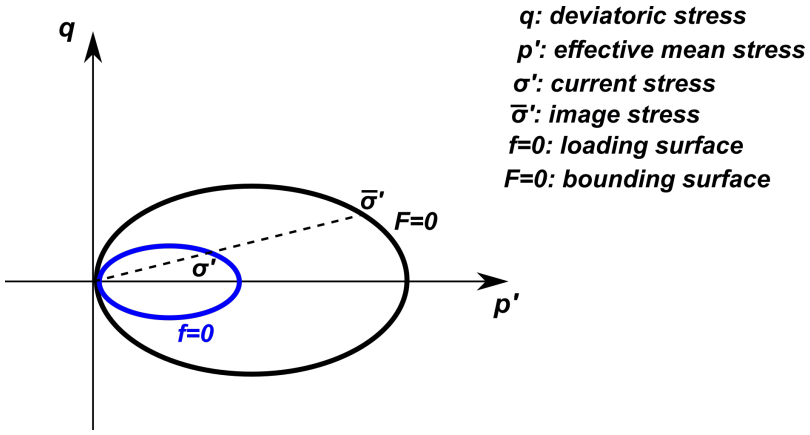

Figure 2.2: Schematic representation of the radial mapping method.

value. The proposed bounding surface takes the following expression

$$F = \left[\frac{I_1}{f_c} + \left(\frac{a}{3} + \frac{b}{\sqrt{3}} - 1\right)\right] g(\varepsilon_{\max}) \mp \left[a\left(\frac{\sqrt{J_2}}{f_c}\right)^2 + b\frac{\sqrt{J_2}}{f_c}\right] = 0, \tag{2.24}$$

where I_1 and J_2 are the first and the second deviatoric stress invariant, respectively. a and b are material parameters and f_c is the compressive strength of concrete. The function $g(\varepsilon_{\max})$ controls the reduction in size of the bounding surface. In Eq. 2.24, the plus sign applies to compression tests, while the minus sign applies to tension tests. The distance d between the current stress state and the stress point image on the bounding surface is computed considering the direction of the instantaneous stress increment. The constitutive parameters are provided as a function of the ratio d/d_{max}, for virgin loading, unloading, and reloading. Pandolfi et al. [157] have assessed the potentiality for four fatigue damage models of concrete based on the bounding surface concept, including the Fardis et al.'s model [154]. It came out that, the model was able to predict quite well the increase in fatigue life with decreasing cycle amplitude and maximum stress. However, it was unable to describe the hysteresis loops only for sufficiently large cycle amplitude, for uniaxial cyclic tests with equal maximum stress. Furthermore, an underestimation of the experimental fatigue life was observed, due to the rate-independent nature of the model, as explained by Pandolfi et al. [157].

More recently, Lu et al. [158], has proposed a damage constitutive model for concrete subjected to uniaxial alternate tension–compression fatigue loading. The model require the definition of an initial damage surface, a loading surface and a bounding surface. They have a spherical shape in the strain-release energy space, and have expressions similar to the bounding surface model proposed by Suaris et al. [155]. The initial damage surface f_0, the loading surface f, and the bounding surface F have the following expressions

$$\begin{aligned} f_0 &= (R_i R_i)^{1/2} - R_0 = 0 \\ f &= (R_i R_i)^{1/2} - R_l/b = 0 \\ F &= \left(\bar{R}_i \bar{R}_i\right)^{1/2} - R_l = 0, \end{aligned} \tag{2.25}$$

where R_i is the thermodynamic-force conjugate, and $\bar{R}_i = bR_i$, the image point of the bounding surface. The radial mapping rule is used, and the mapping parameter b ranges from an initial value of ∞ to 1. R_0 is the value of the thermodynamic-force conjugate at the initiation of damage. In the Lu et al.'s fatigue damage model, the damage depends on a damage modulus H, expressed as a function of the distance d between the loading and the bounding surfaces, and the distance d_{max} between the initial damage and the bounding surfaces. The good juxtaposition between the numerical and experimental results indicates the capability of the model to predict the stress-strain response of concrete subjected to stress reversal.

Wen et al. [160] has proposed a unified approach to model the anisotropic and biaxial fatigue damage of woven composites by utilizing a simplified version of the bounding surface approach. It is an intuitive extension of the non-linear quasi-static damage mechanics to fatigue modeling. The simplified bounding surface approach considers a limit surface called "LS", which represents the strength envelope of the material in a non-fatigue or quasi-static environment. As the number of cycles of loading increase in a fatigue environment, the strength envelope collapse inwards to account for the decrease in the ultimate strength of the material due the growth and coalescence of inherent micro-defects (Fig. 2.3).

The new surfaces obtained after the material has undergone fatigue damage are called residual surface ("RS"). Therefore, the simplified bounding surface approach aims at utilizing the damage

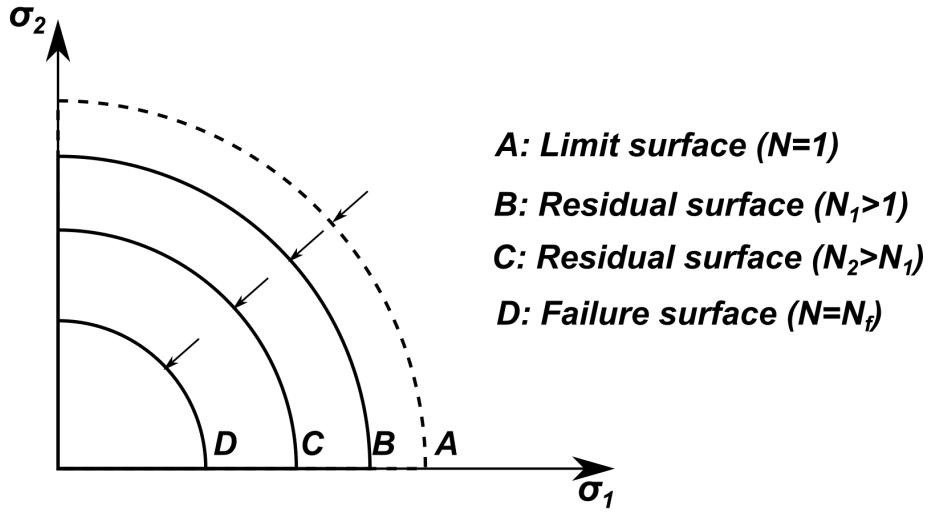

Figure 2.3: 2D schematic representation of the bounding surfaces in the stress plane.

mechanics framework to develop a realistic equation of the limit surface and to propose a evolutionary equation for the residual strength surfaces. Starting from the he standard thermodynamics framework, the potential damage function ψ for quasi-static damage is written in the bi-axial stress space as

$$\psi(\boldsymbol{\sigma}, k) = \frac{1}{2}(1+\alpha+2\beta)\boldsymbol{\sigma}:\boldsymbol{\sigma} - \frac{1}{2}\alpha[\mathrm{Tr}(\boldsymbol{\sigma})]^2 - \frac{1}{2}\left[\frac{\boldsymbol{\sigma}:\boldsymbol{S}}{\mathrm{Tr}(\boldsymbol{\sigma})}q(k)\right]^2 = 0, \tag{2.26}$$

where $\mathrm{Tr}(\boldsymbol{\sigma})$ represents the trace of the stress tensor. The scalars α and β are material parameters, and $q(k)$ can be interpreted as the shape function of the damage function, with a maximum value equal to one. $\boldsymbol{S}$ is a strength tensor defined as a function of the material strength in each direction, and k is the damage parameter. Eq. 2.26 represents the limit surface in a quasi-static environment. In order to account for fatigue, a softening function F has been introduced, as a function of the number of cycles of load n, in the expression of the damage function

$$\psi(\boldsymbol{\sigma}, k) = \frac{1}{2}(1+\alpha+2\beta)\boldsymbol{\sigma}:\boldsymbol{\sigma} - \frac{1}{2}\alpha[\mathrm{Tr}(\boldsymbol{\sigma})]^2 - \frac{1}{2}\left[\frac{\boldsymbol{\sigma}:\boldsymbol{S}}{\mathrm{Tr}(\boldsymbol{\sigma})}F(n)q(k)\right]^2 = 0. \tag{2.27}$$

As the number of cycles of load increases, $F(n)$ gradually decreases, from the value 1 that rep-

resents the limit surface, to smaller values, representing the residual strength surfaces. Based on experimental fatigue life curves, a power function has been used for the softening function F

$$F(n) = n^A, \tag{2.28}$$

where A is a material parameter. Finally, the damage parameter k is defined in the rate form as

$$\frac{\mathrm{d}k}{\mathrm{d}n} = \frac{1}{E_0(1+\beta)}(-A)\left(n^{-A-1}\right), \tag{2.29}$$

where E_0 is the undamaged Young's modulus.

Yadav et al. [161] have proposed a similar model based on the continuum damage mechanics theory to model the fatigue behaviour of concrete. The main difference with the model of Wen et al. is that, the proposed model uses a strain-based approach. In this case, the residual surfaces do not reduce in size as in the Wen's model, but continuously expand until the failure surface is reached (Fig. 2.4)

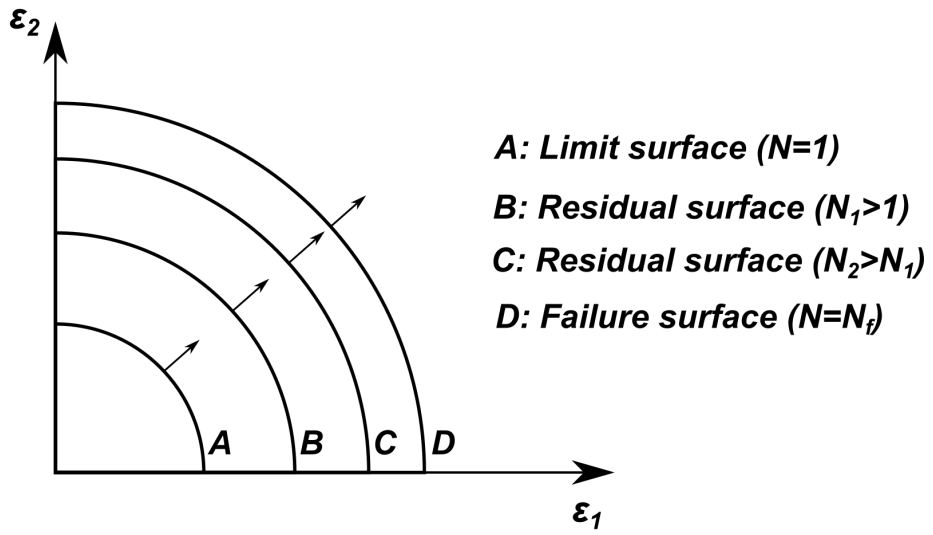

Figure 2.4: 2D schematic representation of the bounding surfaces in the strain plane.

The damage function is the strain space, and in a quasi-static environment is expressed as

$$\mathrm{p}_{static}(\boldsymbol{\varepsilon}, \mathrm{k}) = \left(\varepsilon_{\mathrm{c}}\sqrt{1+2\alpha v^2}\right)\ln\left(\frac{\mathrm{E}_0}{\mathrm{E}_0-\mathrm{k}}\right) = \varepsilon_0 \ln\left(\frac{\mathrm{E}_0}{\mathrm{E}_0-\mathrm{k}}\right), \tag{2.30}$$

where ε_{c}, E_0, ε_0, and v_0, are the ultimate strain corresponding to peak stress, initial Young's Modulus of elasticity, referential strain, initial Poisson's ratio of the concrete material respectively. The function ln represents the natural logarithm. The scalar k represented the accumulated damage variable.

In a fatigue environment, the damage surface from Eq. 2.30 is modified by a *hardening* function, which causes it to expand from the limit surface corresponding to a number of cycles of load equal to one, to the failure surface, corresponding to the number of cycles to failure . The extended damage function takes the following expression

$$\mathrm{p}_{fatigue}(\boldsymbol{\varepsilon}, \mathrm{k}, \mathrm{n}, \mathrm{r}) = \mathrm{G}(\mathrm{n}, \mathrm{r}) \cdot \mathrm{p}_{static}(\boldsymbol{\varepsilon}, \mathrm{k}), \tag{2.31}$$

where $\mathrm{G}(\mathrm{n}, \mathrm{r}) = n^{\lambda(1-r)}$ represents the *hardening* function, λ is a material parameter and r is the stress ratio. The scalar cumulative damage variable k is defined in its rate form as

$$\dot{\mathrm{k}} = \mathrm{A}\left(\frac{\sqrt{\boldsymbol{\varepsilon}^- : \boldsymbol{\varepsilon}^-}}{\varepsilon_0}\right)^{\mathrm{B}(1-\mathrm{r})} n^{\mathrm{C}}, \tag{2.32}$$

where A, B and C are material parameters, and $\boldsymbol{\varepsilon}^-$ is the negative cone of the strain tensor.

2.3.3.4 Microplane models

Microplane models were conceived originally by Bažant [162]. Inspired by the works of Taylor et al. [163] on plasticity of polycrystalline metals, the microplane models consider concrete as a material lattice at the mesoscale, with the cement and the aggregates having a crystal structure. The constitutive relationship between the stress and the strain components are defined on hypothetical planes surrounding the material point, called microplanes. Therefore, an additional level of representation (microscale) is introduced below the scale of the material point (macroscale). The advantage of the microplane model is that it can capture the oriented nature of damage and the

anisotropy of materials over the different microplanes.

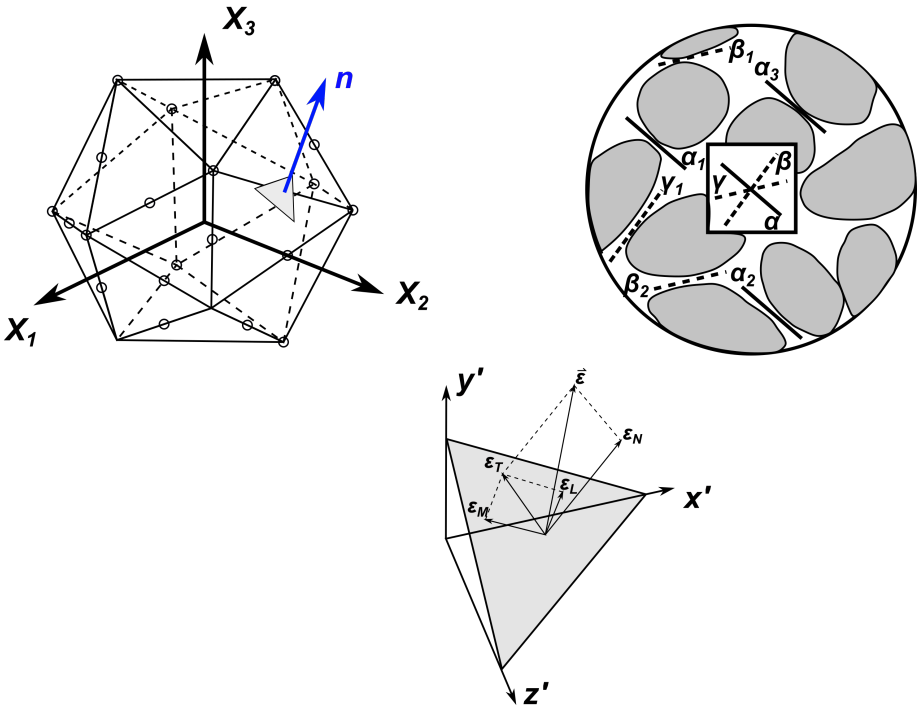

Figure 2.5: schematic representation of the microplane model [164].

Figure 2.5 depicts a material point surrounded by microplanes. Each microplane is identified by distinct orientation, defined by a unit normal vector $\boldsymbol{n}$. Two orthogonal directions, $\boldsymbol{m}$ and $\boldsymbol{l}$ are defined parallel to each microplane. The transition from the macroscale strain tensor to the microscale strain vector is obtained by projections of the strain tensor along the directions $\boldsymbol{n}$, $\boldsymbol{m}$, and $\boldsymbol{l}$, according to the following expressions

$$\varepsilon_N = N_{ij}\varepsilon_{ij}, \quad \varepsilon_M = M_{ij}\varepsilon_{ij}, \quad \varepsilon_L = L_{ij}\varepsilon_{ij}, \tag{2.33}$$

where the subscripts i, $j = 1, 2, 3$ represents the cartesian directions on the global reference system, and $N_{ij} = n_i n_j, M_{ij} = (m_i n_j + m_j n_i)/2, L_{ij} = (l_i n_j + l_j n_i)/2$ are the normal and the tangential mutually orthogonal vectors, obtained by the projections of the unit vectors $\boldsymbol{n}$, $\boldsymbol{m}$, and $\boldsymbol{l}$, respectively, on the global cartesian directions. The relationship between the microscopic stress vector

components $\boldsymbol{\sigma}_N$, $\boldsymbol{\sigma}_M$, $\boldsymbol{\sigma}_L$ along the directions $\boldsymbol{n}$, $\boldsymbol{m}$, and $\boldsymbol{l}$ respectively, and the macroscopic stress $\boldsymbol{\sigma}$ at the material point, is obtained approximately, by ensuring equilibrium through the principle of virtual work [162]

$$\sigma_{ij} = \frac{3}{2\pi} \int_{\Omega} s_{ij} d\Omega \approx 6 \sum_{\mu=1}^{N_m} w_\mu s_{ij}^{(\mu)}, \tag{2.34}$$

with $s_{ij} = \boldsymbol{\sigma}_N N_{ij} + \boldsymbol{\sigma}_L L_{ij} + \boldsymbol{\sigma}_M M_{ij}$. Ω is the surface of a unit hemisphere, having center at the material point, and volume equal to $2\pi/3$. The sum at the right hand-side of Eq. 2.34 is an approximation of the integral, based on an optimal Gaussian integration for a spherical surface, with weights w_μ, $\mu = 1, 2, ..., N_m$. Numerical experimentation by Bažant et al. [165] have shown that at least 21 microplanes are needed for a proper capturing of the post-peak softening behaviour. The inelastic or damage behavior is enforced at the microplane stress level, by subjecting the microplane stresses $\boldsymbol{\sigma}_N$, $\boldsymbol{\sigma}_M$, $\boldsymbol{\sigma}_L$ to strain-dependent strength limits called stress-strain boundaries, similar to the yield surface in the classical plasticity approach. Usually, four yield limits are identified: the volumetric boundary to capture phenomenon such concrete crushing under extreme compressive pressures; the deviatoric boundary to capture softening in compression; the normal boundary to capture tensile fracturing, and finally the shear boundary to capture friction. Examples of yield limits are reported in Fig. 2.6, from the works of Carner et al. [164]. Similarly to classical yield surface, the strain increment is assumed to be fully elastic at the beginning of the time internal into consideration, and the different stress components are evaluated accordingly. If the boundary of any of the above-mentioned strain-dependent strength surfaces is exceeded, the stress is corrected, by bringing it back to the boundary of the yield surface, at a constant strain.

A series of microplane models labeled M0, M1, M2, ..., M6 [162, 164, 166–170] have been developed for concrete material. Each model is an improvement of the previous version. In a similar way to the classical theory of plasticity, the model M0 [162] considers simultaneously the normal and shear strain components for the definition of the loading surface. This was found to be unnecessary, and improved in the model M1 [166], which was accounting for strain softening behaviour and focusing on uniaxial tensile behaviour. The model M2-M6 where able to model the compressive behaviour of concrete, considering the confinement effects. In order to avoid the

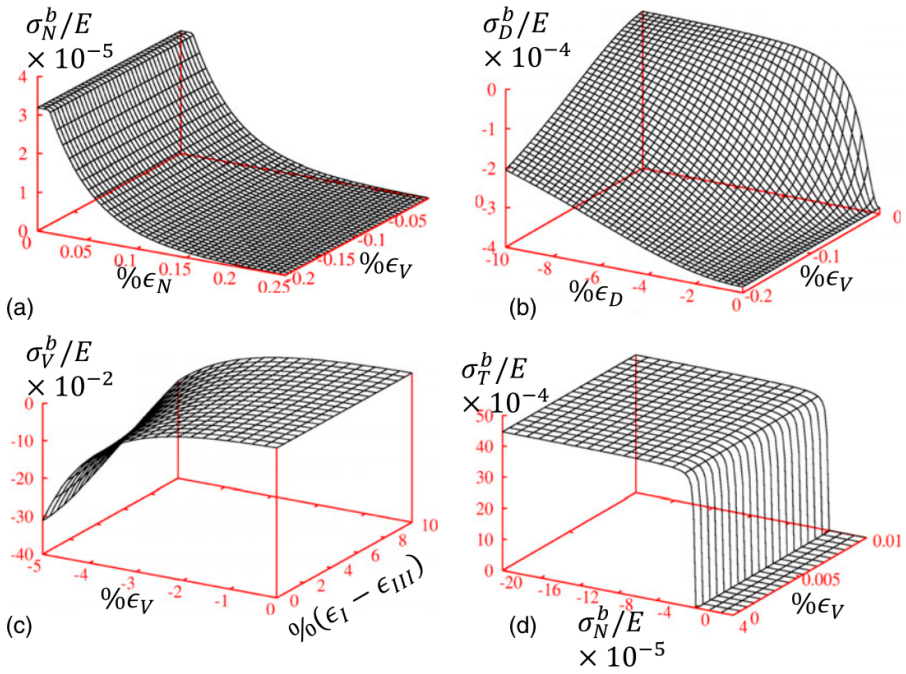

Figure 2.6: Microplane stress-strain boundaries used in model M7: (a) normal boundary; (b) deviatoric boundary; (c) volumetric boundary; (d) plastic-frictional boundary [164].

excessive lateral expansion and the axial stress locking observed in the previous models, the more recent M7 model [164], was developed by considering the volumetric-deviatoric split only for the compressive normal and deviatoric strain-dependent strength surfaces.

A common issue with the microplane models is related to the fact that they use a large number of phenomenological material parameters, and are therefore difficult to calibrate. To prevent unstable strain localization and pathological mesh sensitivity of microplane models, they have been used in combination with some non-local continuum formulation [171–173].

2.3.4 Mesoscale discrete models

Recently, the Discrete Element Method (DEM) has proven to be a powerful tool for the numerical simulation of the mechanical behaviour of cementitious materials. In the Discrete Element Method, the material is modelled as a packing of single particles, with defined physical properties and

kinematically independent equations of motion. The interaction between the particles is governed by contact models. In contrast to continuum models, the discontinuity represents an intrinsic property of the Discrete Element Method, making it suitable to model the complex heterogeneous structure of cementitious materials. Furthermore, the capabilities of the model to simulate large displacements, and the fact that the particles can detach from one to another, allow for a direct simulation of crack initiation and propagation. This is a relevant advantage with respect to continuum models, which require ad-hoc treatments in order to account for localized effects [174]. In order to reduce the computational cost of the Discrete Element Method, the particles shapes are usually simplified using spheres. Two main categories can be identified in the Discrete Element Method: soft sphere models, in which penetration is allowed at the contacts between particles, and hard sphere models, in which neither penetration, nor deformation of the particles are allowed.

During the last decades, the Discrete Element Method, has found many applications for the simulation of the mechanical behaviour of concrete and the reproduction of experimental results, especially with regards to compressive tests [175–177], flexural tests [178–180], and impact loads [181, 182]. However, only little contributions are found with regards to the response of cementitiuos materials to fatigue and cyclic loads[1, 174, 183]. Sinaie et al. [183] has developed a Discrete Element Model for the simulation of cyclic loading for concrete materials. A multi-phase modelling is considered, in which aggregates and mortar are differentiated. Furthermore, different cohesive parameters are used for the mortar-mortar bonds and for the aggregate-mortar bonds, allowing for the "weak" Interfacial Transition Zone (ITZ) to be taken into account. A micro-mechanical damage model including stress reversals is taken into account by a progressive degradation of the cohesive bonds and thus, of the strength, when the normal and shear cohesive forces reach their limits. More recently, Nguyen et al. [174] has coupled the plasticity theory and damage mechanics, including a fatigue damage evolution law, to describe the fatigue behaviour of concrete materials at the grain scale. Interestingly, the fatigue formulation allows for damage accumulation for stress states below the yield surface. The plasticity-damage model is based on the general framework of thermodynamics for dissipative materials [184], while the evolution of fatigue damage is described by the Paris's law. The coupled model has demonstrated good capabilities in capturing the variations

of stress-strain results, fatigue life, and crack patterns.

Another robust discrete numerical model that has been used to describe the behaviour of concrete under cyclic loading is Lattice Discrete Particle Model (LDPM) formulated at the mesoscale by Cusatis et al. [185]. In this model, the coarse aggregate particles are explicitly represented as rigid spheres within polyhedral cells, obtained after a Delaunay tetrahedralization on the centers of the spherical particles to generate a lattice system, and a dual domain tessellation. Each polyhedral cell contains an aggregate particle with surrounding matrix. The material behaviour is developed by means of rigid body kinematics. The robustness of the LDPM relies on its ability to produce realistic failure patterns thanks to its ability to represent individually each coarse aggregate [186]. In order to catch the mechanical behaviour of concrete under tri-axial cyclic loading, Zhu et al. [187] have recently proposed a modified set of constitutive equations for LPDM. The proposed model considers a modified volumetric–deviatoric compression law, and a modified frictional law under compression. Furthermore, the constitutive relationships related to the tension and shear stresses are established separately to ensure a smooth stress transition from tension to compression state. The model has been used to simulate the mechanical behavior and failure mode of concrete under tension–compression cycling and hydrostatic pressure, and under different levels of confinement. The superposition between numerical and experimental results has shown that the constitutive model is able to simulate the cyclic behaviour of concrete under different confinement pressures, and to catch the experimental failure patterns. Gan et al.[188] have proposed a 2D numerical model using lattice network in order to investigate the behaviour of the cement paste under fatigue loading. The lattice model is generated by means of X-ray Computed Tomography (XCT), in which the cement paste is discretized as a set of Timoshenko beam elements having linear elastic brittle behaviour. Fatigue degradation is taken into account by means of the phenomenological S-N curves, and fatigue accumulation is considered by means of the Miner's law. By comparison with experimental results, the proposed model was able to reproduce well the flexural fatigue experimental results, in terms of S-N curve, including stiffness degradation and permanent deformation.

Although the models described above have shown a good predictability of the non-linear behaviour of concrete, only few of them can simulate the behaviour of concrete under the simultaneous

effects of creep and fatigue. Moreover, there is a need of more comprehensive models able to reproduce the mechanical behavior of concrete materials subjected to fatigue loading in multi-axial stress conditions. The plastic damage formulation described herein uses a similar framework of the plastic damage models described above [20, 46, 111]. It is coupled with a phenomenological creep model to account for long-term loads. Moreover, the plastic damage model is extended to include a fatigue behaviour, by including a fatigue degradation function [59, 189] inside the formulation of the yield surface.

Chapter 3

Description of the proposed constitutive model

3.1 The plastic formulation of the model

The plasticity theory is used to treat the irreversible and permanent deformations induced by micro-cracking and slip within the concrete structure. A plastic model for concrete must include properties such as pressure sensitivity, path sensitivity, strain hardening, and brittle tensile behaviour. Three basic assumptions are required for the definition of a plasticity model:

- an initial yield surface, which encloses the initial elastic domain;
- a hardening/softening rule;
- and a flow rule.

3.1.1 The yield surface

The yield surface is described in terms of stress-invariants, using the Haigh–Westergaard (HW) coordinates (ξ, ρ, θ),

$$\xi = \frac{I_1}{\sqrt{3}}, \quad I_1 = \delta_{ij}\sigma_{ij}$$

$$\rho = \sqrt{2J_2}, \quad J_2 = \frac{1}{2}s_{ij}s_{ij}, \quad s_{ij} = \sigma_{ij} - \frac{1}{3}\delta_{ij}\sigma_{kk} \tag{3.1}$$

$$cos(3\theta) = \frac{3\sqrt{3}}{2}\frac{J_3}{J_2^{3/2}}, \quad J_3 = \frac{1}{3}s_{ij}s_{jk}s_{ki},$$

where: I_1 is the first invariant of the stress tensor; J_2 and J_3 are the second and third invariants of the deviatoric stress tensor; δ_{ij} is the Kronecker delta ($\delta_{ij} = 1$ if $i = j$, and $\delta_{ij} = 0$ if $i \neq j$). The geometrical interpretation of the HW coordinates in reported is Fig. 3.1.

The yield surface considered herein is expressed in agreement with the Ménétrey-Willam plastic surface [51]

$$f = 1.5\left[\frac{\rho}{(1-\omega^*)f_c}\right]^2 + \frac{q_h(\kappa)m}{(1-\omega^*)f_c}\left[\frac{\rho}{\sqrt{6}}r(\theta,e) + \frac{\xi}{\sqrt{3}}\right] - q_h(\kappa)q_s(\kappa) = 0, \tag{3.2}$$

where the elliptic function r is expressed as a function of the Lode angle θ, and the eccentricity parameter e

$$r(\theta,e) = \frac{4\left(1-e^2\right)\cos^2(\theta) + (2e-1)^2}{2(1-e^2)\cos(\theta) + (2e-1)\sqrt{4\left(1-e^2\right)\cos^2(\theta) + 5e^2 - 4e}}. \tag{3.3}$$

The friction parameter m in Eq. 3.2 is expressed as a function of the uniaxial compressive strength (f_c) and tensile strength (f_t) of concrete as

$$m = 3\frac{f_c^2 - f_t^2}{f_c f_t}\left(\frac{e}{e+1}\right). \tag{3.4}$$

The shape of the yield function in the deviatoric plane can change, using the eccentricity parameter $e = [0.5, 1]$ as reported in Fig. 3.2.

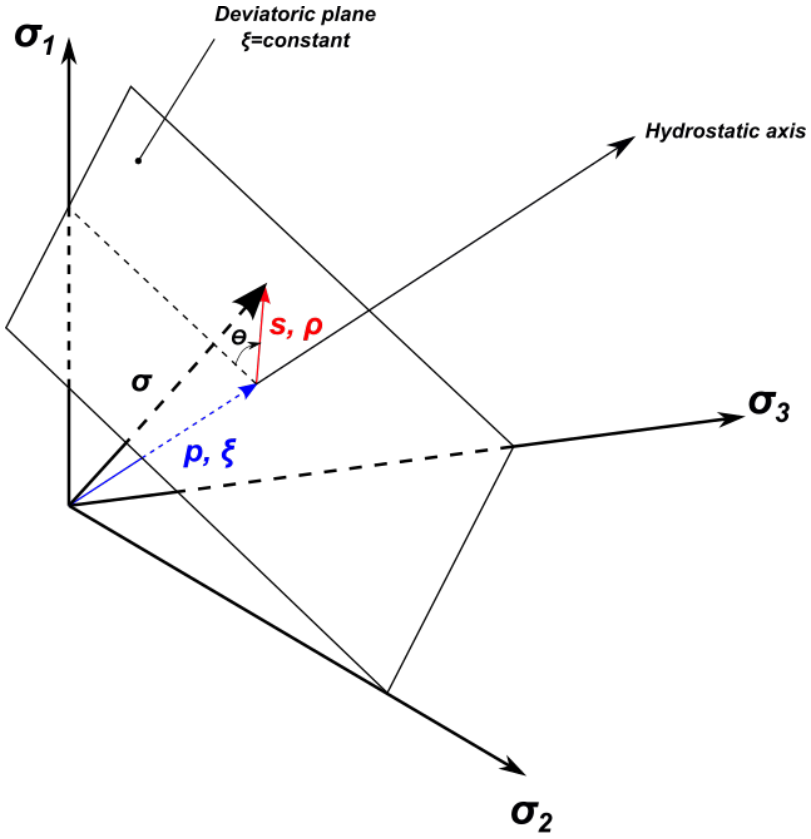

Figure 3.1: Haigh–Westergaard stress space.

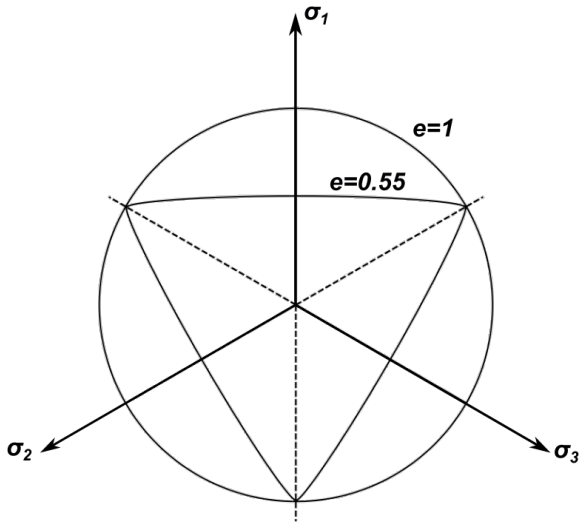

Figure 3.2: Shape of the deviatoric sections of the Ménétrey-Willam yield surface for e = 0.55 and e = 1.

A qualitative representation of the Ménétrey-Willam yield surface is reported in Fig. 3.3.

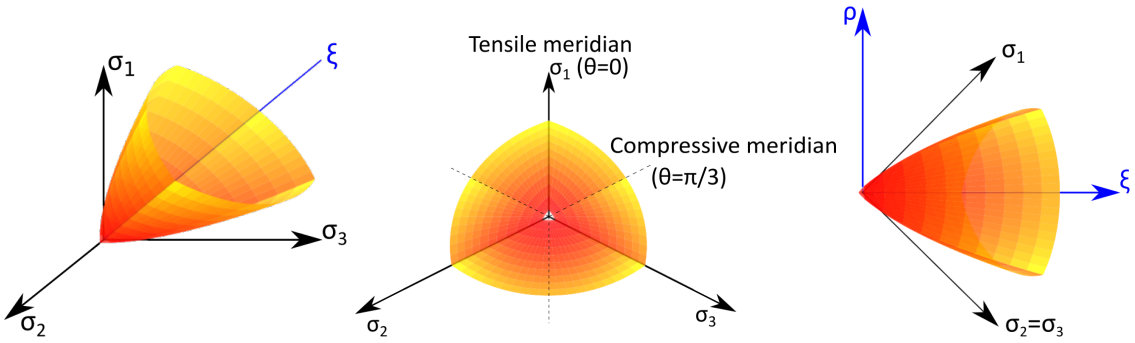

(a) (b) (c)

Figure 3.3: Qualitative representation of the Menétrey-Willam failure surface in the space of principal stresses (a); view in the deviatoric plane (b); view in the ρ-ξ plane (c).

3.1.2 The hardening/softening function

An isotropic hardening is considered in Eq. 3.2, through the functions $q_h(\kappa)$ and $q_s(\kappa)$, which are the hardening and softening laws, respectively. They are functions of the equivalent plastic strain κ, which is the internal variable that controls the plastic evolution, and is defined in the rate form as the absolute value of the volumetric component of the plastic strain tensor rate.

$$\dot{\kappa}(\boldsymbol{\varepsilon}^p) = |\mathrm{Tr}(\dot{\boldsymbol{\varepsilon}}^p)|. \tag{3.5}$$

Both functions control the parabolic shape and the size of the meridians of the yield surface (sections in the ρ-ξ plane), as shown in Fig. 3.4.

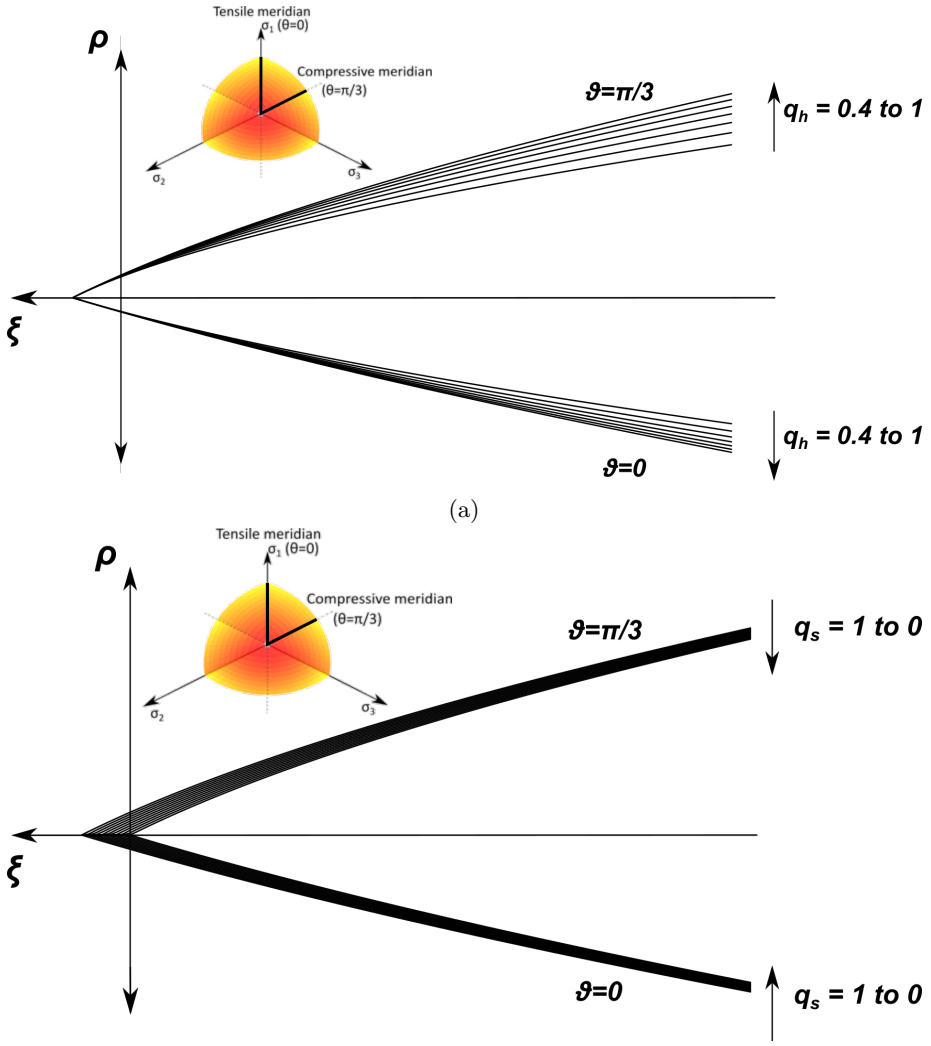

Figure 3.4: Evolution of the compressive meridians and tensile meridians of the yield surface in hardening (a), and softening (b).

In the present work, the hardening and softening functions are inspired from [190], and assume the following expressions

$$q_h(\kappa) = q_{h0} + (1 - q_{h0}) \sqrt{1 - \left(\frac{\kappa_{1D} - \kappa}{\kappa_{1D}} \right)^2}; \tag{3.6}$$

$$q_s(\kappa) = \left[1 + \left(\frac{n_1 - 1}{n_2 - 1}\right)^2\right]^{-2} \; ; \; n_1 = \frac{\kappa}{\kappa_{1D}}; \; n_2 = \frac{(\kappa_{1D} + t_s)}{\kappa_{1D}}. \tag{3.7}$$

Fig. 3.5 depicts a qualitative plot of the hardening and softening functions. It can be observed that the hardening function can increase from a minimum value q_{h0} that defines the onset of plasticity, to a maximum value of one, corresponding to a value of the equivalent plastic strain equal to κ_{1D}, that defines the onset of softening. From that point, the hardening function keeps a constant unitary value and the material enters into the softening regime controlled by the softening function. It can assume a maximum value of one (during the hardening process) and gradually decreases during the softening process.

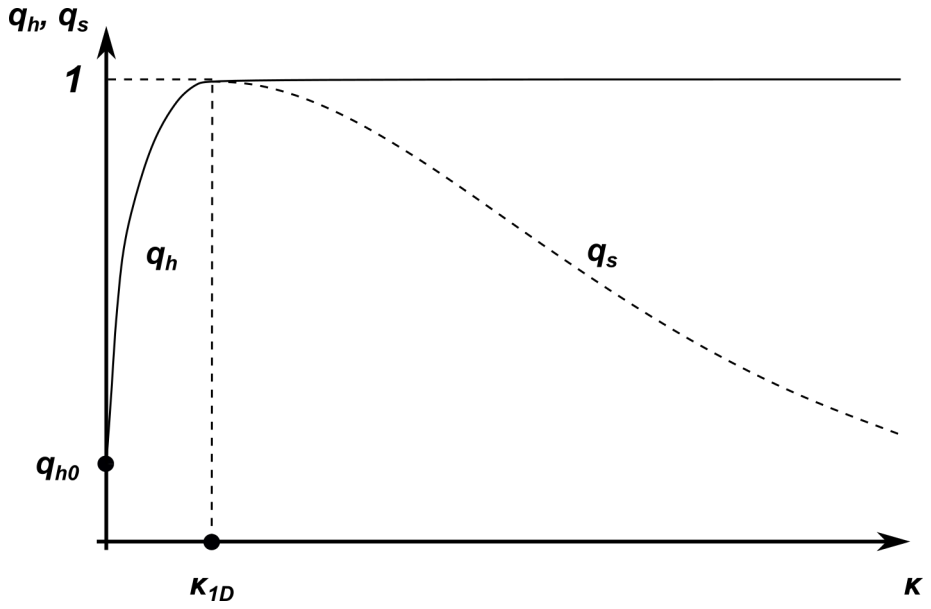

Figure 3.5: Qualitative plots of the hardening and softening functions.

3.1.3 The flow rule

A non-associated flow rule

$$\dot{\boldsymbol{\varepsilon}}^p = \dot{\gamma} \frac{\partial g_p}{\partial \boldsymbol{\sigma}} (\boldsymbol{\sigma}, \kappa) \tag{3.8}$$

is considered, where $\dot{\boldsymbol{\varepsilon}}^p$ is the rate of the plastic strain vector, and $\dot{\gamma} > 0$ is the plastic multiplier. The function g_p represents the plastic potential. The later has a quadratic form and takes the following expression in function of the HW coordinates [111]

$$g_p = -\frac{A}{f_c}\left(\frac{\rho}{\sqrt{q(\kappa)}}\right)^2 - B\left(\frac{\rho}{\sqrt{q(\kappa)}}\right) + \frac{\xi}{\sqrt{q(\kappa)}} = 0, \tag{3.9}$$

where A and B are experimentally determined coefficients. In Eq. 3.9, $q(\kappa)$ is the hardening/softening law, defined as $q(\kappa) = q_h(\kappa)q_s(\kappa)$.

The plastic potential has a circular shape in the deviatoric plane, which is different from that of the yield surface, as shown in Fig. 3.6.

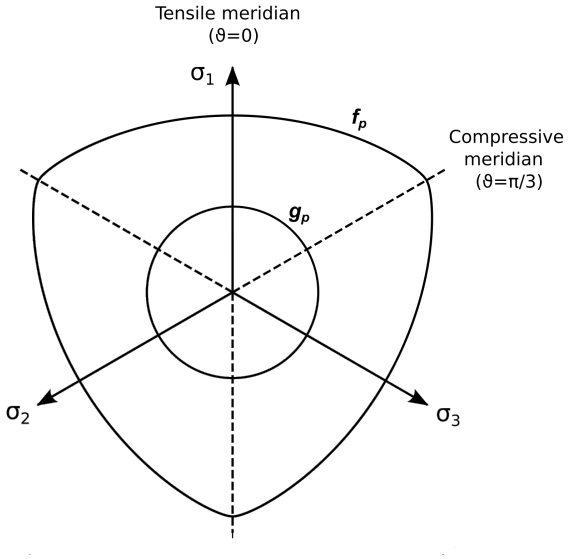

Figure 3.6: Qualitative plots of the yield surface and plastic potential in the deviatoric plane.

3.2 The damage formulation of the model

Damage in concrete is caused by the growth and coalescence of micro-cracks. In the framework of Continuum Damage Mechanics, the microscopic effects of damage is interpreted at the macro-scale by a degradation of the material stiffness. As shown by experimental data reported in Fig. 3.7 and Fig. 3.8, the stiffness degradation during tensile loading is less than in compressive loading.

Therefore, it is convenient to expect different damage mechanisms in tension and compression [114, 191].

Two different global damage variables are incorporated in this model. The first one, ω^*, is used in the formulation of the yield surface (Eq. 3.2) to control the reduction in size of the elastic domain as damage grows. The second one, denoted by ω, is used in the constitutive relationship to account for stiffness degradation effects due to damage. A partial recovery of ω is possible, to account for crack closure effects under stress reversals.

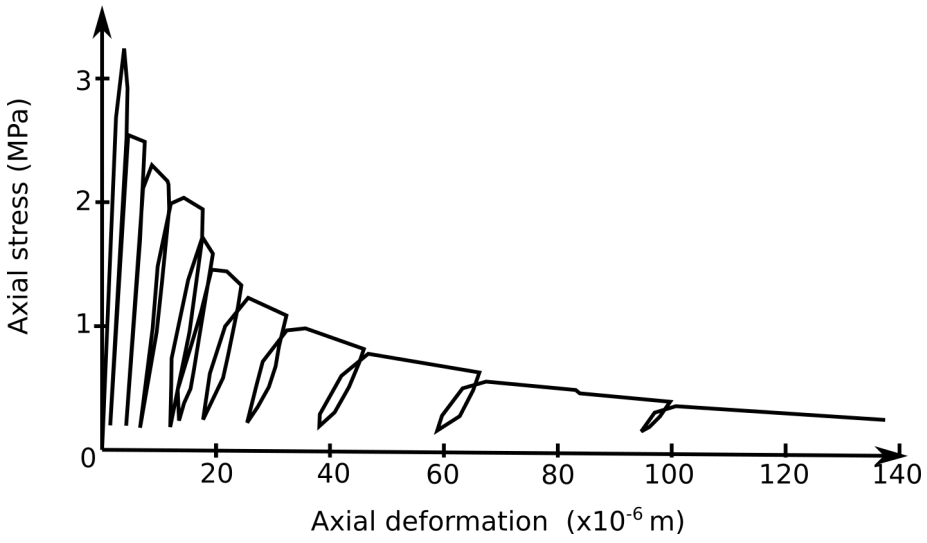

Figure 3.7: Concrete response to cyclic tensile loading from [118]

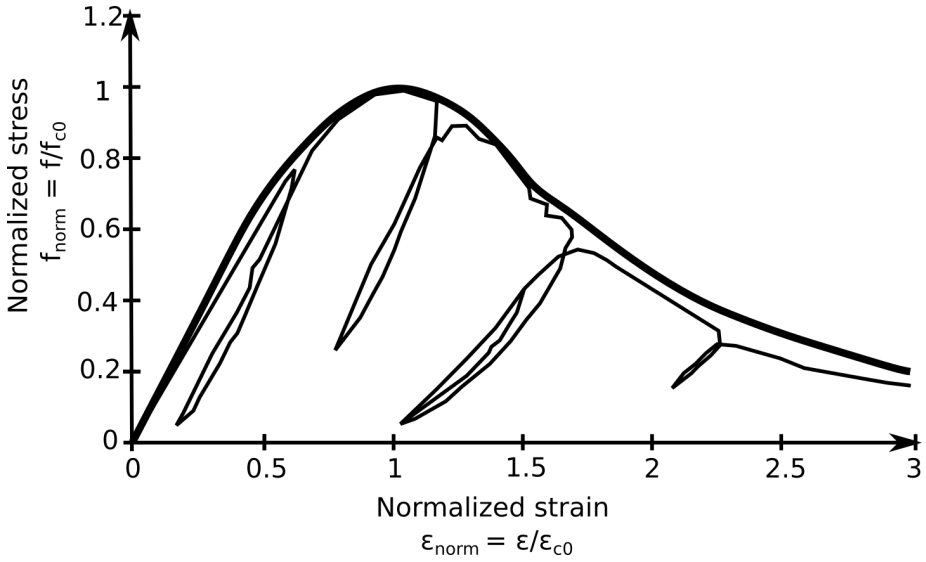

Figure 3.8: Concrete response to monotonic and cyclic compressive loading from [192].

3.2.1 The isotropic damage model

In order to account for different failure mechanisms in tension and compression, two damage components, one in compression ω_c, and one in tension ω_t, are defined as increasing functions of the equivalent plastic strains in compression and tension, respectively. They are based on the amount of extension that the material is experiencing during loading, and they assume a value equal to zero when the material is not damaged, or equal to unit when it is fully damaged.

The scalar damage components ω_c and ω_t are defined by using exponential functions, as suggested in [52]

$$\omega_c = \begin{cases} 0 & \text{if} \quad \kappa_c \leq \kappa_{c0} \\ 1 - (1 - A_c)\,\frac{\kappa_{c0}}{\kappa_c} - A_c \exp\left[-B_c\left(\kappa_c - \kappa_{c0}\right)\right] & \text{if} \quad \kappa_c > \kappa_{c0} \end{cases} \tag{3.10}$$

$$\omega_t = \begin{cases} 0 & \text{if} \quad \kappa_t \leq \kappa_{t0} \\ 1 - (1 - A_t)\,\frac{\kappa_{t0}}{\kappa_t} - A_t \exp\left[-B_t\left(\frac{\kappa_t - \kappa_{t0}}{\kappa_f - \kappa_{t0}}\right)\right] & \text{if} \quad \kappa_t > \kappa_{t0} \end{cases}, \tag{3.11}$$

where A_c, A_t, B_c and B_t are experimentally determined parameters in compression and tension. The internal variables κ_c and κ_t are used to describe the damage evolution in compression and tension, respectively. Their evolution laws are defined as

$$\begin{aligned} \dot{\kappa}_c &= \sum_{i=1}^{3} -\frac{\dot{\varepsilon}_i^p - |\dot{\varepsilon}_i^p|}{2} \\ \dot{\kappa}_t &= \sum_{i=1}^{3} \frac{|\dot{\varepsilon}_i^p| + \dot{\varepsilon}_i^p}{2}, \end{aligned} \tag{3.12}$$

where ε_i^p represents the eigenvalues of the plastic strain tensor. The quantities κ_{c0} and κ_{t0} are the initial values of κ_c and κ_t, respectively, at which damage starts. In order to reduce the mesh-dependency of the solution, the crack band formulation [193, 194] is used in the definition of κ_t through the crack-band equivalent plastic strain κ_f, which is defined as

$$\kappa_f = \frac{1}{2}\kappa_{t0} + \frac{G_f}{f_t \cdot l_c}, \tag{3.13}$$

where G_f is the fracture energy, and l_c is the element characteristic length. An acceptable estimate is $l_c = \sqrt[3]{V^e}$, where V^e is the volume of the finite element.

The total damage variable ω^* used for the definition of the yield surface in Eq. 3.2 is defined as a combination of the compressive and tensile damage components

$$\omega^* = 1 - \left[1 - \omega_c\left(\kappa_c\right)\right]\left[1 - \omega_t\left(\kappa_t\right)\right]. \tag{3.14}$$

3.2.2 Stiffness recovery under stress reversals

In order to account for the crack closure effect during the transition from tensile to compressive load, a stiffness recovery function is adopted to define a new damage variable ω. This stress dependent damage variable takes into account the increase of stiffness due to the closure of cracks when the mechanical loading changes from tension to compression [27, 195]. The stiffness recovery function is defined as

$$s\left(\boldsymbol{\sigma}^{e,tr}\right) = 1 - s_0\left(1 - \frac{\sum_{i=1}^{3}\left|\boldsymbol{\sigma}_i^{e,tr}\right| - \boldsymbol{\sigma}_i^{tr}}{2\sum_{i=1}^{3}\left|\boldsymbol{\sigma}_i^{e,tr}\right|}\right), \tag{3.15}$$

where s_0 is the maximum value of the stiffness recovery function, and $\boldsymbol{\sigma}_i^{e,tr}$ are the principal values of the elastic trial stress during the return mapping algorithm, as explained in Section 4.2.

The stress-dependent damage variable is a function of the stiffness recovery function s

$$\omega = 1 - \left[1 - \omega_c\left(\kappa_c\right)\right]\left[1 - s\left(\boldsymbol{\sigma}^{e,tr}\right)\omega_t\left(\kappa_t\right)\right]. \tag{3.16}$$

It is worth mentioning that, while the damage variable ω^* can only increase, the stress-dependent damage variable ω can decrease or increase, according to the sign of the stress variation.

In order to illustrate the crack closure effect, the constitutive response of the plasto-damage model to a reversal of the mechanical loading is shown in Figure 3.9. An axial tensile strain is imposed to the concrete sample (point 1 to 2), and then the strain is reversed, until the material undergoes full compression (Figure 3.9a). The constitutive response reported in Figure 3.9b shows that, when the mechanical loading changes from tension to compression (point 3), there is an increase in stiffness, due to the closure of cracks that opened during the tensile loading.

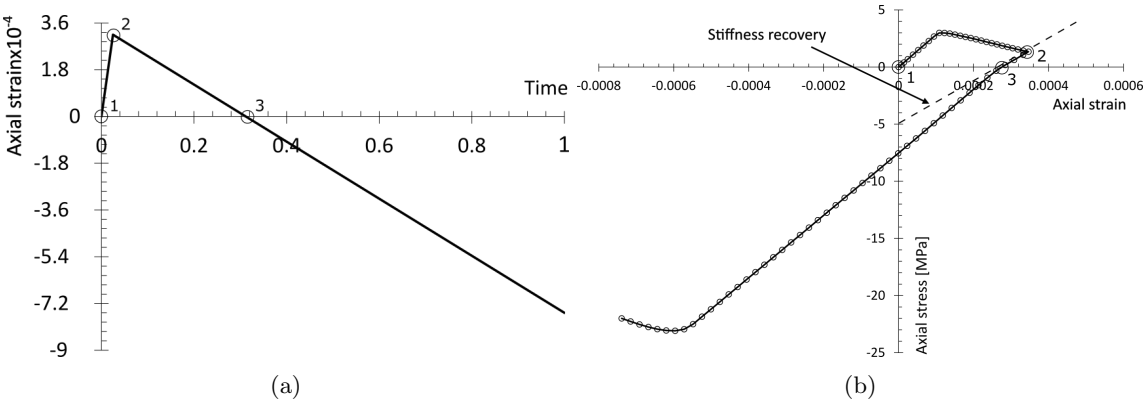

(a) (b)

Figure 3.9: Quasi-static imposed strain (a), and corresponding constitutive response with stiffness recovery (b).

A numerical test is performed to appreciate the capabilities of the plastic-damage model to reproduce the mechanical behaviour of concrete. To this aim, a quasi-static monotonic and cyclic imposed load, under strain control is considered. The loading patterns for monotonic and cyclic

loading are represented in Figure 3.10a and the comparison between the mechanical responses are shown in Figure 3.10b. Two main features of concrete behaviour can be observed from the constitutive response in Figure 3.10b. First, a characteristic closed loop is evidenced whose shape must depend on damage and stiffness recovery. Further, during the reloading phase (point 4 to 6), the constitutive curve does not return to the point where the unloading started (point 3), but it follows a different path (from point 4 to 6, through 5). Interestingly, the constitutive curve at reloading reaches the same softening curve that would be proper of the monotonic loading. These observations are coherent with experimental evidences.

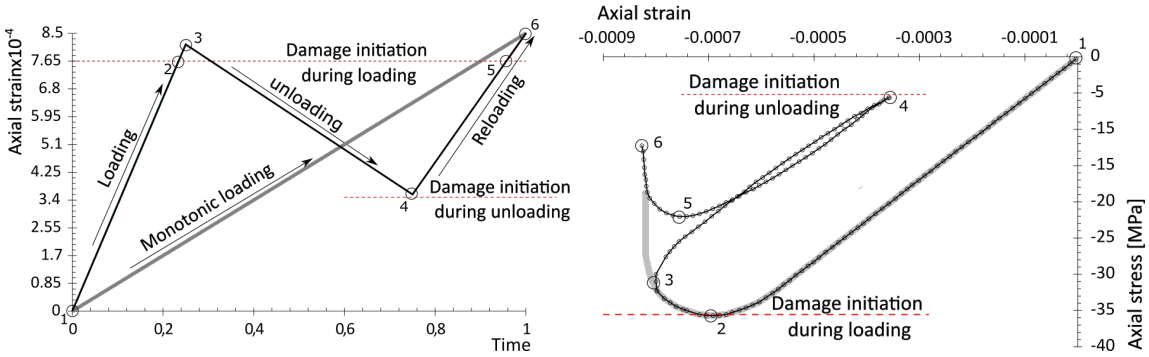

(a) (b)

Figure 3.10: Quasi-static monotonic and cyclic imposed strain (a), and constitutive response (b).

3.3 The creep model

Concrete creep is characterized by a gradual strain growth with time under a unit sustained stress. The creep behaviour of concrete is usually described by means of creep curves. These curves depict the vertical deformation of a concrete specimen subjected to a constant compressive load versus time. Creep curves of concrete are commonly subdivided into three stages [120], as shown in Fig. 3.11. A first stage, called primary creep or transitional creep, is characterized by a rapid increase in the creep strain, and a steady decrease in the creep rate. The second stage is called secondary creep, or steady-state creep, in which a constant creep rate is observed, and finally the last stage, called tertiary creep, which is characterized by a rapid increase of the creep rate and

subsequent failure. From experimental evidence [41], there exists a relationship between the creep behaviour and the loading level. When the loading level is lower than the linear creep threshold, which is approximately equal to 40% of concrete strength, the relationship between creep strain and stress is linear. Increasing the loading level between 40% to 70% of the concrete strength accounts for non-linear creep. For the aforementioned loading levels, the creep curve will not usually step into the tertiary stage. This stage is typically envisaged for loading levels above 70% of concrete strength [196].

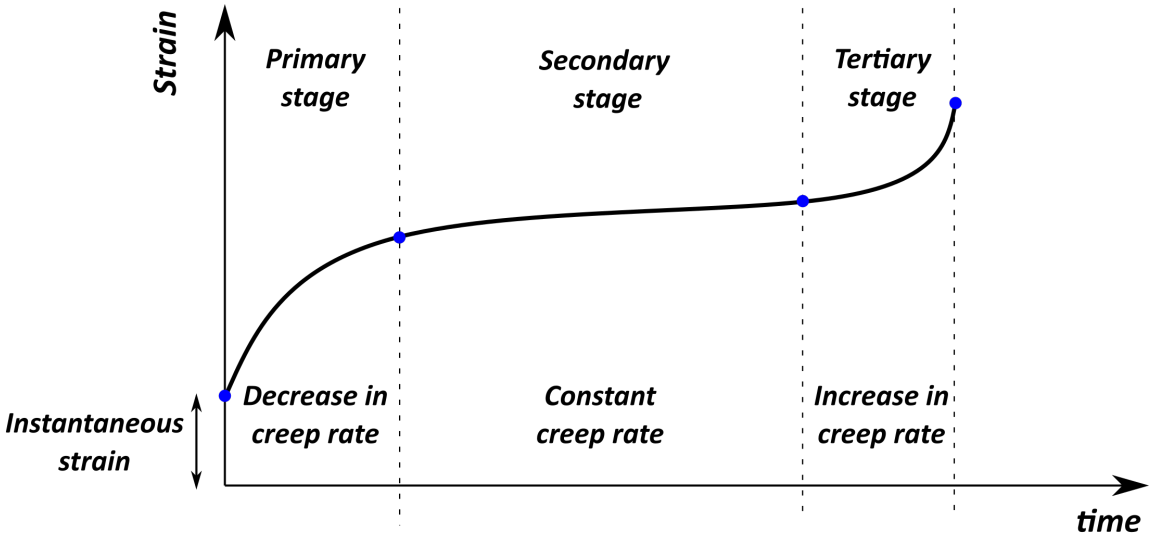

Figure 3.11: Typical three-stage pattern of concrete creep curves.

Various concrete creep models exist, including CEB-FIP model [74], ACI model [197], fib model [198], B3 model [53], and B4 model [199].

The creep model used herein is the B3 model. It is an aging linear visco-elastic model grounded on the solidification theory (Fig. 3.12). In line with this formulation, it is assumed that the aging is a consequence of volume growth of the load-bearing solidified matter (considered as the C-S-H for Calcium Silicate Hydrate), whose properties are non-aging, and are described by a Kelvin chain with age-independent moduli and viscosities. In this way aging can be better justified physically, and agrees well with test results [196].

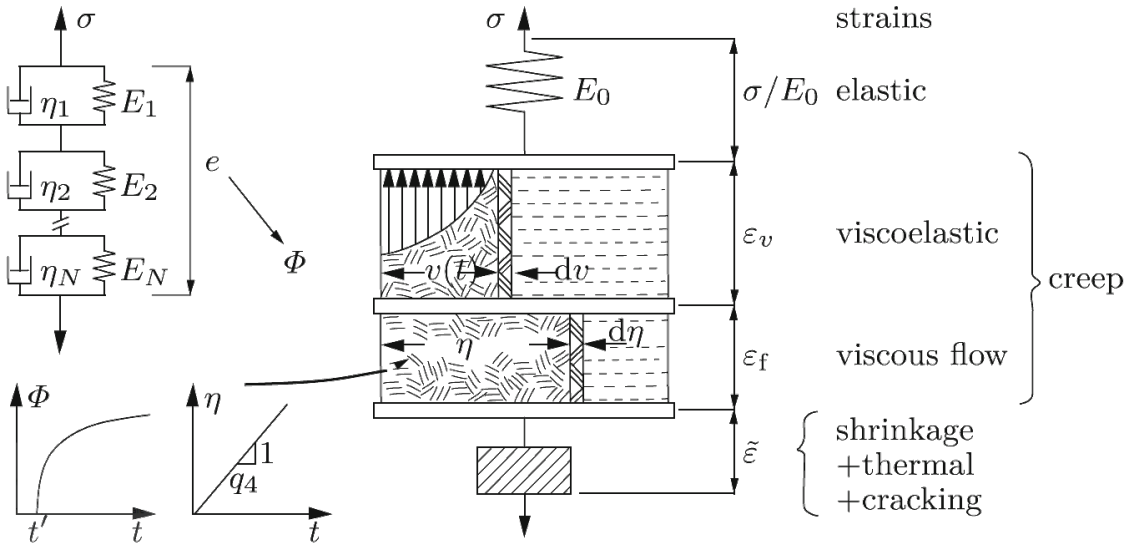

Figure 3.12: Solidification model for creep [196].

The compliance function of the B3 creep model is expressed in MPa^{-1} as

$$J(t,t') = q_1 + C_0(t,t') + C_d(t,t',t_0), \tag{3.17}$$

where q_1 is the instantaneous strain due to unit stress in MPa^{-1}, expressed as a function of the mean elastic modulus at 28 days $E_{cm,28}$ in Mpa as

$$q_1 = 0.6/E_{cm28}; \tag{3.18}$$

t and $t^{'}$ represent the current age and loading age in days, respectively.

$C_0(t,t')$ is the basic creep compliance function of the B3 model, expressed as [53]

$$C_0(t,t') = q_2 Q(t,t') + q_3 \ln[1+(t-t')^{0.1}] + q_4 \ln\left(\frac{t}{t'}\right), \tag{3.19}$$

The term $q_2 Q(t,t')$ represents the aging visco-elastic part of the compliance function. The parameter q_2 takes the following expression in MPa^{-1}

$$q_2 = 185.4 \times 10^{-6} c^{0.5} f_{cm28}^{-0.9}, \tag{3.20}$$

where c is the cement content in kg/m^3, and f_{cm} is the mean compressive strength of concrete at 28 days in MPa. $Q(t,t')$ is an approximate binomial integral and is expressed as

$$\begin{aligned} Q\left(t,t'\right) &= Q_f\left(t'\right)\left[1+\left(\frac{Q_f\left(t'\right)}{Z\left(t,t'\right)}\right)^{r\left(t'\right)}\right]^{-1/r\left(t'\right)} \\ Q_f\left(t'\right) &= \left[0.086\left(t'\right)^{2/9}+1.21\left(t'\right)^{4/9}\right]^{-1} \\ Z\left(t,t'\right) &= \left(t'\right)^{-0.5}\cdot \mathrm{In}\left[1+\left(t-t'\right)^{0.1}\right] \\ r\left(t'\right) &= 1.7\left(t'\right)^{0.12}+8. \end{aligned} \tag{3.21}$$

The second term of Eq. 3.19 includes a log-power function, and it represents the non-aging visco-elastic part; The parameter q_3 assumes the following expression in MPa^{-1}

$$q_3 = 0.29(w/c)^4 q_2, \tag{3.22}$$

where w/c is the water to cement ratio.

The third term of Eq. 3.19 accounts for the viscous flow part of the compliance function, where the parameter q_4 is expressed as the following in MPa^{-1}

$$q_4 = 20.3 \times 10^{-6}(a/c)^{-0.7}. \tag{3.23}$$

The term $C_d(t,t',t_0)$ represents the drying creep compliance function of the B3 model that takes into account the Pickett effect [200]. It occurs when there is an exchange of moisture between the concrete specimen and the environment, or when there is a non uniform distribution of moisture across the specimen. Therefore, it is a function of the spatial average of the pore relative humidity h, via the function $H(t)$

$$H(t) = 1-(1-h)\tanh\left[\left(\frac{t-t_0}{\tau_{sh}}\right)^{1/2}\right], \tag{3.24}$$

where τ_{sh} is the shrinkage half-time in days [201]. The drying creep takes the following expression

$$C_d(t,t',t_0) = q_5 \left[e^{-8H(t)} - e^{-8H(t_0{}')} \right]^{0.5}, \tag{3.25}$$

where t_0 is the time at which drying starts in days, and $t_0{}' = max(t', t_0)$. q_5 is the drying creep compliance parameter and is a function of the concrete mean strength at 28 days $f_{cm,28}$ in MPa, and the ultimate shrinkage strain $\varepsilon_{sh,\infty}$, and is given in MPa^{-1} as

$$q_5 = 0.757 {f_{cm28}}^{-1} \left| \varepsilon_{sh\infty} \times 10^6 \right|^{-0.6}. \tag{3.26}$$

3.4 Extension of the plastic damage model to include fatigue

The plastic-damage model described above does not allow for plastic flow or damage growth when the stress state lies below the yield surface. However, fatigue degradation and the corresponding accumulation of plastic strain is often observed experimentally, even for maximum stress levels smaller than the yielding point of the material. In order to allow for plastic strain and damage accumulation in such a situation, a modified formulation of the Ménétrey-Willam yield surface is proposed in this work. Specifically, the yield surface is extended to include a fatigue degradation function q_f, that must depends on a history variable which accumulates as the number of cycle increases. In this way, the fatigue degradation is interpreted as the reduction of the local strength of the material, as the number of cycles increases. Therefore, the new expression of the yield surface in the HW space is expressed as follows

$$f = 1.5 \left[\frac{\rho}{(1-\omega^*) f_c} \right]^2 + \frac{q_h(\kappa) m}{(1-\omega^*) f_c} \left[\frac{\rho}{\sqrt{6}} r(\theta, e) + \frac{\xi}{\sqrt{3}} \right] - q_h(\kappa) q_s(\kappa) q_f(\gamma_f) = 0, \tag{3.27}$$

where γ_f is the accumulated history variable for fatigue, which rate is always positive ($\dot{\gamma_f} \geq 0$).

Many choices are possible for the fatigue degradation function q_f. As a general rule, it must always be less than one, and decreases monotonically. The following power-logarithmic function

has been used as the fatigue degradation function

$$q_f(\gamma) := \begin{cases} 1 & \text{if} \quad \gamma < \gamma_t \\ (1 - a \log(\gamma/\gamma_t))^2 & \text{if} \quad \gamma_t \leq \gamma \leq 10^{1/a}\gamma_t \\ 0 & \text{if} \quad \gamma > 10^{1/a}\gamma_t \end{cases} \tag{3.28}$$

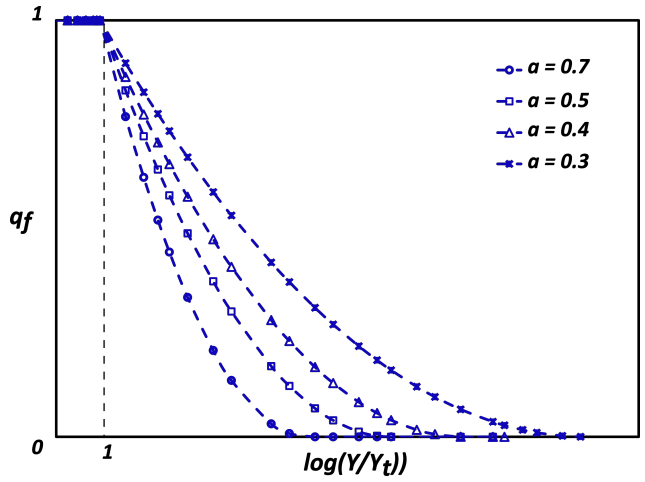

Figure 3.13: Qualitative representation of the fatigue degradation function.

From Fig. 3.13 that represents a qualitative plot of the fatigue degradation function, it is observed that the parameter γ_t is used to control the onset of fatigue degradation, and most importantly, the parameter a decides the fatigue degradation rate.

The particular choice of the function in Eq. 3.28 is motivated by the similarity between the 1-D expression of the yield surface (Eq. 3.27), in tension and compression, and the formulae for fatigue life curves.

In the uniaxial compressive case with $\sigma_c > 0$, the principal stresses are $\sigma_3 = -\sigma_c; \sigma_2 = \sigma_1 = 0$. The corresponding stress invariants and HW coordinates are evaluated according to Eq. 3.1, and results into

$$\xi = \frac{-\sigma_c}{\sqrt{3}}, \quad \rho = \sqrt{\frac{2}{3}}\sigma_c, \quad \theta = \pi/3. \tag{3.29}$$

The elliptic parameter r is then evaluated, $r(\theta, e) = r(\pi/3, e) = 1$, and substituted in the expression of the yield surface (Eq. 3.2) to obtain the following equation

$$\left[\frac{\sigma_c}{(1-\omega^*)\, f_c}\right]^2 - q_f(\gamma_f) q_h(\kappa) q_s(\kappa) = 0. \tag{3.30}$$

It finally results in

$$\sigma_c / f_{c,res} = 1 - a \log\left(\gamma_f / \gamma_t\right), \tag{3.31}$$

where, $f_{c,res} = q_h(\kappa) q_s(\kappa)\,(1-\omega^*)\, f_c$.

Similarly, in the uniaxial tensile case with $\sigma_t > 0$, the principal stresses are $\sigma_3 = \sigma_2 = 0; \sigma_1 = \sigma_t$. The corresponding stress invariants and HW coordinates are evaluated according to Eq. 3.1, and results into

$$\xi = \frac{\sigma_t}{\sqrt{3}}, \quad \rho = \sqrt{\frac{2}{3}}\sigma_t, \quad \theta = 0. \tag{3.32}$$

The elliptic parameter r is then evaluated, $r(\theta, e) = r(0, e) = 1/e$, and substituted in the expression of the yield surface (Eq. 3.2) to obtain the following equation

$$\left[\frac{\sigma_t}{(1-\omega^*)\, f_c}\right]^2 + \frac{q_h(\kappa) m}{(1-\omega^*)\, f_c}\sigma_t \left[\frac{1+e}{3\mathrm{e}}\right] - q_f(\gamma_f) q_h(\kappa) q_s(\kappa) = 0. \tag{3.33}$$

Assuming that $\frac{f_c^2 - f_t^2}{f_c f_t} \simeq \frac{f_c}{f_t}$, it finally results in

$$\sigma_t / f_{t,res} = \left(1 - a \log\left(\gamma_f / \gamma_t\right)\right), \tag{3.34}$$

where, $f_{t,res} = q_s(\kappa)\,(1-\omega^*)\, f_t$.

Eq. 3.31 and 3.34 and very similar to fatigue life curve formulae (see Eq. 2.1). As observed by Cornelissen et al. [202], no difference was found between tension and compression fatigue life curves, provided that the stresses were related to the static tensile and compressive strengths respectively. This is clear indication that, in both cases, the dynamic behaviour of concrete is determined by the same material properties, namely a and γ_t in the present case.

It is assumed that the fatigue degradation is driven by the amount of local extension experienced by the material, which are governed by the positive part of the elastic strain vector. The internal variable for fatigue degradation κ_f is defined such that

$$\dot{\kappa}_f = \frac{1}{2}\sum_{i=1}^{3}\left(\dot{\varepsilon}_i^e + |\dot{\varepsilon}_i^e|\right), \tag{3.35}$$

where ε_i^e represents the eigenvalues of the elastic strain tensor. Such a choice is motivated by the fact that, fatigue damage must accumulate, even for stress states below the yield surface. As a consequence, in the case of tensile load, the fatigue degradation is directly created by the extensions, in the same direction as the tensile load; However, in the case of compressive load, the extensions are transmitted by the Poisson's effect, and then, are perpendicular to the direction of load.

The accumulated history variable γ_f takes the following expression,

$$\gamma_f = \int_0^t H\left(\dot{\kappa}_f\right)|\dot{\kappa}_f|\, d\tau, \tag{3.36}$$

where $H\left(\dot{\kappa}_f\right)$ represents the Heaviside function, defined such that

$$H\left(\dot{\kappa}_f\right) := \begin{cases} 1, & \text{if} \quad \dot{\kappa}_f > 0 \quad \text{(loading)} \\ 0, & \text{if} \quad \dot{\kappa}_f \leq 0 \ \text{(unloading)} \end{cases}. \tag{3.37}$$

In this way, fatigue degradation accumulates only during the loading part of the cyclic loading, and not during unloading.

Similarly to the hardening and softening functions described above, The residual strength due to fatigue degradation along the tensile and compressive meridians of the yield surface are provided in Fig. 3.14.

Fig. 3.15 reports the residual strength due to fatigue degradation on the deviatoric section as the confinement level increases. It can be seen that, in the case of no confinement, the size of the deviatoric section reduces is a noticeable manner, as q_f increases, while in the cases of medium and high confinements, the reduction in size is less noticeable, especially in high confinement. As a

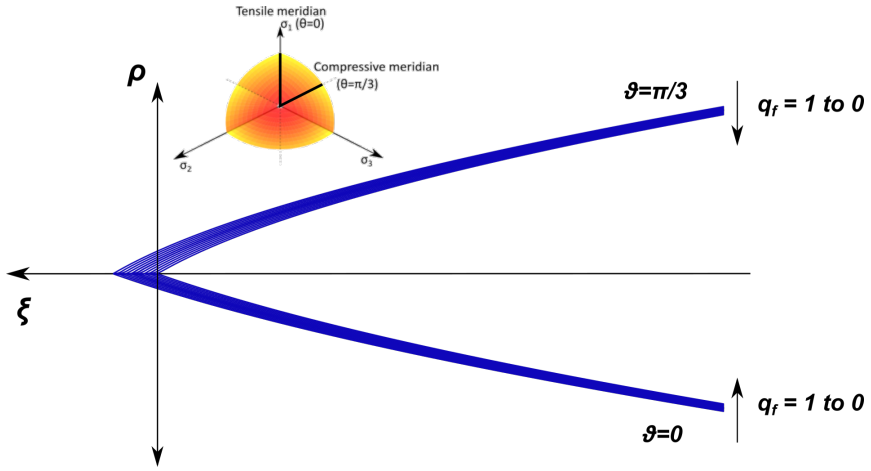

Figure 3.14: Evolution of the compressive and tensile meridians of the yield surface in fatigue.

consequence, the strength degradation due to fatigue is more relevant at lower confinement, while almost no strength degradation is noticed at higher confinement levels. This is consistent with the experimental fact that, fatigue life in compression increases with the level of confinement [86].

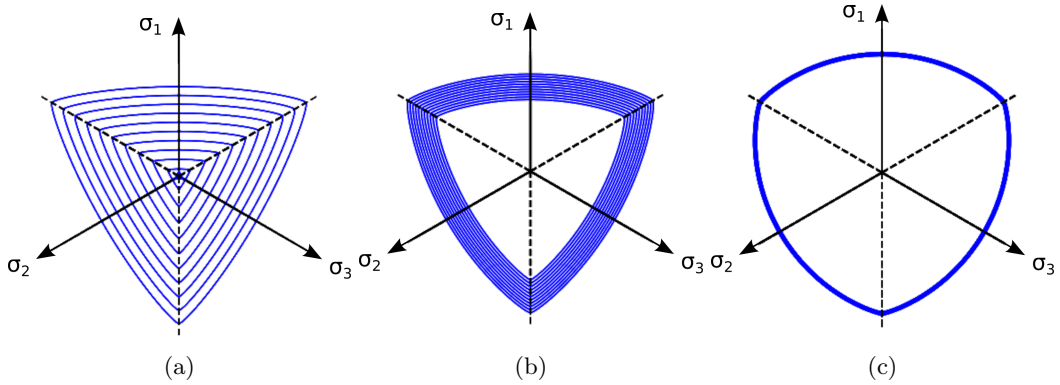

(a) (b) (c)

Figure 3.15: Evolution of the deviatoric section of the yield surface in fatigue (the section moves inwards as q_f increases): for no confinement(a), medium confinement (b), and high confinement (c).

Chapter 4

Numerical implementation

In the following chapter. the coupling scheme between the plastic damage and creep models is discussed. With reference to the coupling scheme, the total stress is split into two components in an additive manner: a plastic damage component and a creep component. A two-step algorithm, made of an elastic predictor step, plus a plastic correction step, is used to evaluate the first stress component, while the exponential algorithm serves for the calculation of the second component. The computation of the elasto-plastic damage consistent tangent operator, and of the visco-elasto-plastic constitutive tangent operator is discussed. A "return to apex" procedure is presented, in order to deal with situations in which the return-mapping vector does not intersect the yield surface during the return-mapping procedure.

4.1 Stress-strain relationship and coupling scheme

Let $\boldsymbol{\varepsilon}_{n+1}$ be the total strain at a generic time interval $[t_n,\, t_{n+1}]$. Small strains are assumed and the constitutive coupled model can be described by the following stress-strain relationship

$$\boldsymbol{\sigma}_{n+1} = (1-\omega_{n+1})\boldsymbol{D}^{ve}_{n+1/2}\left(\boldsymbol{\varepsilon}_{n+1} - \boldsymbol{\varepsilon}^{p}_{n+1} - \boldsymbol{\varepsilon}^{c}_{n+1}\right), \tag{4.1}$$

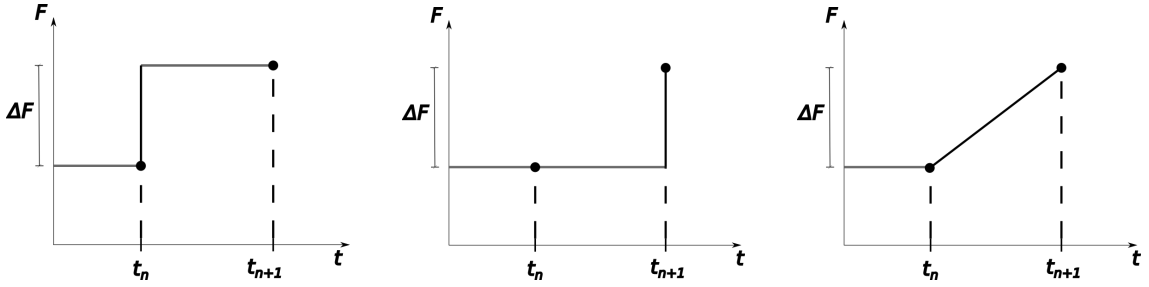

(a) load applied at t_n (b) load applied at t_{n+1} (c) linear variation

Figure 4.1: Different schemes for the plastic damage and creep coupling.

where $\boldsymbol{\sigma}_{n+1}$, $\boldsymbol{\varepsilon}^p_{n+1}$ and $\boldsymbol{\varepsilon}^c_{n+1}$ are the stress, plastic strain, and creep strain, respectively, at time t_{n+1}. In Eq. 4.1, ω_{n+1} represents the damage with stiffness recovery at the time t_{n+1}, as mentioned is Section 3.2.2; while $\boldsymbol{D}^{ve}_{n+1/2}$ is the elastic constitutive tensor computed by using the elastic modulus at mid-interval, as described in Section 4.4.

Three different schemes can be considered for the coupling between the plastic damage and creep models. During the loading interval from t_n to t_{n+1} the load increment can be applied instantaneously at the beginning of the time interval (Figure 4.1a); instantaneously at the end of the time interval (Figure 4.1b); or with a linear variation from the beginning to the end of the time interval (Figure 4.1c). While in the first two schemes the plastic damage and creep models evolve independently (specifically, in the first scheme the plastic damage model is activated before the creep model, while in the second scheme the creep model is activated before the plastic damage model), in the third scheme they evolve simultaneously.

Herein, the coupling between the plastic damage and creep models is done according to the first scheme, that is, the load increment is applied instantaneously at the beginning of the time interval $[t_n,\ t_{n+1}]$. Due to the presence of the viscous dashpots in the creep rheological model, that delay the response of the Kelvin moduli (see Section 4.4), the creep component of Eq. 4.1 is constant. Therefore, at the beginning of the time interval, the total stress is equal to the elastic trial stress $\boldsymbol{\sigma}^{e,tr}_{n+1}$, eventually corrected by the plastic corrector algorithm as described in Section 4.2. Once the instantaneous elasto-plastic damage stress $\boldsymbol{\sigma}^{ep}_{n+1}$ is obtained at the beginning of the time interval, the creep model is activated and the material undergoes a stress relaxation at constant

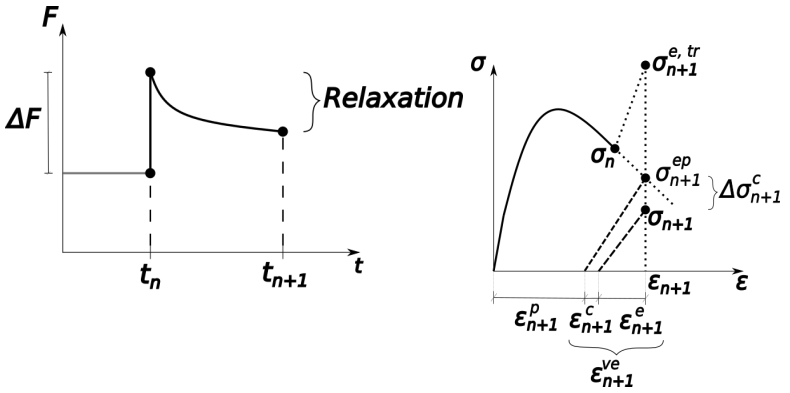

(a) (b)

Figure 4.2: Coupling scheme between plastic damage and creep models in the force versus time domain (a), and stress versus strain domain (b).

strain, corresponding to $\Delta\boldsymbol{\sigma}^c_{n+1}$, from time t_n to time t_{n+1}. The coupling mechanism between the plasto-damage and creep models is graphically described in Figure 4.2a in the force versus time domain. The same is reported in the stress versus strain uniaxial domain in Figure 4.2b, where the plastic strain $\boldsymbol{\varepsilon}^p_{n+1}$ and visco-elastic strain $\boldsymbol{\varepsilon}^{ve}_{n+1}$ are identified.

With reference to the coupling scheme described above, the constitutive equation (Eq. 4.1) can be split into an elasto-pastic damage part $\boldsymbol{\sigma}^{ep}_{n+1}$ and a creep relaxation part $\Delta\boldsymbol{\sigma}^c_{n+1}$ as follows

$$\begin{aligned}
\boldsymbol{\sigma}_{n+1} &= (1-\omega_{n+1})\boldsymbol{D}^{ve}_{n+1/2}\left(\varepsilon_{n+1}-\boldsymbol{\varepsilon}^p_{n+1}-\boldsymbol{\varepsilon}^c_{n+1}\right)\\
&= (1-\omega_{n+1})\boldsymbol{D}^{ve}_{n+1/2}\left(\varepsilon_{n+1}-\boldsymbol{\varepsilon}^p_{n+1}-\boldsymbol{\varepsilon}^c_{n}-\Delta\boldsymbol{\varepsilon}^c_{n+1}\right)\\
&= \underbrace{(1-\omega_{n+1})\boldsymbol{D}^{ve}_{n+1/2}\left(\varepsilon_{n+1}-\boldsymbol{\varepsilon}^p_{n+1}-\boldsymbol{\varepsilon}^c_{n}\right)}\underbrace{-(1-\omega_{n+1})\boldsymbol{D}^{ve}_{n+1/2}\Delta\boldsymbol{\varepsilon}^c_{n+1}}\\
&= \qquad\qquad \boldsymbol{\sigma}^{ep}_{n+1} \qquad\qquad + \qquad\qquad \Delta\boldsymbol{\sigma}^c_{n+1}.
\end{aligned} \tag{4.2}$$

4.2 Computation of the elasto-plastic damage stress

Let us denote by ${}^{(i+1)}\mathbf{x}$ the set of unknown variables of the elasto-plastic damage problem at the $(i+1)^{th}$ iteration and time t_{n+1}

$$ {}^{(i+1)}\mathbf{X} = \left[{}^{(i+1)}\boldsymbol{\sigma}^{ep}_{n+1}, {}^{(i+1)}\kappa_{n+1}, {}^{(i+1)}\dot{\gamma}_{n+1}, {}^{(i+1)}\kappa_{c,n+1}, {}^{(i+1)}\kappa_{t,n+1}, {}^{(i+1)}\kappa_{f,n+1} \right]^T \tag{4.3} $$

corresponding to a total of 11 scalar unknowns. Their evolution laws are reported here below

$$ \begin{aligned} \dot{\boldsymbol{\sigma}}^{\mathrm{ep}} &= (1-\omega)\boldsymbol{D}^{\mathrm{ve}}\,\dot{\boldsymbol{\varepsilon}}^{p} = \dot{\lambda}(1-\omega)\boldsymbol{D}^{\mathrm{ve}}\,\frac{\partial g}{\partial \boldsymbol{\sigma}} \\ \dot{\kappa} &= |\mathrm{Tr}\,(\dot{\boldsymbol{\varepsilon}}^{p})| = \dot{\lambda}|\mathrm{Tr}\left(\frac{\partial g}{\partial \boldsymbol{\sigma}}\right)| \\ \dot{\kappa}_c &= \frac{1}{2}\sum_{i=1}^{3}\left(|\dot{\boldsymbol{\varepsilon}}^{p}{}_i| - \dot{\boldsymbol{\varepsilon}}^{p}{}_i\right) = \dot{\lambda}\frac{1}{2}\sum_{i=1}^{3}\left(\left|\frac{\partial g}{\partial \boldsymbol{\sigma}_i}\right| - \frac{\partial g}{\partial \boldsymbol{\sigma}_i}\right) \\ \dot{\kappa}_t &= \frac{1}{2}\sum_{i=1}^{3}\left(\dot{\boldsymbol{\varepsilon}}^{p}{}_i + |\dot{\boldsymbol{\varepsilon}}^{p}{}_i|\right) = \dot{\lambda}\frac{1}{2}\sum_{i=1}^{3}\left(\frac{\partial g}{\partial \boldsymbol{\sigma}_i} + \left|\frac{\partial g}{\partial \boldsymbol{\sigma}_i}\right|\right) \\ \dot{\kappa}_f &= \frac{1}{2}\sum_{i=1}^{3}\left(\dot{\boldsymbol{\varepsilon}}^{e}{}_i + |\dot{\boldsymbol{\varepsilon}}^{e}{}_i|\right). \end{aligned} \tag{4.4} $$

The nature of the elasto-plastic damage problem motivates the use of a two-step algorithm, with an iterative procedure for the numerical implementation. The iterative procedure is described as follows.

At the first step, called the elastic trial step, it is assumed that the plastic multiplier is null. Therefore, at a generic time interval $[t_n, t_{n+1}]$, the strain increment $\Delta\boldsymbol{\varepsilon}_{n+1}$ is fully elastic and neither plastic flow nor damage occur. The elastic trial strain and stress, and the internal variable for plasticity and damage are given by

$$ \begin{aligned} \boldsymbol{\varepsilon}^{e,tr}_{n+1} &= \boldsymbol{\varepsilon}^{e}_{n} + \Delta\boldsymbol{\varepsilon}_{n+1} \\ \boldsymbol{\sigma}^{e,tr}_{n+1} &= (1-\omega_{n+1})\,\boldsymbol{D}^{ve}_{n+1/2}\boldsymbol{\varepsilon}^{e,tr}_{n+1} \\ \kappa^{tr}_{n+1} &= \kappa_n \\ \kappa^{tr}_{c,n+1} &= \kappa_{c,n} \\ \kappa^{tr}_{t,n+1} &= \kappa_{t,n}. \end{aligned} \tag{4.5} $$

However, the internal variable for fatigue $\kappa^{tr}_{f,n+1}$ is updated according to the trial elastic strain $\boldsymbol{\varepsilon}^{e,tr}_{n+1}$ as follows

$$\kappa_{f,n+1}^{tr} = \kappa_{f,n} + \dot{\kappa_f}(\boldsymbol{\varepsilon}_{n+1}^{e,tr}), \tag{4.6}$$

where $\dot{\kappa}_f(\boldsymbol{\varepsilon}_{n+1}^{e,tr})$ is evaluated from the last equation in 4.4.

Then, the plastic admissibility of the elastic trial is checked. This means, checking if the trial solution lies below the yield surface (admissible plastic state), or outside the yield surface (inadmissible plastic state).

If the plastic state of the trial solution is admissible, then the solution at step $n+1$ is given by the trial solution, and the set of unknowns is updated

$$\begin{aligned} \mathbf{X}_{n+1} &= \mathbf{X}^{tr}, \\ \mathbf{X}^{tr} &= \left[\boldsymbol{\sigma}_{n+1}^{e,tr}, \kappa_n, \dot{\gamma}_n, \kappa_{c,n}, \kappa_{t,n}, \kappa_{f,n+1}^{tr}\right]^T \end{aligned} \tag{4.7}$$

Otherwise, the inadmissible stress state must be brought back to the new boundary of the yield domain. This is achieved numerically using the return mapping algorithm or plastic correction. In this step, the set of non-linear algebraic equations (4.8) is solved under the constraint $\dot{\gamma}_{n+1} > 0$

$$\boldsymbol{B} = \begin{bmatrix} f_p\left(\boldsymbol{\sigma}, \kappa, \kappa_c, \kappa_t\right) \\ \boldsymbol{r}\left(\boldsymbol{\sigma}, \dot{\gamma}, \kappa_c, \kappa_t\right) \\ h(\boldsymbol{\sigma}, \dot{\gamma}, \kappa) \\ s_1\left(\dot{\gamma}, \kappa_c\right) \\ s_2\left(\dot{\gamma}, \kappa_t\right) \\ s_3\left(\dot{\gamma}, \kappa_f\right) \end{bmatrix} = \begin{bmatrix} f_p\left(\boldsymbol{\sigma}_{n+1}^{ep}, \kappa_{n+1}, \kappa_{c,n+1}, \kappa_{t,n+1}, \kappa_{f,n+1}\right) \\ \boldsymbol{\sigma}_{n+1}^{ep} - \boldsymbol{\sigma}_{n+1}^{e,tr} + (1-\omega_{n+1})\,\boldsymbol{D}_{n+1/2}^{ve}\Delta\varepsilon_{n+1}^{p} \\ \kappa_{n+1} - \kappa^{tr} - \dot{\kappa} \\ \kappa_{c,n+1} - \kappa_c^{tr} - \dot{\kappa}_c \\ \kappa_{t,n+1} - \kappa_t^{tr} - \dot{\kappa}_t \\ \kappa_{f,n+1} - \kappa_f^{tr} - \dot{\kappa}_f \end{bmatrix} = \mathbf{0} \tag{4.8}$$

The system of non-linear equations is solved by using the Newton-Raphson iterative procedure, in which the Jacobian matrix $\boldsymbol{A}$ of the set of equations (4.8) is inverted, and a new trial set of solutions is computed until the norm of the residual $\boldsymbol{r}$ (second equation of the set of equations 4.8) is less than a given tolerance.

$$\boldsymbol{A} = \begin{bmatrix} \frac{\partial f_p}{\partial \boldsymbol{\sigma}} & \frac{\partial f_p}{\partial \kappa} & \frac{\partial f_p}{\partial \dot{\gamma}} & \frac{\partial f_p}{\partial \kappa_c} & \frac{\partial f_p}{\partial \kappa_t} & \frac{\partial f_p}{\partial \kappa_f} \\ \frac{\partial \mathbf{r}}{\partial \boldsymbol{\sigma}} & \frac{\partial \mathbf{r}}{\partial \kappa} & \frac{\partial \mathbf{r}}{\partial \dot{\gamma}} & \frac{\partial \mathbf{r}}{\partial \kappa_c} & \frac{\partial \mathbf{r}}{\partial \kappa_t} & \frac{\partial \mathbf{r}}{\partial \kappa_f} \\ \frac{\partial h}{\partial \boldsymbol{\sigma}} & \frac{\partial h}{\partial \kappa} & \frac{\partial h}{\partial \dot{\gamma}} & \frac{\partial h}{\partial \kappa_c} & \frac{\partial h}{\partial \kappa_t} & \frac{\partial h}{\partial \kappa_f} \\ \frac{\partial s_1}{\partial \boldsymbol{\sigma}} & \frac{\partial s_1}{\partial \kappa} & \frac{\partial s_1}{\partial \dot{\gamma}} & \frac{\partial s_1}{\partial \kappa_c} & \frac{\partial s_1}{\partial \kappa_t} & \frac{\partial s_1}{\partial \kappa_f} \\ \frac{\partial s_2}{\partial \boldsymbol{\sigma}} & \frac{\partial s_2}{\partial \kappa} & \frac{\partial s_2}{\partial \dot{\gamma}} & \frac{\partial s_2}{\partial \kappa_c} & \frac{\partial s_2}{\partial \kappa_t} & \frac{\partial s_2}{\partial \kappa_f} \\ \frac{\partial s_3}{\partial \boldsymbol{\sigma}} & \frac{\partial s_3}{\partial \kappa} & \frac{\partial s_3}{\partial \dot{\gamma}} & \frac{\partial s_3}{\partial \kappa_c} & \frac{\partial s_3}{\partial \kappa_t} & \frac{\partial s_3}{\partial \kappa_f} \end{bmatrix}. \tag{4.9}$$

The incremental solution ${}^{(i+1)}\Delta\mathbf{X}$, and the solution ${}^{(i+1)}\mathbf{X}$ at the $(i+1)^{th}$ iteration, are given by

$$\begin{aligned} {}^{(i+1)}\Delta\mathbf{X} &= -{}^{i}\left(\boldsymbol{A}^{-1}\boldsymbol{B}\right) \\ {}^{(i+1)}\mathbf{X} &= {}^{i}\mathbf{X} + {}^{(i+1)}\Delta\mathbf{X}. \end{aligned} \tag{4.10}$$

During the Newton-Raphson iteration scheme from Eq. 4.10, it can be seen that the inadmissible stress state from the trial solution ${}^{i}\mathbf{X}$ is modified at the current iteration by an amount of ${}^{(i+1)}\Delta\mathbf{X}$ due to the plastic correction. The correction is done until the inadmissible stress state returns back to the new boundary of the yield surface at the current step.

4.3 The elasto-plastic damage consistent tangent operator

In order to reach the parabolic convergence of the Newton-Raphson method, it is convenient to define a tangent modulus which is consistent with the adopted integration scheme [203]. The consistent tangent modulus at step $n+1$ for the elasto-plastic damage model can be evaluated as [204]

$$\boldsymbol{D}^{ep}_{n+1} = \frac{d\boldsymbol{\sigma}^{ep}_{n+1}}{d\boldsymbol{\varepsilon}^{e,tr}_{n+1}}. \tag{4.11}$$

Its numerical expression is obtained by differentiation and linearization of the system of return-mapping equations, leading to the following set of equations

$$\begin{bmatrix} d\boldsymbol{\sigma}^{ep}_{n+1} \\ \Delta k \\ \Delta\dot{\gamma} \\ \Delta\kappa_c \\ \Delta\kappa_t \\ \Delta\kappa_f \end{bmatrix} = \begin{bmatrix} \boldsymbol{C}_{11} & \boldsymbol{C}_{12} & \boldsymbol{C}_{13} & \boldsymbol{C}_{14} & \boldsymbol{C}_{15} & \boldsymbol{C}_{16} \\ C_{21} & \boldsymbol{C}_{22} & C_{23} & C_{24} & C_{25} & C_{26} \\ C_{31} & \boldsymbol{C}_{32} & C_{33} & C_{34} & C_{35} & C_{36} \\ C_{41} & \boldsymbol{C}_{42} & C_{43} & C_{44} & C_{45} & C_{46} \\ C_{51} & \boldsymbol{C}_{52} & C_{53} & C_{54} & C_{55} & C_{56} \\ C_{61} & \boldsymbol{C}_{62} & C_{63} & C_{64} & C_{65} & C_{66} \end{bmatrix} \cdot \begin{bmatrix} 0 \\ (1-\omega_{n+1})\,\boldsymbol{D}^{ve}_{n+1/2} d\boldsymbol{\varepsilon}^{e,tr}_{n+1} \\ 0 \\ 0 \\ 0 \\ 0 \end{bmatrix} \tag{4.12}$$

where $\varepsilon^{e,tr}_{n+1} = \boldsymbol{\varepsilon}_{n+1} - \boldsymbol{\varepsilon}^{p}_{n} - \boldsymbol{\varepsilon}^{c}_{n}$ is the trial elastic strain, and $\boldsymbol{C}$ is the inverse of the Jacobian matrix $\boldsymbol{A}$. The consistent elasto-plastic tangent operator is then, computed as

$$\boldsymbol{D}^{ep}_{n+1} = \frac{d\boldsymbol{\sigma}^{ep}_{n+1}}{d\boldsymbol{\varepsilon}^{e,tr}_{n+1}} = (1-\omega_{n+1})\,\boldsymbol{C}_{12}\boldsymbol{D}^{ve}_{n+1/2}. \tag{4.13}$$

4.4 Computation of the stress relaxation due to creep

The stress relaxation $\Delta\boldsymbol{\sigma}^{c}_{n+1}$ is computed by using the B3 compliance function reported in Eq. 3.17, which can be modelled with any desired accuracy by a Kelvin chain rheological model, as shown in Figure 4.3. The Kelvin chain consists of a series of Kelvin units $\mu = 1, 2, 3, \ldots, N$, each of which is made of a spring of stiffness $E_\mu(t)$ coupled in parallel with a dashpot of viscosity $\eta_\mu(t) = \tau_\mu E_\mu(t)$, where τ_μ are the retardation times that must be adequately chosen.

The springs' moduli are obtained by a discretization of the continuous retardation spectrum, which can be uniquely defined by means of the Laplace transformation inversion, by using Widder's

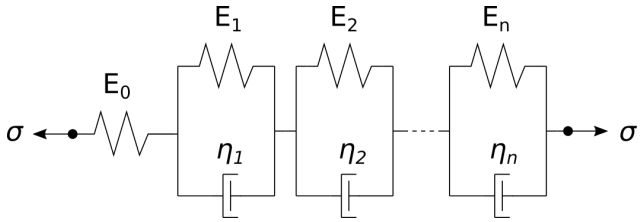

Figure 4.3: Kelvin chain rheological model.

approximate inversion formula [205]

$$L(\tau_\mu) = -\frac{\lim_{k\to\infty}(-k\tau_\mu)^k C^k(k\tau_\mu)}{(k-1)!}, \tag{4.14}$$

where C^k is the derivative of order k of the creep part of the compliance function

$$C(t,t') = J(t,t') - q_1. \tag{4.15}$$

In practice, there is no need to compute the above limit and $k = 3$ is sufficient for a good accuracy [205]. A qualitative representation of the continuous retardation spectra for the basic and drying creep is reported in Figure 4.4, in function of the logarithm of the age at loading t' and the retardation time τ_μ.

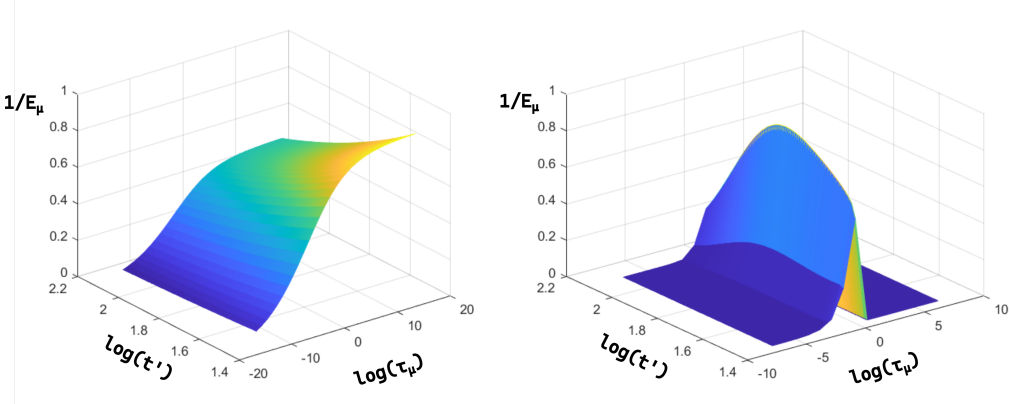

Figure 4.4: Qualitative representation of the continuous retardation spectra for basic creep (left), and drying creep (right).

The retardation times $\tau_\mu, \mu = 1, 2, 3, \ldots, N$, are usually selected so that they are equally spaced in the logarithmic scale. Further, the smallest retardation time τ_1 must be small enough to account for any instantaneous deformation, and the biggest retardation time must cover at least the observation time of interest. After the appropriate selection of the retardation times, the discrete retardation spectrum $A(\tau_\mu)$ can be obtained from the continuous one via the following equation

$$\frac{1}{E(\tau_\mu)} = A(\tau_\mu) = L(\tau_\mu)\ln(10)\Delta(\log(\tau_\mu)). \tag{4.16}$$

If the time step is short enough, the aging of the material can be neglected within the time step. Therefore, a constant creep function $C(t, t_{n+1/2})$ can be used to obtain a constant discrete spectrum for each time step, where $t_{n+1/2}$ is the age of concrete at the middle of the time step.

Commonly used algorithms for the numerical solution of the first order ordinary differential equation governing the Kelvin chain model, like the central or backward difference methods, or the Runge-Kutta method, will have numerical instability problems, as these algorithms are conditionally stable. For its unconditional stability, the exponential algorithm can be used to overcome this issue.

The steps for the numerical implementation of a visco-elastic creep model by means of the exponential algorithm are listed here below.

1. At t_0 set all components of internal variables $\boldsymbol{\lambda}(\tau_\mu) = \mathbf{0}, \mu = 1, 2, 3, \ldots, N$, where $\boldsymbol{\lambda}$ has the physical meaning of a dimensionless strain rate [196]; set $E_0 = 1/J(t_0, t_0)$; set the step counter n to 1.

2. For a given time interval $[t_n, t_{n+1}]$, compute the creep function from the compliance function calculated at mid-step

$$C(t, t_{n+1/2}) = J(t, t_{n+1/2}) - 1/E_{0,n+1/2}, \tag{4.17}$$

   where $t_{n+1/2} = (t_{n+1} + t_n)/2$, and $E_{0,n+1/2}$ is the elastic stiffness of concrete at mid-step.

3. For $k = 3$ compute the continuous spectrum of the creep function via Eq. 4.14.

4. After an adequate choice of retardation times, compute the discrete retardation spectrum $A(\tau_\mu)_{n+1/2}$ from Eq. 4.16.

5. Compute $\beta(\tau_\mu)$ and $\tilde{\lambda}(\tau_\mu)$ as

$$\beta(\tau_\mu) = e^{-\Delta t/\tau_\mu} \tag{4.18}$$

$$\tilde{\lambda}(\tau_\mu) = \tau_\mu(1-\beta(\tau_\mu))/\Delta t. \tag{4.19}$$

6. Compute $D(\tau_\mu)_{n+1/2} = 1/\left(A(\tau_\mu)_{n+1/2}[1-\tilde{\lambda}(\tau_\mu)]\right)$.

7. Compute the incremental modulus

$$E^{ve}_{n+1/2} = \left(\frac{1}{E_{0,n+1/2}} + \sum_{\mu=1}^{N} \frac{1}{D(\tau_\mu)_{n+1/2}}\right)^{-1}. \tag{4.20}$$

8. Compute the strain increment due to creep

$$\Delta\boldsymbol{\varepsilon}^c_{n+1} = \sum_{\mu=1}^{N} (1-\beta(\tau_\mu))\,\boldsymbol{\lambda}(\tau_\mu)_n. \tag{4.21}$$

9. For a given strain increment $\Delta\boldsymbol{\varepsilon}_{n+1}$, compute the corresponding creep stress increment

$$\Delta\boldsymbol{\sigma}^c_{n+1} = (1-\omega_{n+1})\boldsymbol{D}^{ve}_{n+1/2}(\Delta\boldsymbol{\varepsilon}_{n+1} - \Delta\boldsymbol{\varepsilon}^c_{n+1}), \tag{4.22}$$

where $\boldsymbol{D}^{ve}_{n+1/2}$ is the visco-elastic stiffness tensor computed using the incremental modulus $E^{ve}_{n+1/2}$, and ω_{n+1} is the damage variable that accounts for stiffness recovery.

10. Update the internal variables using the following formula

$$\boldsymbol{\lambda}(\tau_\mu)_{n+1} = \tilde{\lambda}(\tau_\mu)A(\tau_\mu)_{n+1/2}\boldsymbol{Z}\Delta\boldsymbol{\sigma}^c_{n+1} + \beta(\tau_\mu)\boldsymbol{\lambda}(\tau_\mu)_n, \tag{4.23}$$

where $\boldsymbol{Z}$ is the inverse of the unit elastic constitutive tensor.

Recalling Eq. 3.19, the basic creep is described by a log-power law with aging incorporated

through the solidification theory. It also considers an additional logarithmic term that reflects viscous flow, and that can be described by a dashpot with age-dependent viscosity. This term can be treated directly in the rate form, without the need to construct a Dirichlet series approximating its compliance function. The aging component of the basic creep is defined in a tabular form [201]. Considering its derivatives up to at least the third order can be tedious. However, a simpler exponential algorithm exists for basic creep [205], which requires only the definition of the spectrum of the non-aging log-power component. The aging component can be easily incorporated through the solidification theory [206] for which the visco-elastic strain rate is given by

$$\dot{\varepsilon}^c(t) = \left(q_2 \sqrt{\frac{1}{t}} + q_3 \right) \dot{\varepsilon}^c_{log-power}(t), \tag{4.24}$$

where $\dot{\varepsilon}^c_{log-power}(t)$ represents the visco-elastic strain rate due to the log-power term of the basic creep. Therefore, the foregoing algorithm can be modified in the following way: at step 3, for $k = 3$ Eq. 4.14 becomes

$$L(\tau_\mu) = q_2 \frac{(3\tau_\mu)^3}{2} \frac{d^3\Phi}{d\epsilon^3}, \tag{4.25}$$

where $\epsilon = t - t'$ and $\Phi(\epsilon) = \ln(1 + \epsilon^{0.1})$.

Eq. 4.16 at step 4 is then modified in the following way

$$\frac{1}{E(\tau_\mu)} = A(\tau_\mu) = \left(\sqrt{\frac{1}{t_{n+1/2}}} + \frac{q_3}{q_2} \right) L(\tau_\mu) \ln(10) \Delta(\log(\tau_\mu)). \tag{4.26}$$

The effective incremental modulus of the aging Kelvin chain can be evaluated at mid-step a according to Eq. 4.20

$$E^{ve}_{n+1/2} = \left(\frac{1}{E_0} + \left(\sqrt{\frac{1}{t_{n+1/2}}} + \frac{q_3}{q_2} \right) \sum_{\mu=1}^{N} A(\tau_\mu)_{n+1/2} (1 - \tilde{\lambda}(\tau_\mu)) \right)^{-1}, \tag{4.27}$$

The creep strain increment is then evaluated, by considering aging, using the following expression

$$\Delta\boldsymbol{\varepsilon}^{c}_{n+1} = \left(\sqrt{\frac{1}{t_{n+1/2}}} + \frac{q_3}{q_2}\right) \sum_{\mu=1}^{N} \left(1 - e^{-\Delta t/\tau_\mu}\right) \boldsymbol{\lambda}(\tau_\mu)_n, \tag{4.28}$$

where $\boldsymbol{\lambda}(\tau_\mu)_n$ assume the following expression

$$\boldsymbol{\lambda}(\tau_\mu)_{n+1} = \tilde{\lambda}(\tau_\mu) A(\tau_\mu)_{n+1/2} \boldsymbol{Z} \Delta\boldsymbol{\sigma}_{n+1} + \beta(\tau_\mu)\boldsymbol{\lambda}(\tau_\mu)_n, \tag{4.29}$$

with $\Delta\boldsymbol{\sigma}^{c}_{n+1} = -(1-\omega_{n+1})\boldsymbol{D}^{ve}_{n+1/2}(\Delta\boldsymbol{\varepsilon}^{c}_{n+1})$, and $\Delta\boldsymbol{\sigma}_{n+1} = \boldsymbol{\sigma}^{ep}_{n+1} + \Delta\boldsymbol{\sigma}^{c}_{n+1} - \boldsymbol{\sigma}_n$.

Finally, the total creep strain is evaluated by summing the creep strain at Eq. 4.28 to the additional creep strain increment due to the viscous component of the B3 model,

$$\Delta\boldsymbol{\varepsilon}^{c}_{n+1} = \left(\sqrt{\frac{1}{t_{n+1/2}}} + \frac{q_3}{q_2}\right) \sum_{\mu=1}^{N} \left(1 - e^{-\Delta t/\tau_\mu}\right) \boldsymbol{\lambda}(\tau_\mu)_n + q_4 \boldsymbol{\sigma}_n \frac{\Delta t}{t_{n+1/2}}. \tag{4.30}$$

4.5 Visco-elasto-plastic damage constitutive tangent operator

The visco-elasto-plastic tangent operator $\boldsymbol{D}^{vep}$ can be expressed as a function of the elasto-plastic tangent operator $\boldsymbol{D}^{ep}$ and the visco-elastic tangent operator $\boldsymbol{D}^{ve}$. The total strain at step $(n+1)$ can be written as

$$\boldsymbol{\varepsilon}_{n+1} = \boldsymbol{\varepsilon}^{e}_{n+1} + \boldsymbol{\varepsilon}^{p}_{n+1} + \boldsymbol{\varepsilon}^{c}_{n+1} = \boldsymbol{\varepsilon}^{ve}_{n+1} + \boldsymbol{\varepsilon}^{p}_{n+1}, \tag{4.31}$$

where $\boldsymbol{\varepsilon}^{ve} = \boldsymbol{\varepsilon}^{e}_{n+1} + \boldsymbol{\varepsilon}^{c}_{n+1}$ is the visco-elastic strain. Recalling equation 4.2, the stress $\boldsymbol{\sigma}_{n+1}$ is a function of the visco-elastic strain at step $(n+1)$. By using the chain rule the tangent visco-elasto-plastic operator $\boldsymbol{D}^{vep}$ yields

$$\boldsymbol{D}^{vep} = \frac{\partial\boldsymbol{\sigma}_{n+1}\left(\boldsymbol{\varepsilon}^{ve}_{n+1}\right)}{\partial\boldsymbol{\varepsilon}_{n+1}} = \frac{\partial\boldsymbol{\sigma}_{n+1}}{\partial\boldsymbol{\varepsilon}^{ve}_{n+1}} \frac{\partial\boldsymbol{\varepsilon}^{ve}_{n+1}}{\partial\boldsymbol{\varepsilon}_{n+1}} = (1-\omega_{n+1})\boldsymbol{D}^{ve}_{n+1/2} \frac{\partial\boldsymbol{\varepsilon}^{ve}_{n+1}}{\partial\boldsymbol{\varepsilon}_{n+1}}. \tag{4.32}$$

The visco-elastic strain is a function of the plastic strain, where the plastic potential is evaluated

at the beginning of the time interval

$$\boldsymbol{\varepsilon}^{ve}_{n+1} = \boldsymbol{\varepsilon}_{n+1} - \boldsymbol{\varepsilon}_n - \Delta\boldsymbol{\varepsilon}^{p}_{n+1} = \boldsymbol{\varepsilon}_{n+1} - \boldsymbol{\varepsilon}_n - \dot{\gamma}\frac{\partial g_p}{\partial \boldsymbol{\sigma}^{ep}_{n+1}}. \tag{4.33}$$

Taking the derivative of $\boldsymbol{\varepsilon}^{ve}_{n+1}$ over the total strain, yields

$$\frac{\partial \boldsymbol{\varepsilon}^{ve}_{n+1}}{\partial \boldsymbol{\varepsilon}_{n+1}} = \boldsymbol{I} - \dot{\gamma}\frac{\partial^2 g_p}{\partial(\boldsymbol{\sigma}^{ep}_{n+1})^2}\frac{\partial \boldsymbol{\sigma}^{ep}_{n+1}}{\partial \boldsymbol{\varepsilon}_{n+1}} = \boldsymbol{I} - \dot{\gamma}\frac{\partial^2 g_p}{\partial(\boldsymbol{\sigma}^{ep}_{n+1})^2}\boldsymbol{D}^{ep}. \tag{4.34}$$

Hence, the constitutive tangent operator for the visco-elasto-plastic model is defined as

$$\boldsymbol{D}^{vep} = (1-\omega_{n+1})\boldsymbol{D}^{ve}_{n+1/2}\left(\boldsymbol{I} - \dot{\gamma}\frac{\partial^2 g_p}{\partial(\boldsymbol{\sigma}^{ep}_{n+1})^2}\boldsymbol{D}^{ep}\right). \tag{4.35}$$

4.6 The "return to apex" algorithm

The convergence of the backward-Euler return mapping algorithm described in Section 4.2 relies upon the intersection of the normal vector to the plastic potential $\frac{\partial g}{\partial \boldsymbol{\sigma}}$ with the yield surface. For concrete behaviour in compression, the intersection point is always found. However, with regards to tension, it may happen that no intersection is found, as shown in Fig. 4.5, where the trial solution is overcoming the apex point.

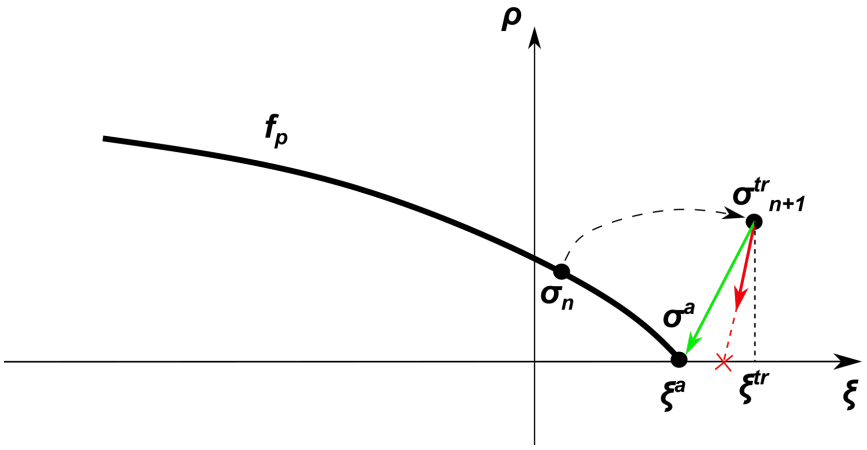

Figure 4.5: Classical return-mapping procedure in traction (the projection vector in shown in red).

In order to tackle this issue, we assume that the solution we are looking for is located and the apex, and therefore a proper "return to apex" procedure is implemented. It is represented by the green line in Fig. 4.5, and allows for the correction along both the hydrostatic line and the deviatoric plane.

First of all, it must be checked if the return to apex procedure is necessary. This is achieved by controlling if ξ^{tr} overcomes or not ξ^a. The mathematical expression of ξ^a is obtained from Eq. 3.27, imposing $f_p = 0$ and $\rho = 0$. It yields

$$\xi^a\left(\kappa, \kappa_c, \kappa_t, \kappa_f\right) = \frac{\sqrt{3}\left(1-\omega^*\right) f_c}{m} q_s(\kappa) q_f\left(\kappa_f\right). \tag{4.36}$$

if $\xi^{tr} > \xi^a$, the "return to apex" procedure must be activated. The equations of "return to apex" procedure are derived here below. Recalling for convenience the expression of the residual of the return-mapping equations (Eq. 4.8)

$$\boldsymbol{r} = \boldsymbol{\sigma}^{ep}_{n+1} - \boldsymbol{\sigma}^{tr}_{n+1} + \left(1-\omega_{n+1}\right) \boldsymbol{D}^{ve}_{n+1/2} \Delta\varepsilon^p_{n+1}, \tag{4.37}$$

the plastic strain increment required for the projection of the trial stress onto the apex point is obtained by substituting $\boldsymbol{\sigma}^{ep}_{n+1}$ with $\boldsymbol{\sigma}^a$ in the expression of the residual

$$\Delta\boldsymbol{\varepsilon}^p_{n+1} = \frac{1}{1-\omega_{n+1}} \left(\boldsymbol{D}^{ve}_{n+1/2}\right)^{-1} \left[\boldsymbol{\sigma}^{tr}_{n+1} - \boldsymbol{\sigma}^a\right]. \tag{4.38}$$

Then, the internal variables for plasticity, damage and fatigue can be expressed as functions of $\Delta\boldsymbol{\varepsilon}^p_{n+1}$ as follows

$$\begin{aligned}
\kappa_{n+1} &= \kappa_n + \left|\mathrm{Tr}\left(\Delta\varepsilon^p_{n+1}\right)\right| \\
\kappa_{c,n+1} &= \kappa_{c,n} + \frac{1}{2}\sum_{i=1}^{3}\left(\left|\Delta\varepsilon^p_{n+1,i}\right| - \Delta\varepsilon^p_{n+1,i}\right) \\
\kappa_{t,n+1} &= \kappa_{t,n} + \frac{1}{2}\sum_{i=1}^{3}\left(\left|\Delta\varepsilon^p_{n+1,i}\right| + \Delta\varepsilon^p_{n+1,i}\right) \\
\kappa_{f,n+1} &= \kappa_{f,n} + \frac{1}{2}\sum_{i=1}^{3}\left(\left|\Delta\varepsilon^e_{n+1,i}\right| + \Delta\varepsilon^e_{n+1,i}\right),
\end{aligned} \tag{4.39}$$

with $\Delta\boldsymbol{\varepsilon}^e_{n+1} = \Delta\boldsymbol{\varepsilon}_{n+1} - \Delta\boldsymbol{\varepsilon}^p_{n+1}$.

As the apex stress is function of the internal variables for plasticity, damage, and fatigue, the resolution of the Eq. 4.39 and 4.38 require an iterative scheme. The iterations are done, until the norm of the residual is less than a given tolerance

$$\|\boldsymbol{r}\| = \Delta\boldsymbol{\varepsilon}^p_{n+1} - \frac{1}{1-\omega_{n+1}} \left(\boldsymbol{D}^{ve}_{n+1/2}\right)^{-1} \left[\boldsymbol{\sigma}^{tr}_{n+1} - \boldsymbol{\sigma}^a\right] < \text{Toll.} \tag{4.40}$$

Chapter 5

Numerical results

In this section, numerical tests are performed to evaluate the capabilities of the model to reproduce the non-linear mechanical behaviour of concrete under different loading conditions. First, each component of the unified model is calibrated and validated against experimental results taken from literature. Then, meso-scale numerical tests are performed on the unified model. The analyses are performed via the Abaqus Software [207], in which the constitutive model described in the previous sections has been implemented within the user subroutine UMAT.

5.1 Calibration and validation of the plastic-damage model

In order to calibrate the plastic-damage model, the response of the constitutive model is compared with results from tri-axial compression tests conducted by [208]. An axial compressive stress is gradually applied under displacement control on a saturated cylindrical specimen of concrete, considering different levels of confinement and water to cement ratio w/c equal to 0.55. First, the calibration is done considering a fixed confinement pressure f_{cc} equal to 8.6 MPa. Then, the constitutive parameters obtained after calibration are used to validate the model considering different levels of confinement pressures equal to 0.0 MPa, 2.1 MPa, 4.3 MPa, 17.2 MPa and 30.1 MPa. The constitutive parameters are reported in Table 5.1, while the superposition of numerical and

experimental results, is shown in Fig. 5.1.

E (MPa)	ν	f_c (MPa)	f_t (MPa)	e	t_s	κ_{1D}	q_{h0}	A	B	κ_{c0}
29600	0.22	47.4	3.05	0.55	0.003	0.1	0.4	-2.22	-3.46	0.015
A_c	B_c	$\omega_{c,max}$	κ_{t0}	A_t	B_t	$\omega_{t,max}$	s_0	G_f (J/m^2)	w_c (mm)	–
1	100	0.95	0.0015	1	1	0.95	0.2	25	1	–

Table 5.1:
Plastic-damage constitutive parameters for the cement matrix.

It can be seen in Fig. 5.1 that the plastic-damage model is able to catch correctly the material behaviour with increasing confinement levels. Specifically, the peak stresses and the post-peak responses are reproduced fairly well.

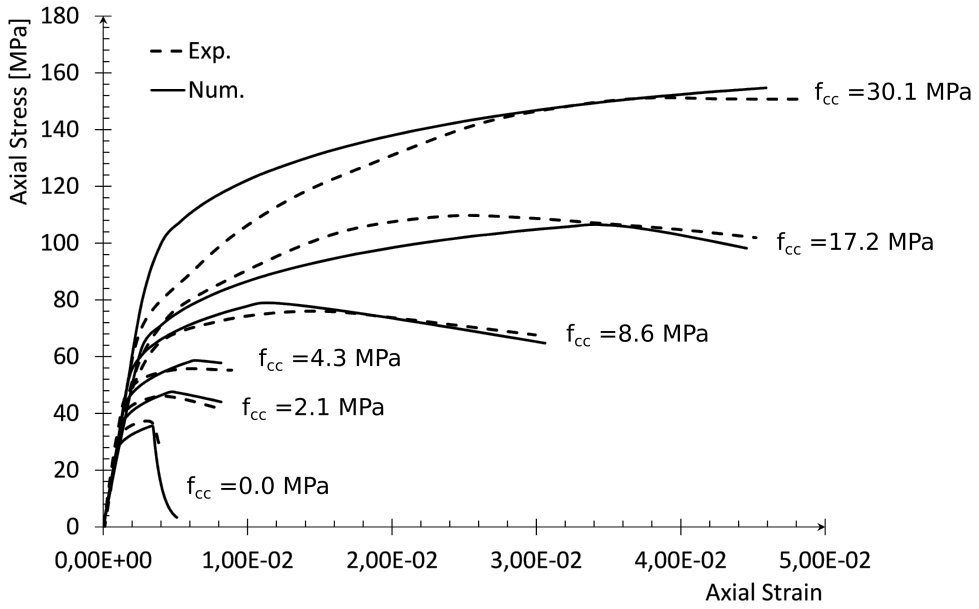

Figure 5.1: Experimental and numerical comparisons for different confinement levels.

Figure 5.2 depicts the evolution of damage with respect to the equivalent plastic strain, at varying confinement levels. It comes out that, the confinement pressure has a strong effect on the damage evolution pattern. Less confined specimens accumulate damage very fast, especially at the beginning of the loading process, where the damage rate is very high.

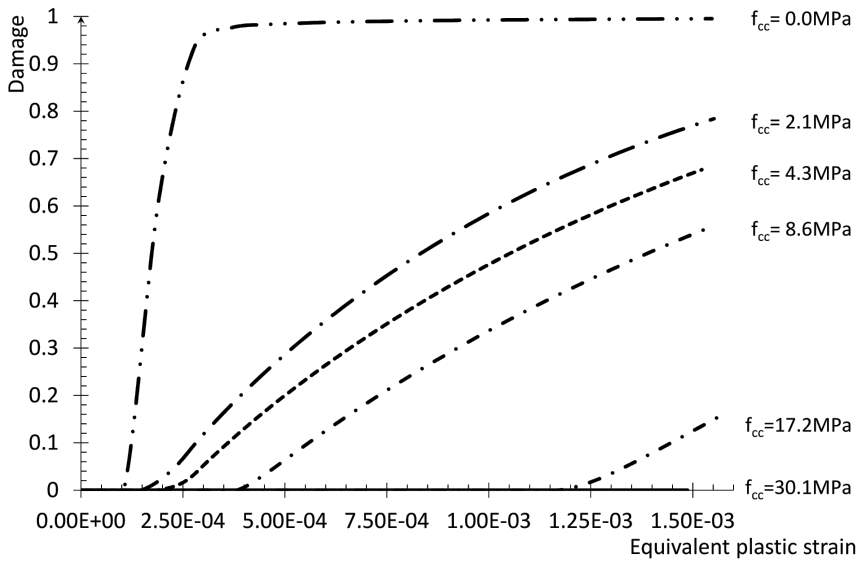

Figure 5.2: Damage evolution for different confinement levels.

Then, the response of he plastic-damage model to a cyclic axial compressive stress under displacement control, with a constant confinement level f_{cc} equal to 8.6 MPa is considered. The juxtaposition between the numerical and experimental results is shown in Fig. 5.3, where a good agreement between experimental and numerical results can be observed. In particular, the model is able to reproduce fairly well the closed loops observed during the elastic unloading and reloading. This is due to the stiffness recovery function, incorporated in the damage variable ω used in the constitutive law.

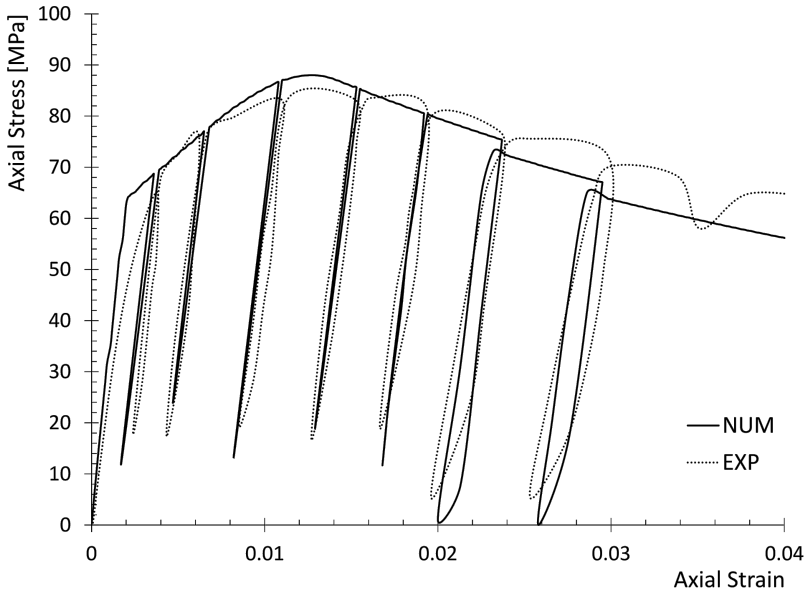

Figure 5.3: Constitutive cyclic response.

5.2 Calibration and validation of the creep model

Among the calibrating parameters for the exponential algorithm, the choice of the number of Kelvin units m and m_d, for the basic and drying creep respectively, and the corresponding sets of retardation times are briefly discussed in the following section. Some suggestions for the appropriate choice of the retardation times can be found in [205]. In particular, the set of retardation times must cover the entire range of time of interest. Moreover, the smallest retardation time must be small enough than the time of load application, in order to capture the irreversible effects of concrete aging at young ages. A spacing of decades in the logarithmic scale between the retardation time proves to produce creep curves that are smooth enough [205].

In order to evaluate the number of Kelvin units m for the basic creep that is sufficient for

an accurate creep algorithm, a creep test on a cubic sample of concrete is considered. A load corresponding to a uniform unit pressure is applied instantaneously on the top of the cube at 28 days, and the deformation is observed for 10000 days. The simulation is done considering autogenous conditions. Therefore, no exchange of humidity with the environment takes place, and the drying creep can be neglected. In this simple case, the analytical solution is expected to be equal to the product between the basic creep compliance function and the Heaviside step function [196]. The same problem is solved numerically by implementing the exponential algorithm to the basic creep part of the B3 model. Three different sets of retardation times are considered: a first set with 13 Kelvin units with the smallest retardation time $\tau_1 = 10^{-7}$ days; a second set of 18 Kelvin units with the smallest retardation time $\tau_1 = 10^{-9}$ days; and, finally, a set of 22 Kelvin units with the smallest retardation time $\tau_1 = 10^{-15}$ days. The spacing between the retardation times is uniformly equal to 10 in the logarithmic scale. The parameters of the model B3 are evaluated considering the material properties reported in Table 5.2. The comparison between the numerical and analytical results is shown in Figure 5.4a. Table 5.3 reports the maximum and mean error between the analytical and numerical solutions for each case.

Material property	
Young modulus (E)	30000 (MPa)
Poisson's ratio (ν)	0.15
Strength at 28 days (f_c)	27.58 (MPa)
Water-cement ratio (w/c)	0.6
Aggregate-cement ratio (a/c)	7
Cement content (c)	219.29 (kg/m^3)

Table 5.2: Material properties for the basic creep test.

Number of Kelvin units	Max. error (%)	Mean error (%)
13 (with $\tau_1 = 10^{-7}$ days)	17.7	7.7
18 (with $\tau_1 = 10^{-9}$ days)	12.7	4.9
22 (with $\tau_1 = 10^{-15}$ days)	5.7	1

Table 5.3: Maximum and mean errors between analytical and numerical solutions of the basic creep strain.

Figure 5.4a alongside Table 5.3 show that a total number m of 22 Kelvin units leads to an accurate enough approximation. Therefore, the set of retardation times for the implementation of

the basic creep is the following

$$\tau_{\mu,basic} = 10^{\mu-1}\tau_{1,basic};\ \ \mu = 2,3,\ldots,22;\ \ \tau_{1,basic} = 10^{-15}days. \tag{5.1}$$

A different set of retardation times must be selected for the drying creep. In order to increase the accuracy of the exponential algorithm for the drying creep, two strategies are simultaneously adopted. The first one consists in the reduction of the spacing between the retardation times in the logarithmic scale from 10 to $\sqrt{10}$. Further, with reference to [209], Jirásek and Havlásek have demonstrated that there is no substantial gain in accuracy by increasing the derivative order in Eq. 4.14, but rather by the adjustment of the discrete retardation times. Therefore, the second strategy consists in multiplying the retardation times by a constant factor $\psi = 1.3$. The retardation times for the drying creep are, therefore, selected as

$$\tau_{\mu,drying} = 10^{0.5(\mu-1)}\tau_{1,drying};\ \ \mu = 2,3,\ldots,25;\ \ \tau_{1,drying} = 10^{-7}days. \tag{5.2}$$

The reliability of the implemented total creep (basic + drying creep) algorithm with the above-mentioned retardation times is evaluated by comparison between the analytical total creep curve and the numerical one, obtained by using the same creep parameters as for the basic creep model described above. Figure 5.4b shows the superposition between the analytical and numerical curves at varying humidity content, while Table 5.4 shows the corresponding maximum and mean errors.

Relative humidity h	Max. error (%)	Mean error (%)
0.5	12.1	8.4
0.6	8.5	5
0.7	6.5	3.1
0.8	5.7	2.1
0.9	5.7	1.7

Table 5.4: Maximum and mean errors between analytical and numerical solutions of the total creep strain for different values of relative humidity.

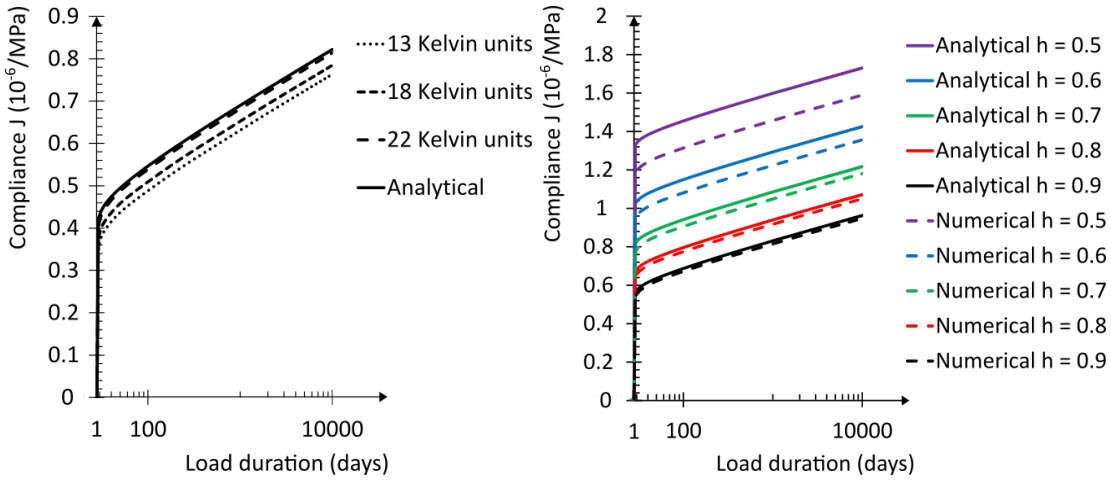

Figure 5.4: Comparison between numerical and analytical results for the basic creep (a), and total (basic + drying) creep (b).

In order to validate the implementation of the exponential algorithm for the B3 model, an experimental creep test is considered. To this aim, reference is made to the experiment carried out by Ranaivomanana, Multon and Turatsinse at Toulouse University, by focusing on the compression test [210]. Compressive creep tests were carried out on cylindrical specimens of 110 mm in diameter and 220 mm in height. From the concrete composition, the specific calibrating parameters derived for the creep model are reported in Table 5.5.

Model parameters	
Young modulus (E)	41925 (MPa)
Poisson's ratio (ν)	0.1
Number of Kelvin units for basic creep (m)	22
Number of Kelvin units for drying creep (m_d)	25
Time of load application (t')	28 (days)
Strength at 28 days (f_c)	69.7 (MPa)
Water-cement ratio (w/c)	0.44
Aggregate-cement ratio (a/c)	4.5
Cement content (c)	400 (kg/m^3)
2 $\times$ volume to surface ratio (D)	44 (mm)
Relative humidity (h)	1
Time at which drying starts (t_0)	28 (days)

Table 5.5: Constitutive parameters for the creep model.

Figure 5.5 reports the comparison between experimental and numerical creep curves. The close juxtaposition between the two curves indicate promising capabilities of the model to predict the long-term deformation of concrete under sustained loadings.

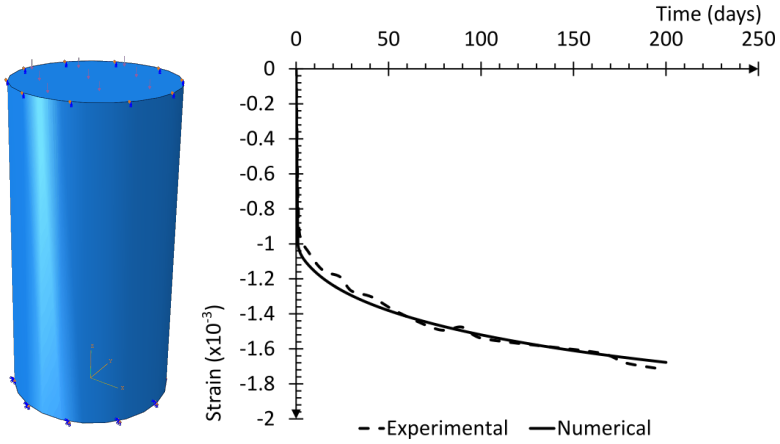

(a) (b)

Figure 5.5: Concrete cylinder numerical model (a), and comparison between numerical and experimental results (b).

5.3 Calibration and validation of the fatigue model

5.3.1 Cyclic compression tests with different maximum stress levels

The model has been calibrated and validated against cyclic compression tests from [6]. An axial cyclic compressive load is applied under force-controlled at the top of a cylindrical specimen of concrete. The minimum stress level was kept constant at $S_{min} = 0.05$ in all tests, while the maximum stress level was either $S_{max} = 0.85$ and 0.70. The quantity S is equal to the ratio between the applied stress and the compressive strength. The frequency of the tests is equal to 1 Hz, and three specimens were tested for each stress level. The domain has been discretized using 8-nodes linear brick, as shown in Fig. 5.6.

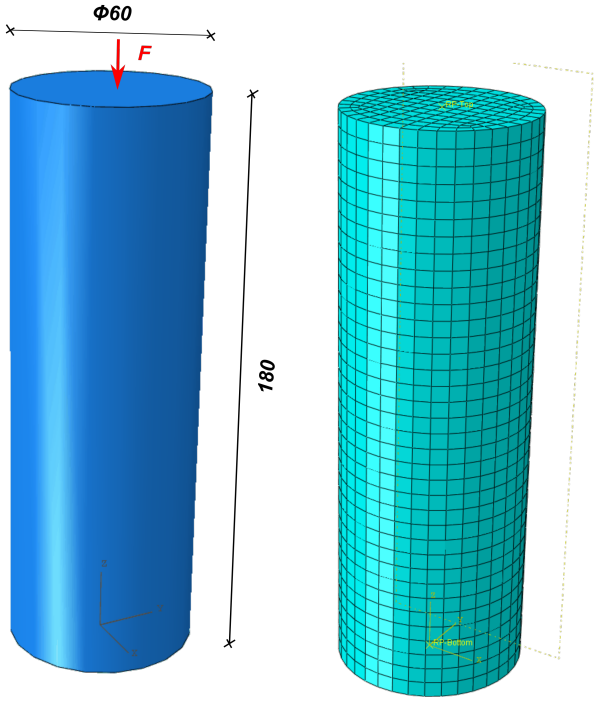

Figure 5.6: Numerical model.

The model has been calibrated considering $S_{max} = 0.85$, and the material parameters obtained after calibration and reported in Table 5.6, have been used to validate the model, considering $S_{max} = 0.70$. At this stage, the creep model is deactivated, due to the small time scale into consideration. Fig. 5.7 and 5.8 show the juxtaposition between the experimental and numerical fatigue curves related to the strain development at the maximum stress level (peak strain), and at the minimum stress level (valley strain), for $S_{max} = 0.85$ and $S_{max} = 0.70$ respectively. On the same Figures, are reported the juxtapositions between the numerical and experimental fatigue modulus, which is evaluated as the ratio of the maximum stress to the peak strain [211].

E (MPa)	ν	f_c (MPa)	f_t (MPa)	e	t_s	κ_{1D}	q_{h0}	A	B	κ_{c0}	
30000	0.2	96	12	0.55	0.005	0.0005	0.7	-2.22	-3.46	0.015	
A_c	B_c	$\omega_{c,max}$	κ_{t0}	A_t	B_t	$\omega_{t,max}$	s_0	G_f (J/m^2)	w_c (mm)	a	γ_t
1	100	0.95	0.01	1	0.2	0.95	0.2	25	1	0.085	0.01

Table 5.6:
Constitutive parameters after calibration.

It can be seen, that the experimental and the numerical results agree fairly well. In particular, the model is able to catch the three-stage pattern for the strain development and the fatigue modulus, and the gradient of the curves during the secondary stage is fairly well depicted. Furthermore, the computed number of cycles to failure are within the minimum and maximum tested values.

The plots of the average equivalent plastic strain at the middle section of the cylindrical specimen are reported in Fig. 5.9 for both the maximum stress levels. it can be seen that, it shows the same three-stage pattern as the fatigue curves. This supports the idea that, the presented model considers the accumulation of plastic strains, as the macroscopic indicator which is responsible of the fatigue degradation of concrete materials.

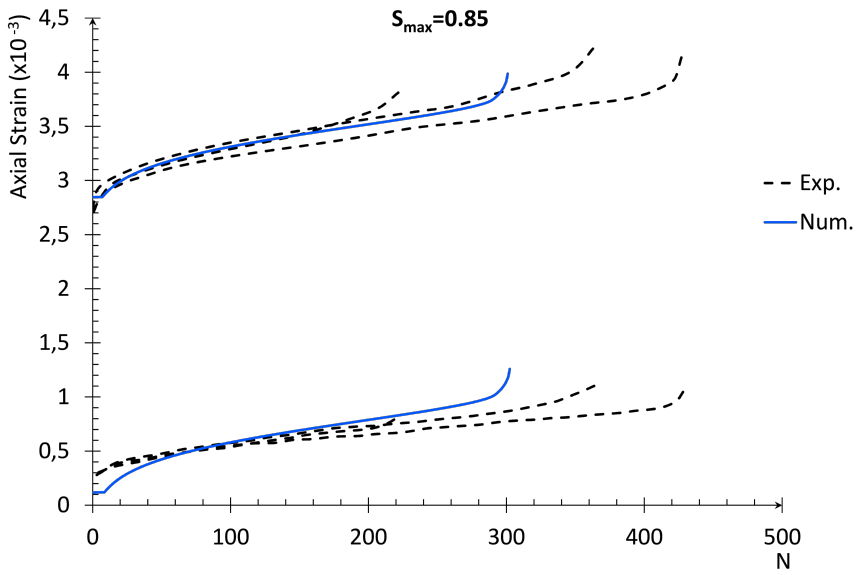

(a)

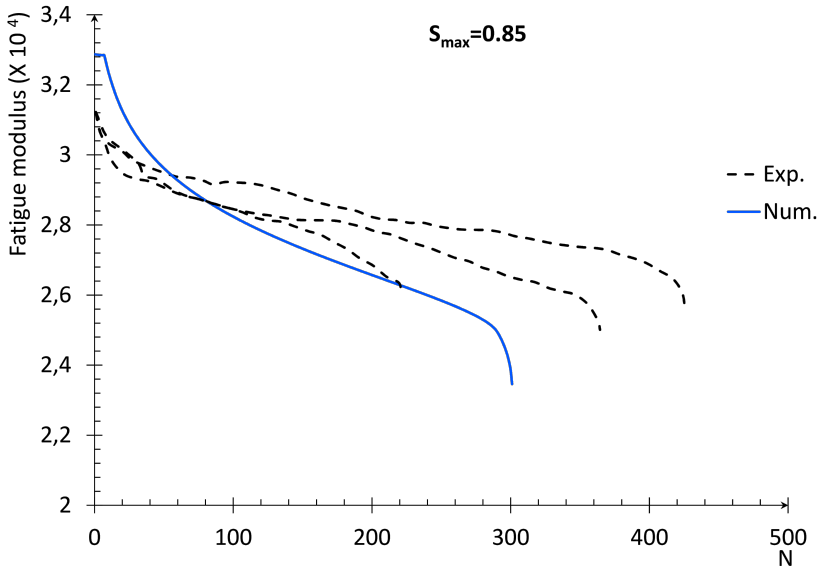

(b)

Figure 5.7: Comparison between numerical and analytical results for peak and valley strains (a), and fatigue modulus (b), for $S_{max} = 0.85$.

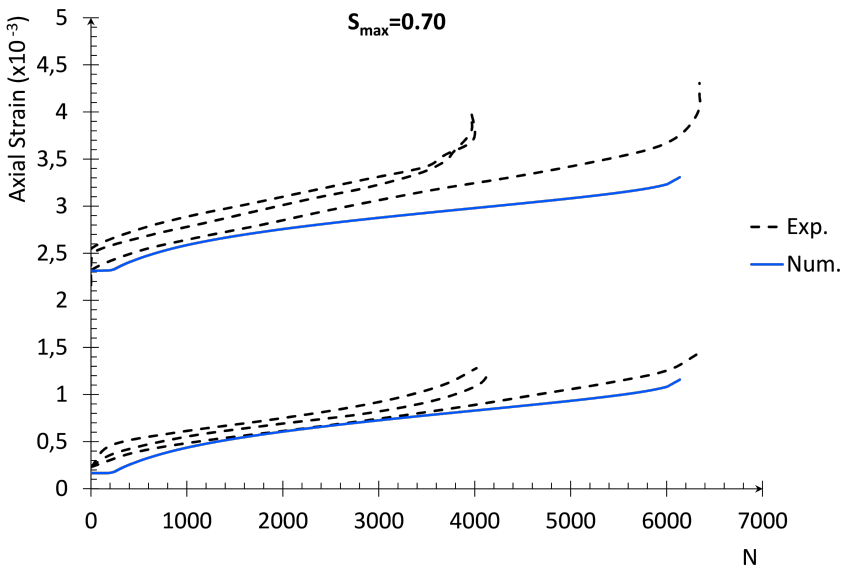

(a)

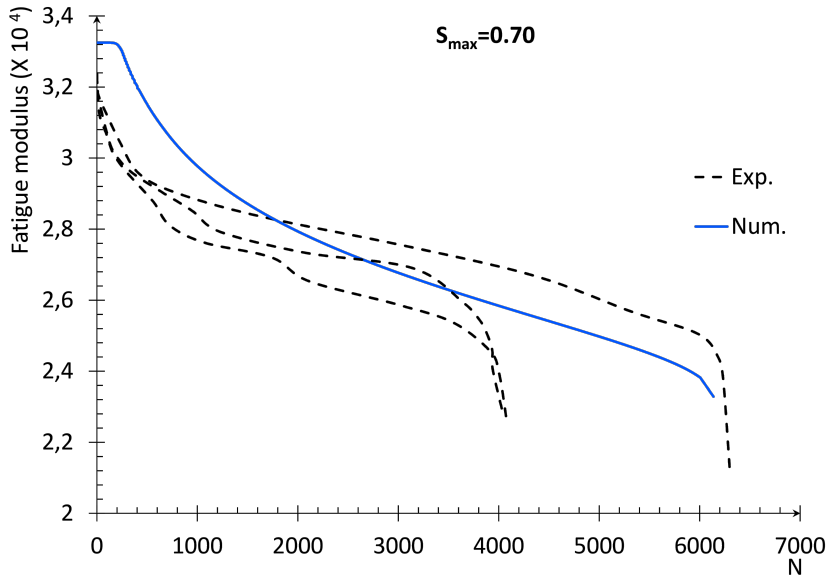

(b)

Figure 5.8: Comparison between numerical and analytical results for peak and valley strains (a), and fatigue modulus (b), for $S_{max} = 0.70$.

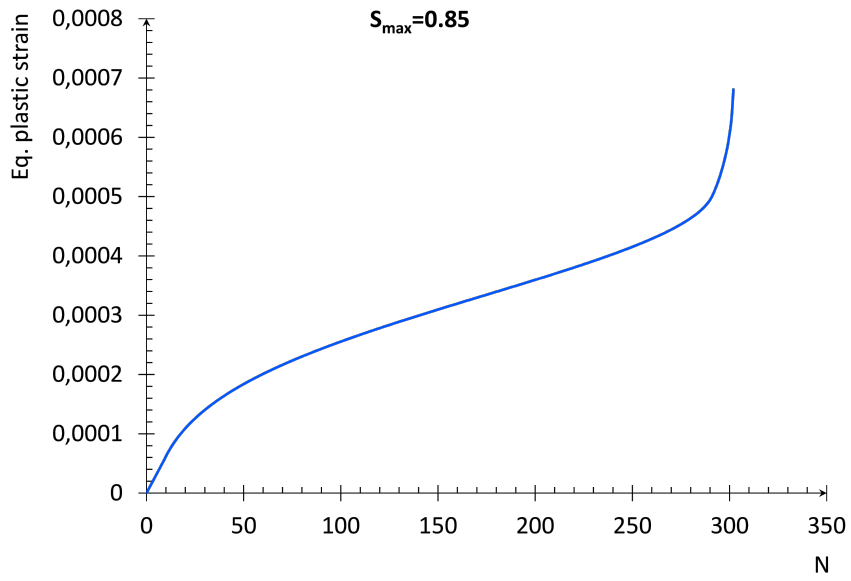

(a)

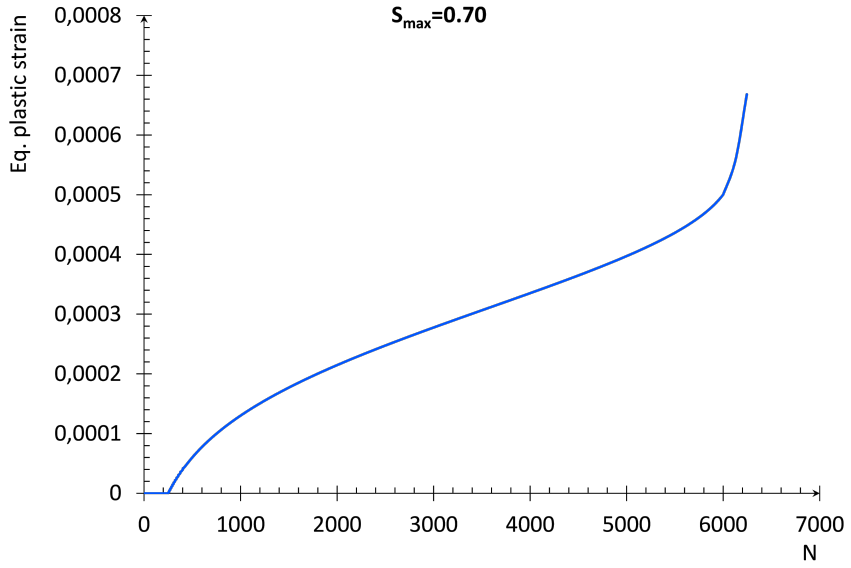

(b)

Figure 5.9: Average equivalent plastic strain for $S_{max} = 0.85$ (a), and $S_{max} = 0.70$ (b).

5.3.2 Cyclic tension-compression tests with different confinement levels

The fatigue model has been calibrated against tri-axial tension-compression cyclic tests from [87]. The test were carried out on tapered prism specimens, and both ends of each specimen have been enlarged to avoid stress concentrations (see Fig. 5.10). The applied sinusoidal waveform cyclic loading has a maximum stress level $\sigma_{max} = 0.55 f_t$, and a minimum stress level $\sigma_{min} = -0.2 f_c$, where f_t and f_c are the tensile and compressive strengths, respectively (by convention, tension is considered positive, and compression is considered negative). A lateral load is applied along the two horizontal directions of the specimen, considering three different levels of confinement ratio R (ratio between the lateral pressure and the compressive strength) equal to 0.3, 0.2, and 0.1. Five specimens were considered for each test. The domain has been discretized using 8-node linear bricks, and the enlargements of the concrete specimens were modeled with an elastic behaviour.

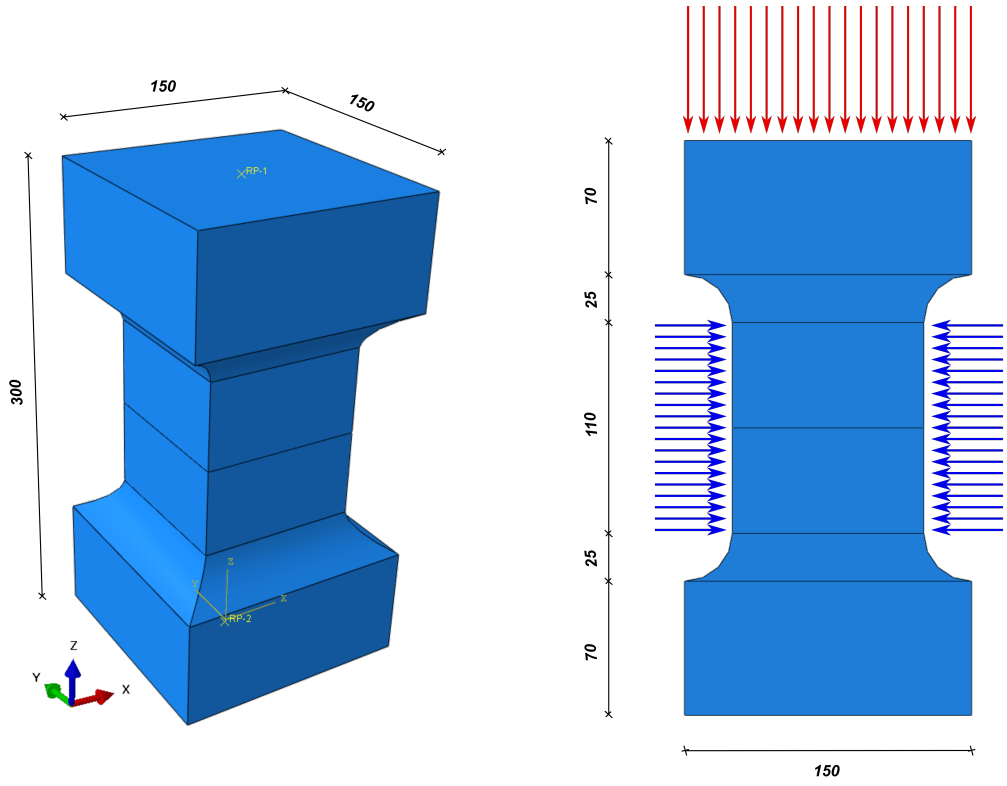

Figure 5.10: Numerical model.

The model has been calibrated considering $R = 0.3$, and the material parameters obtained after calibration are reported in Table 5.7. At this stage, the creep model is deactivated, due to the small time scale into consideration. Then, the model has been validated, considering $R = 0.2$ and $R = 0.1$.

E (MPa)	ν	f_c (MPa)	f_t (MPa)	e	t_s	κ_{1D}	q_{h0}	A	B	κ_{c0}	
32000	0.2	27	2.5	0.55	0.001	0.00001	0.6	-22.2	-34.6	0.015	
A_c	B_c	$\omega_{c,max}$	κ_{t0}	A_t	B_t	$\omega_{t,max}$	s_0	G_f (J/m^2)	w_c (mm)	a	γ_t
1	100	0.95	0.0001	1	0.2	0.95	0.2	25	1	0.0375	0.0015

Table 5.7:
Constitutive parameters after calibration.

Fig. 5.11 to 5.13 report the superposition between the experimental and numerical residual strains, versus the normalized number of cycles, for each confinement level.

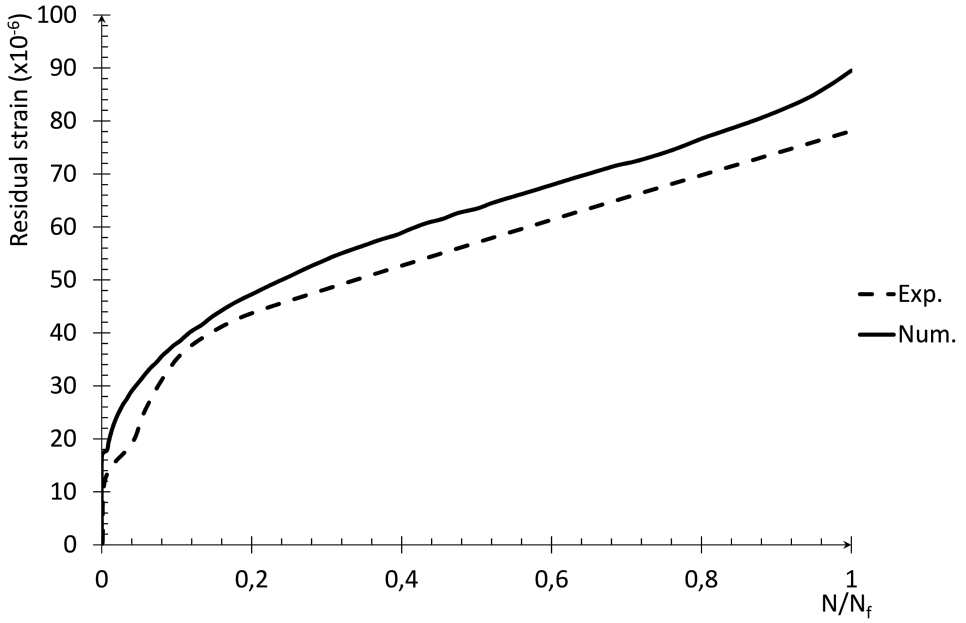

Figure 5.11: Numerical and experimental residual strains for $R = 0.3$.

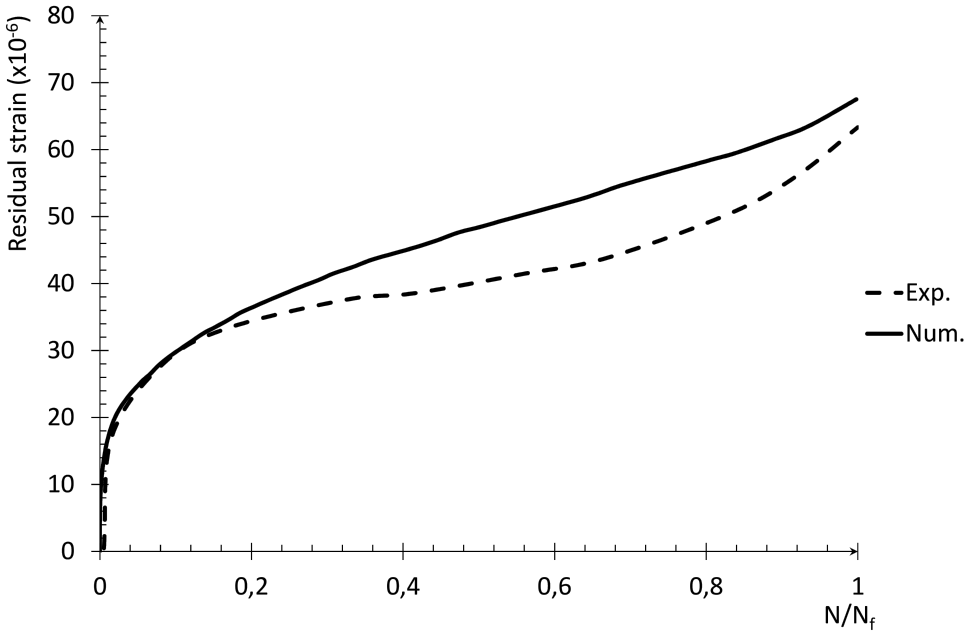

Figure 5.12: Numerical and experimental residual strains for $R = 0.2$.

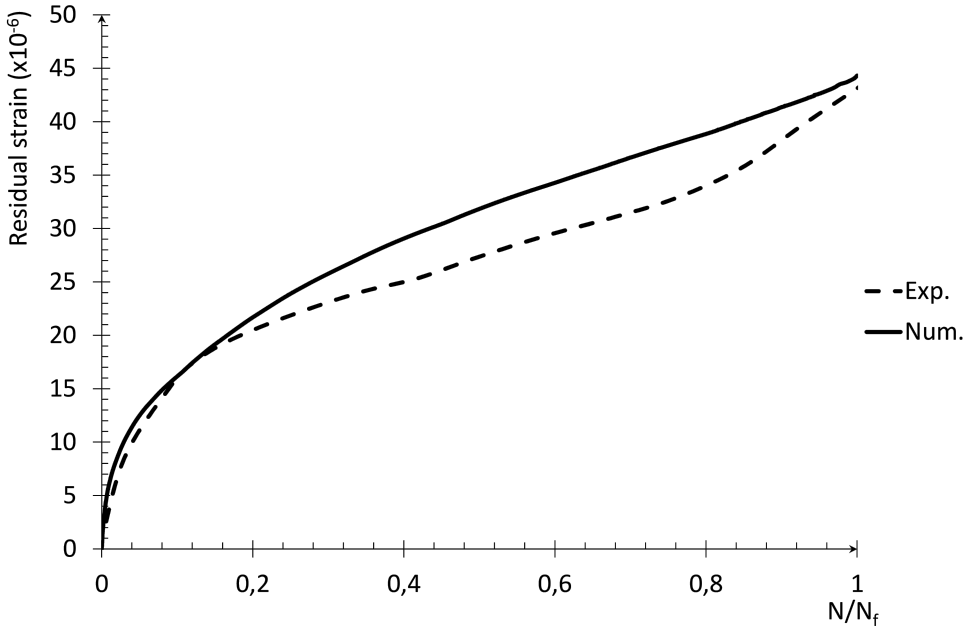

Figure 5.13: Numerical and experimental residual strains for $R = 0.1$.

It can be seen that, although the residual strains are slightly overestimated during the second stage and the third stage, the model is able to catch fairly well the first stage and the residual strain at failure. Furthermore, the computed number of cycles at failure, is very close to the average value of the tested number of cycles at failure for each confinement level, as shown in Fig. 5.14.

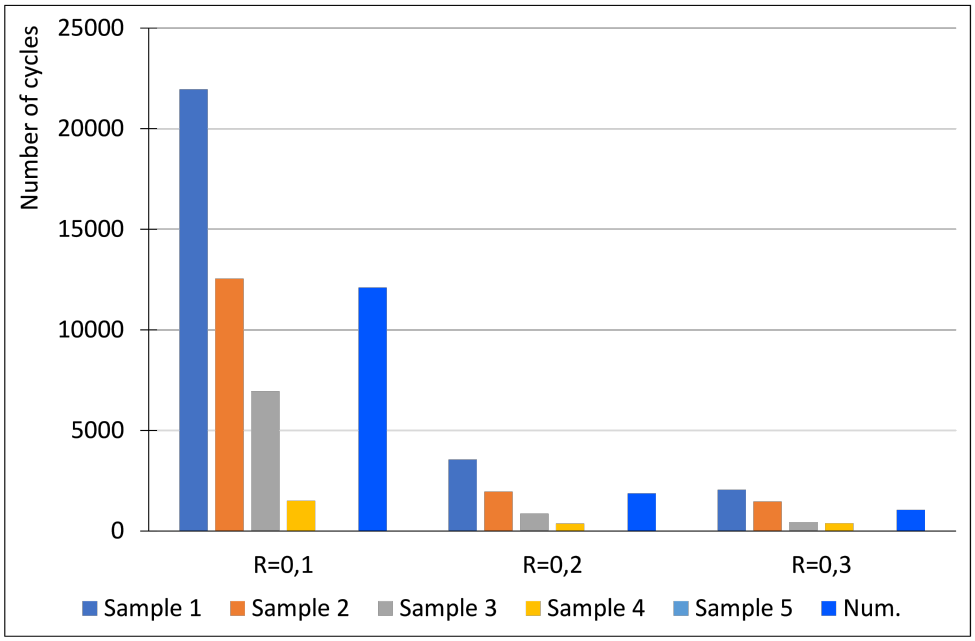

Figure 5.14: Numerical and experimental number of cycles at failure for different confinement levels.

5.4 Parametric study for some relevant model parameters

A parametric study is performed to assess the influence of the values of some relevant model parameters on the fatigue performance of the samples analyzed in the previous sections. The parameters under consideration are the concrete compressive strength f_c, the slope of the fatigue degradation function a, the initial hardening parameter q_{h0}, the tensile strength f_t, the initial equivalent plastic strain for damage in tension κ_{t0}, and finally, the threshold for the onset of fatigue degradation γ_t. The cyclic compression test described in Section 5.3.1 is selected to study the influence of the parameters f_c, q_{h0}, and a, considering $S_{max} = 0.85$. On the other hand, the study

of the influence of the parameters f_t, κ_{t0}, and γ_t, is done considering the cyclic tension-compression test described in Section 5.3.2, with $R = 0.3$.

5.4.1 Influence of f_c

In order to assess the influence of the parameter f_c, three different values are adopted, namely, 93, 96, and 100 MPa. The first value is lower than the one considered in the simulation in Section 5.3.1, while the third one is higher. The peak and valley strain developments are shown in Fig. 5.15. It can be seen that, the parameter f_c affects the fatigue curve in its whole, that is, all the three stages are affected. Specifically, increasing f_c, the secondary strain slope decreases, corresponding to a higher number of cycles prior to failure. Therefore, the parameter f_c has a positive effect on the fatigue performance. This is expected, since the size of the yield domain in compression increases with f_c.

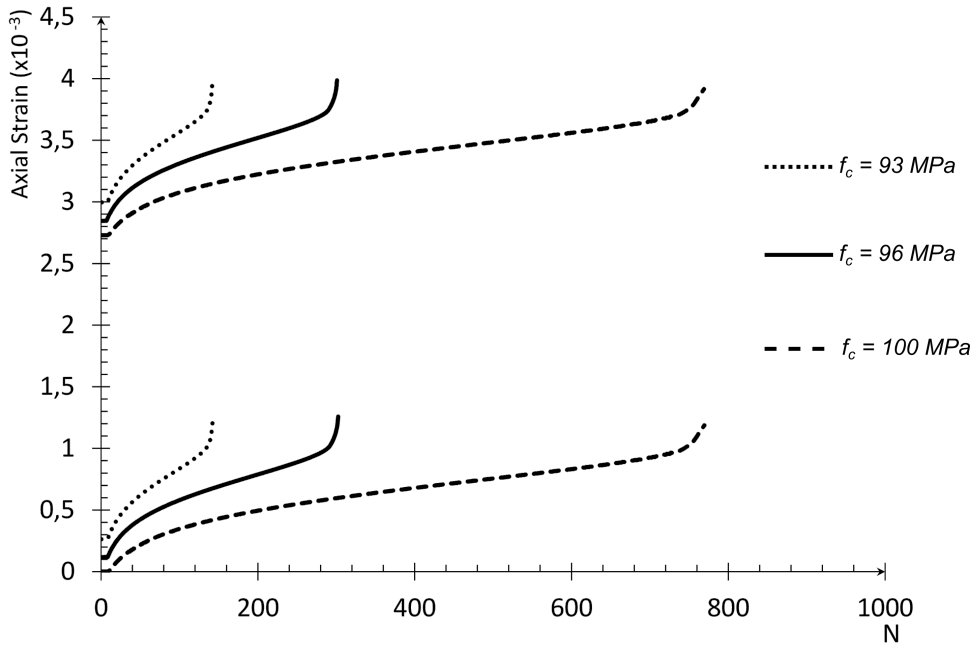

Figure 5.15: Effect of f_c on the strain development.

5.4.2 Influence of q_{h0}

In order to assess the influence of the parameter q_{h0}, three different values are adopted, namely, 0.55, 0.7, and 0.85. The first value is lower than the one considered in the simulation in Section 5.3.1, while the third one is higher. The peak and valley strain developments are shown in Fig. 5.16. It can be seen that, the parameter q_{h0} has a less important effect on the fatigue performance. The secondary strain slope and the number of cycles to failure are similar, for all three values. The main effect of the parameter q_{h0} is located in stage 1. As q_{h0} is related to the initial size of the elastic domain, higher values of the parameter means longer time in the elastic regime, for the same value of the parameter a, which is the rate at which the yield surface contracts. Therefore, the case in which $q_{h0} = 0.85$, shows a longer horizontal plateau at the beginning, which corresponds to the elastic regime.

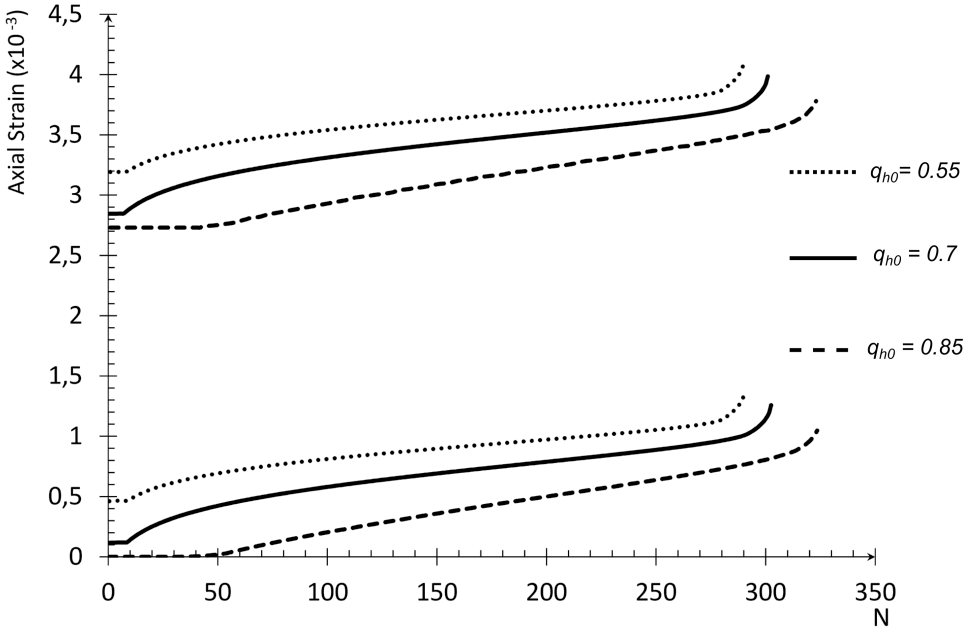

Figure 5.16: Effect of q_{h0} on the strain development.

5.4.3 Influence of a

In order to assess the influence of the parameter a, three different values are adopted, namely, 0.065, 0.085, and 0.1. The first value is lower than the one considered in the simulation in Section 5.3.1, while the third one is higher. The peak and valley strain developments are shown in Fig. 5.17. It can be seen that, the parameter a has a strong effect on the fatigue performance. Although the first stages are almost coincident, the secondary strain slope increases with a, which corresponds to a smaller number of cycles prior to failure. This is expected, since higher values of a means faster fatigue degradation rate, which is depicted by the slope of the secondary stage.

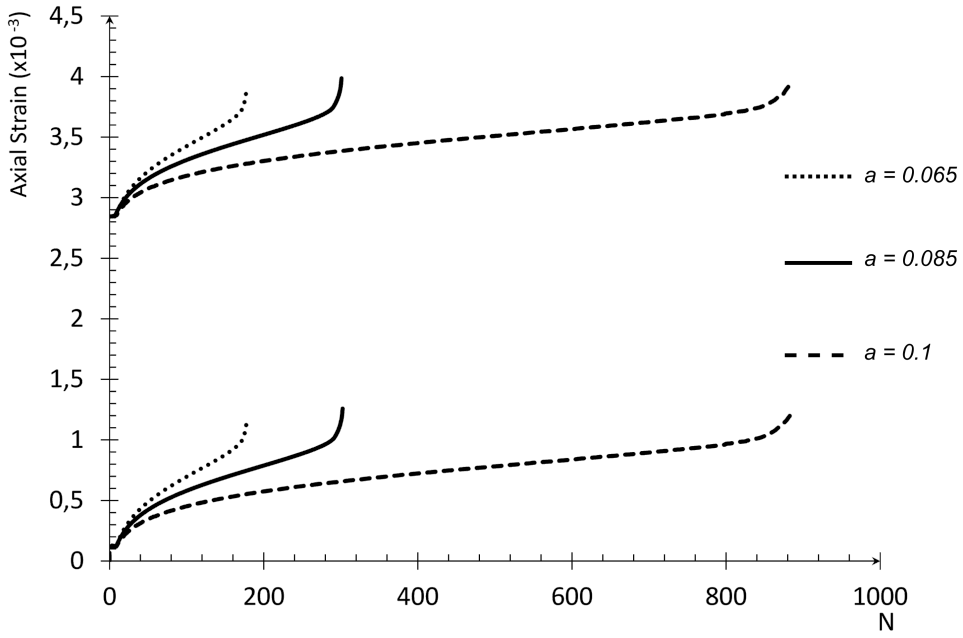

Figure 5.17: Effect of a on the strain development.

5.4.4 Influence of f_t

In order to assess the influence of the parameter f_t, three different values are adopted, namely, 2 MPa, 2.5 MPa, and 3 MPa. The first value is lower than the one considered in the simulation in Section 5.3.2, while the third one is higher. The residual strain curve is shown in Fig. 5.18. It can be seen that, a small change in the value of f_t can have a relevant effect on the fatigue

performance. A decrease in the tensile strength will lead to an increase in the secondary strain slope, and a reduction of the number of cycles prior to failure. This behaviour can be anticipated, given that the tensile strength is related to size of the elastic domain in tension.

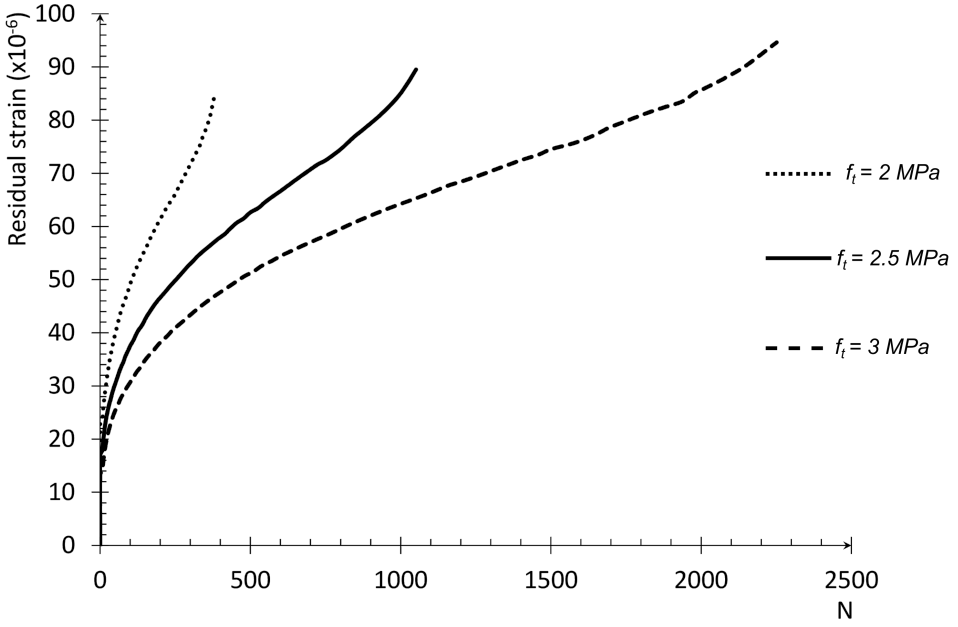

Figure 5.18: Effect of f_t on the strain development.

5.4.5 Influence of κ_{t0}

In order to assess the influence of the parameter κ_{t0}, three different values are adopted, namely, 5E-5, 1E-4 MPa, and 5E-4. The first value is lower than the one considered in the simulation in Section 5.3.2, while the third one is higher. The residual strain curve is shown in Fig. 5.19. It can be seen that, the parameter κ_{t0} has almost no effect in the first and second stages, since the fist stages and the secondary strain slopes are almost coincident. However, the number of cycles to failure seems to increase, with the value of κ_{t0}. Therefore, an earlier triggering of tensile damage, will lead to a premature failure.

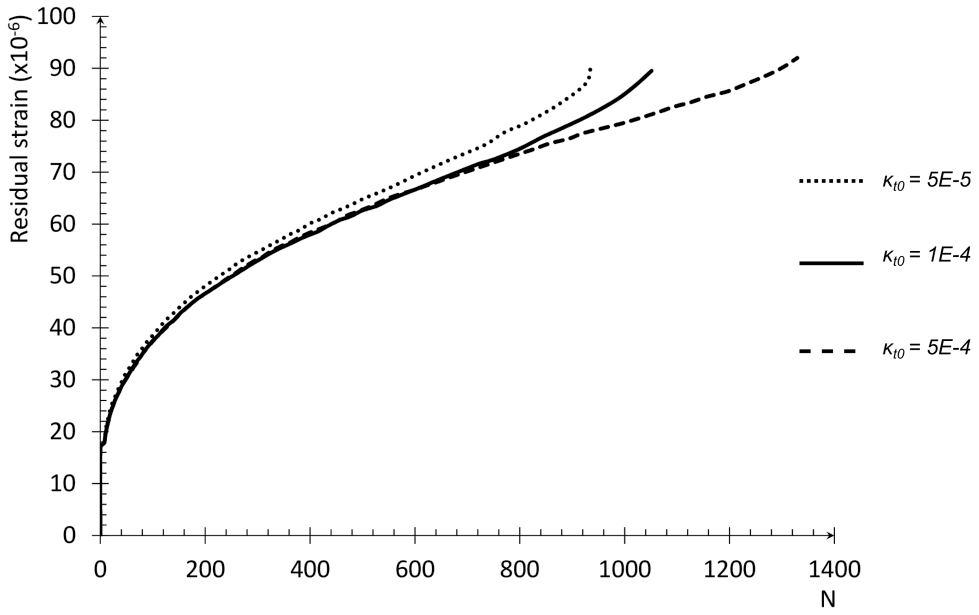

Figure 5.19: Effect of κ_{t0} on the strain development.

5.4.6 Influence of γ_t

In order to assess the influence of the parameter γ_t, three different values are adopted, namely, 1.5E-4, 1.5E-3, and 5E-3. The first value is lower than the one considered in the simulation in Section 5.3.2, while the third one is higher. The residual strain curve is shown in Fig. 5.20. It can be seen that, an earlier triggering of fatigue degradation has a detrimental effect on the fatigue performance. Specifically, the secondary strain slope and the number of cycles to failure seems to be very sensitive to the parameter γ_t. Furthermore, when the value of γ_t is very small, the strains develop very fast during the first stage, and the secondary stage disappears, leading to a premature failure.

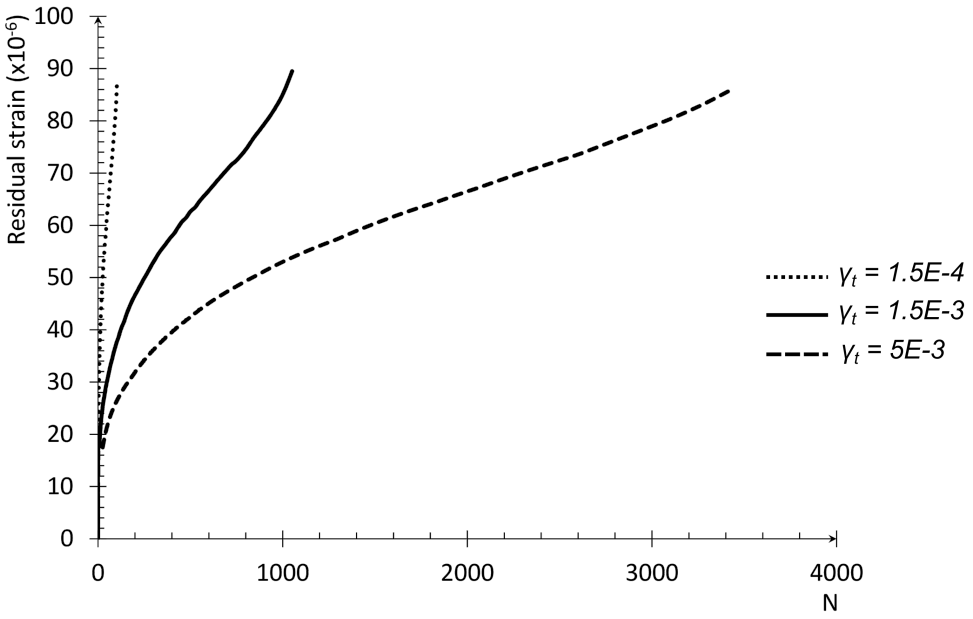

Figure 5.20: Effect of γ_t on the strain development.

5.5 Assessment of the capabilities of the unified model at the meso-scale

5.5.1 Description of the meso-scale model

The simplified meso-scale model is considered herein, in which the concrete is modelled as a two-phases material made of the cement matrix and the coarse aggregates. A prismatic concrete sample $50 \times 50 \times 50$ mm^3 is considered. A realistic reproduction of the sample is obtained through X-ray Computed Tomography (CT), as detailed in [50, 92, 212], in order to consider the real spatial distribution of the aggregates inside the concrete sample. The reconstructed solid model out of the real sample is shown in Figure 5.21. The meso-scale analyses are expected to be advantageous because they allow for the consideration of local confinement effects, that arise due to the interaction between the different phases, when the specimen is subjected to compressive loads. Coarse aggregates of nominal diameter bigger than 5 mm are explicitly modeled. They are assigned elastic

properties of $E = 60000$ MPa and $\nu = 0.22$. By doing so, the properties of the finer aggregates are averaged with those of the cement matrix, with an expected negligible error. The specific material behaviour illustrated at Section 3 has been used for the cement matrix, and has been implemented in a UMAT subroutine. The plastic damage and fatigue parameters are reported in Table 5.8, while the creep parameters are reported in Table 5.9.

E (MPa)	ν	f_c (MPa)	f_t (MPa)	e	t_s	κ_{1D}	q_{h0}	A	B	κ_{c0}	
33000	0.2	34.6	3.05	0.55	0.01	0.00005	0.4	-2.22	-3.46	0.015	
A_c	B_c	$\omega_{c,max}$	κ_{t0}	A_t	B_t	$\omega_{t,max}$	s_0	G_f (J/m^2)	w_c (mm)	a	γ_t
1	100	0.95	0.0001	1	0.4	0.95	0.2	25	1	0.085	0.00001

Table 5.8:
Plastic damage and fatigue parameters for the cement matrix.

E (MPa)	ν –	m –	m_d –	t_0 (days)	f_c (MPa)	w/c –	a/c –	c (kg/m^3)	D (mm)	h –	t_{dry} (days)
33000	0.2	22	25	28	34.6	0.6	7	219	16.7	0.8	28

Table 5.9: Creep constitutive parameters for the cement matrix.

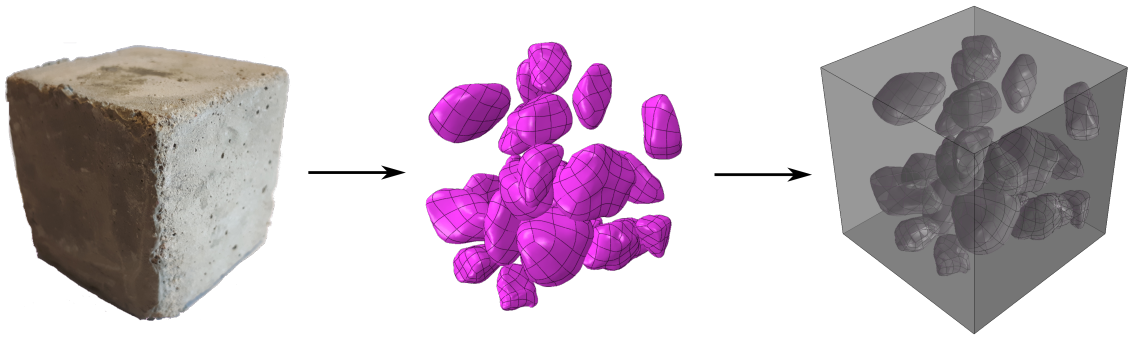

Figure 5.21: Meso-cale model of a cubic concrete specimen through X-ray CT.

5.5.2 Creep test

A creep test is performed at the meso-scale on a solid model of a real concrete specimen in order to evaluate the capabilities of the proposed model to simulate the non-linear creep characteristics

of concrete. The idea is to test the performance of the model to reproduce the three stage creep behaviour described in the introduction, by considering the physical interaction between the mortar and the aggregates.

The vertical compressive load is applied uniformly at the top surface of the concrete cube at 28 days, and kept constant for 20000 days. The model is isostatically constrained. Figure 5.22a shows the meso-scale model with its different phases (cement matrix and coarse aggregates), and the uniform compressive load (in red) applied at the top. Six different loading levels are taken into consideration. They are defined as a fraction η of the compressive strength f_c of the concrete sample. The loading levels that have been taken into consideration are the following: two low loading levels $\eta = 0.25$ and 0.35, two medium loading levels $\eta = 0.45$ and 0.55, and two high loading levels $\eta = 0.75$ and 0.85.

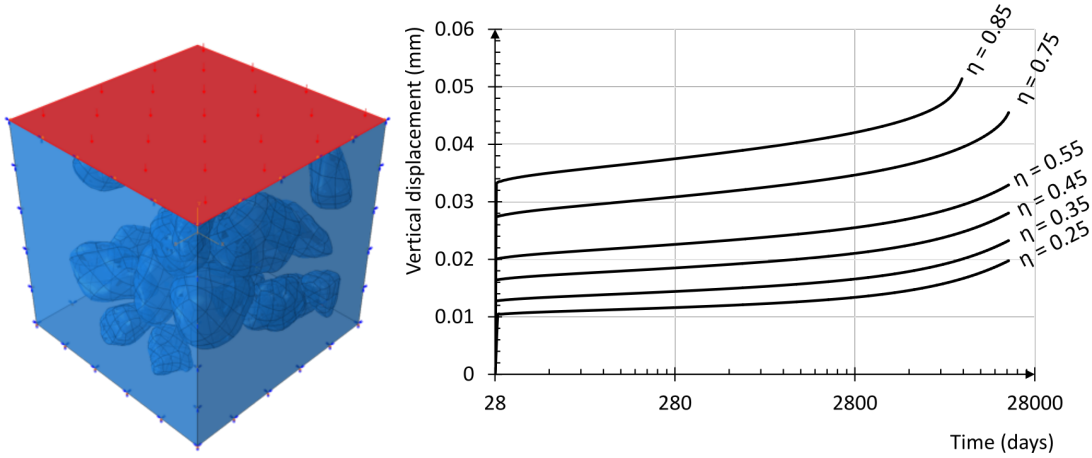

(a) (b)

Figure 5.22: Meso-scale solid model (a), and plot of the vertical displacement at the top surface of the concrete cube versus time (b).

The plots of the average displacement of the top surface of the cube versus time for each loading level are displayed in logarithmic scale in Figure 5.22b. For all loading levels it can be observed an initial fast increase in the vertical displacement due to the instantaneous vertical compressive load, which corresponds to the primary creep stage. Subsequently, the displacement increases almost at a constant rate for relatively low loading levels ($0.25f_c$ and $0.35f_c$), and for relatively medium loading

levels ($0.45f_c$ and $0.55f_c$). This accounts for the secondary creep stage. Finally, for relatively high loading levels, including $0.75f_c$ and $0.85f_c$, another fast increase is noticed, with subsequent failure in a very short time. This corresponds to the tertiary creep stage, which is usually observed for loading levels above $0.7f_c$ [41]. It can also be observed from Figure 5.22b that the total time from initial loading to failure decreases with increasing loading level.

In order to get an insight into the interaction between aggregates and cement matrix, reference is made to the equivalent plastic strain as a measure of the extent of plastic flow that the cement matrix undergoes due to the mechanical load. When the equivalent plastic strain is equal to zero, the cement matrix stress state lies in the elastic domain; on the other hand, positive values of the equivalent plastic strain indicate that the cement matrix has undergone plastic deformations.

The contour plot of the equivalent plastic strain on a section of the concrete sample model is shown in Figure 5.23 for medium and high loading levels. Specifically, Figure 5.23a depicts the plastic strain field immediately after the application of the instantaneous load; in Figure 5.23b at an intermediate time (corresponding to 10000 days medium loading levels, or half time between application of load and failure for high loading levels); in Figure 5.23c at the final time (corresponding to 20000 days for medium loading levels, or to the failure of the concrete specimen for high loading levels). It can be noted from Figure 5.23a that, for high loading levels, the plastic flow triggers immediately after the load application. This early formation of plastic zones in the concrete sample is responsible of the premature failure of the concrete specimen at high loading levels, as shown in Figure 5.22b. Further, the plastic zones initiate at the interface between aggregates and cement matrix, especially in regions where the aggregates are close to each other, as highlighted by the arrows in Figure 5.23a. In fact, in these zones the local confinement of the cement matrix, due to the interaction between the nearest aggregates, lead to stress concentrations in the matrix, hence to plastic deformations.

In Figure 5.23b it can be observed that the plastic zones initiate around the aggregates for the medium loading levels, while they grow bigger in regions around the aggregates and travel through the matrix for high loading levels. This behaviour can be explained by the strain mismatch due to creep deformations at the aggregate/cement matrix interface. In fact, on that interface

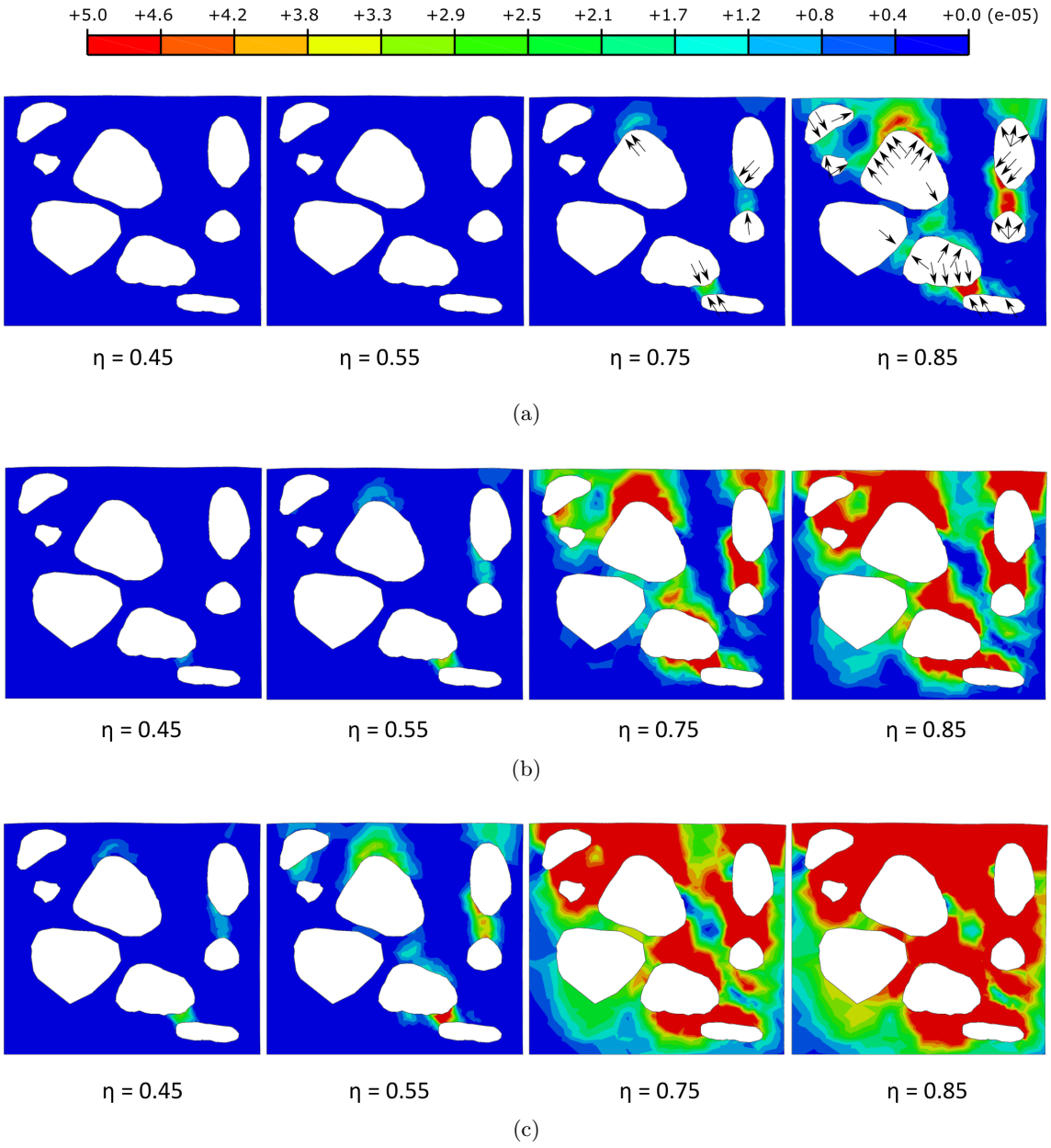

Figure 5.23: Contour plot of the equivalent plastic strain on section of the concrete sample immediately after the load application (a), at an intermediate step (b), and at the final step (c).

the stiffer aggregates oppose to the continuous deformation of the creeping mortar. These strain incompatibilities lead to increasing stresses in the cement matrix, with a subsequent enhancement

in the formation and propagation of plastic zones, especially around aggregates which are close to each other. The plastic regions can grow and finally merge into bigger ones. This explains how creep deformation can lead to the failure of concrete materials.

Finally, Figure 5.23c shows the distribution of the plastic zones for medium and high loading levels close to the end of the experiment. The high loading levels show almost complete failure of the sample, due to a widespread plastic region, while the evolution of plastic zones is relatively slow for medium loading levels. This can be explained by the rapid increase in creep deformation rates, as concrete enters into the tertiary creep stage when it is subjected to high loading levels. At this point the strain mismatch due to creep is enhanced between aggregates and cement matrix, so leading to a faster propagation of the plastic zones. For medium loading levels, the creep deformations are visible at the secondary stage, in which the creep rate is constant. Therefore, the strain incompatibilities due to creep are less relevant and the plastic zones grow accordingly.

The above-mentioned observations are supported by Figure 5.24, which presents the plot of the equivalent plastic strain versus time at a specific location of the concrete sample (zone A), where the plastic strains develop first. It can be noticed that the equivalent plastic strain grows in line with the expected creep rates, for the three different creep stages. Especially for medium loading levels, the equivalent plastic strain evolves at a constant rate, corresponding to the creep rate at the secondary creep stage. Differently, for high loading levels the equivalent plastic strain grows faster, and it increases exponentially with time, as concrete enters into the tertiary creep stage and approaches failure.

The results of the numerical tests at the mesoscale show evidence that the model is capable to account for the non-linear creep, which is not included in the B3 creep model, by considering the physical interaction at the interface of the mortar and the aggregates.

5.5.3 Fatigue test

A fatigue test is performed at the meso-scale, considering a vertical cyclic compressive load applied at the top of the concrete cube specimen. The minimum stress level was kept constant $\sigma_{min} = 5\% f_c$, and the frequency of the test is equal to 1 Hz. Two different maximum stress levels

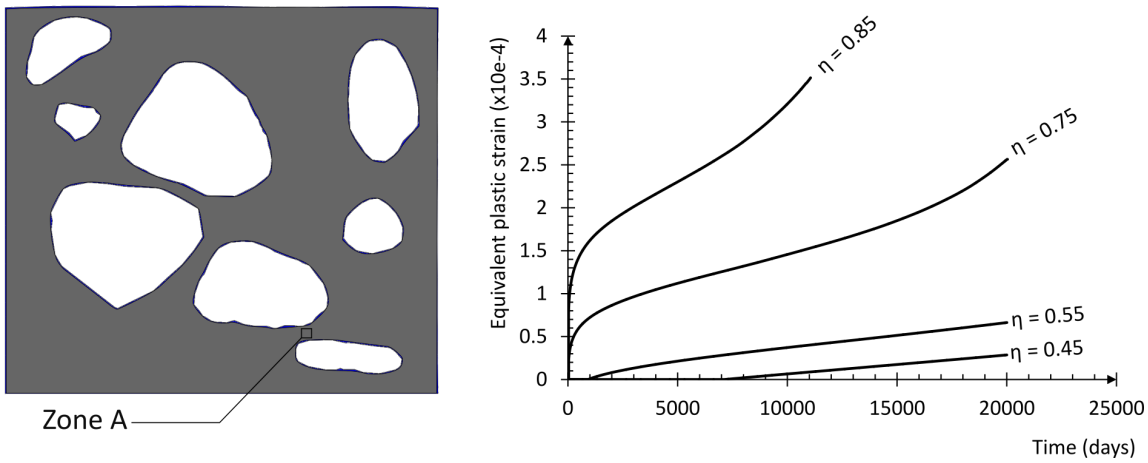

Figure 5.24: Plot of the equivalent plastic strain in Zone A versus time in days for medium and high loading levels.

are considered: $\sigma_{max} = 40\% f_c$, and $\sigma_{max} = 75\% f_c$. As in the creep test, the model is isostatically constrained. Fig. 5.25 depicts the vertical displacement at the top of the concrete cube versus the number of cycles of loading, for both the stress levels considered. In the case of the higher stress level, the number of cycles prior to failure is less than 1000, while in the case of the low stress level, this number is higher than 10 000, and failure has not occurred yet. According to the classification of Hsu et al. [14], the former falls into the LCF regime, while the latter falls into the HCF regime. In the LCF case, we can observed the three-stage pattern of the fatigue curve, in which the first and third stages last about 10 % of the whole life, while the second stage represents around 80 % of the fatigue life. In the HCF case, the displacement evolves very slowly, with a secondary strain rate which is very small compared to the LCF case.

The vertical displacement pattern observed can be explained, with a deeper insight at the meso-scale structure of the concrete cube. The contour plots of the equivalent plastic strain at different times are shown in Fig. 5.26, and Fig. 5.27 for $\sigma_{max} = 40\% f_c$, and $\sigma_{max} = 75\% f_c$ respectively. It can be seen that, the plastic strains tend to develop at the interfaces between the aggregates and the cement matrix, due to the local stress concentrations that arise in these zones. Then, they tend to grow and coalesce to occupy bigger zones in the specimen. The fatigue curve evolution in Fig. 5.25, is therefore explained by the progressive accumulation of plastic strains inside the material.

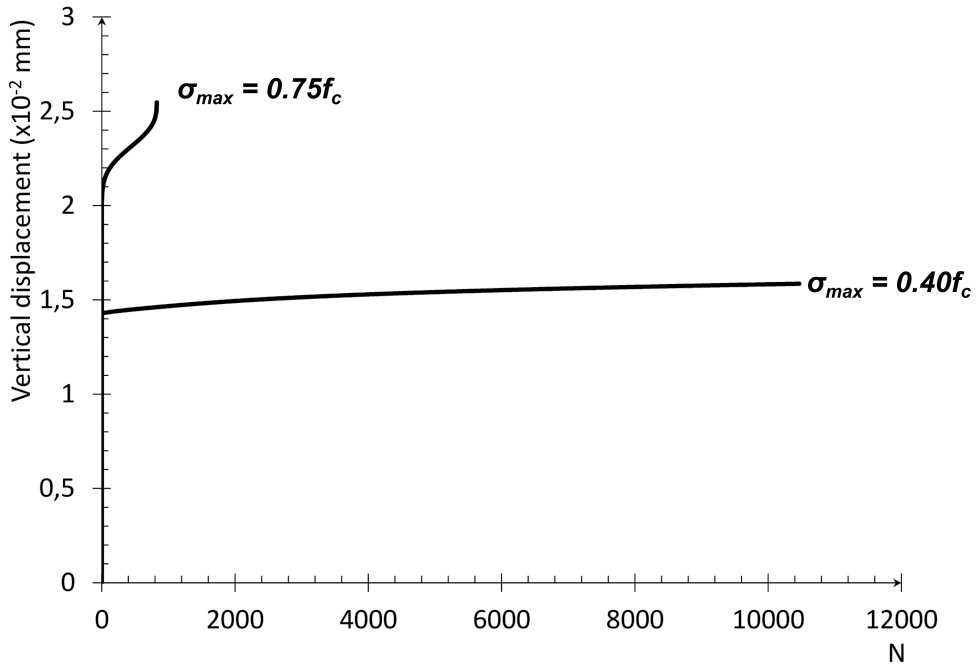

Figure 5.25: Vertical displacement at the top surface versus the number of cycles.

In the HCF case, it can be noted that, despite the concrete cube did not fail, internal plastic zones can somehow be observed inside the heterogeneous structure of the material. The plastic zones evolve slowly, a result which consistent with the small gradient of displacement observed during the second stage in Fig.5.25.

However, in the LCF case, a wide plastic zone can be observed only after 10 % for the fatigue life, which corresponds to approximately 80 cycles. Fig. 5.27 shows how the plastic zones evolve very fast, which is consistent with the higher slope of the fatigue curve during the second stage in Fig. 5.25. Then, the plastic zones coalesce, until occupying almost the full specimen, which corresponds to the third stage.

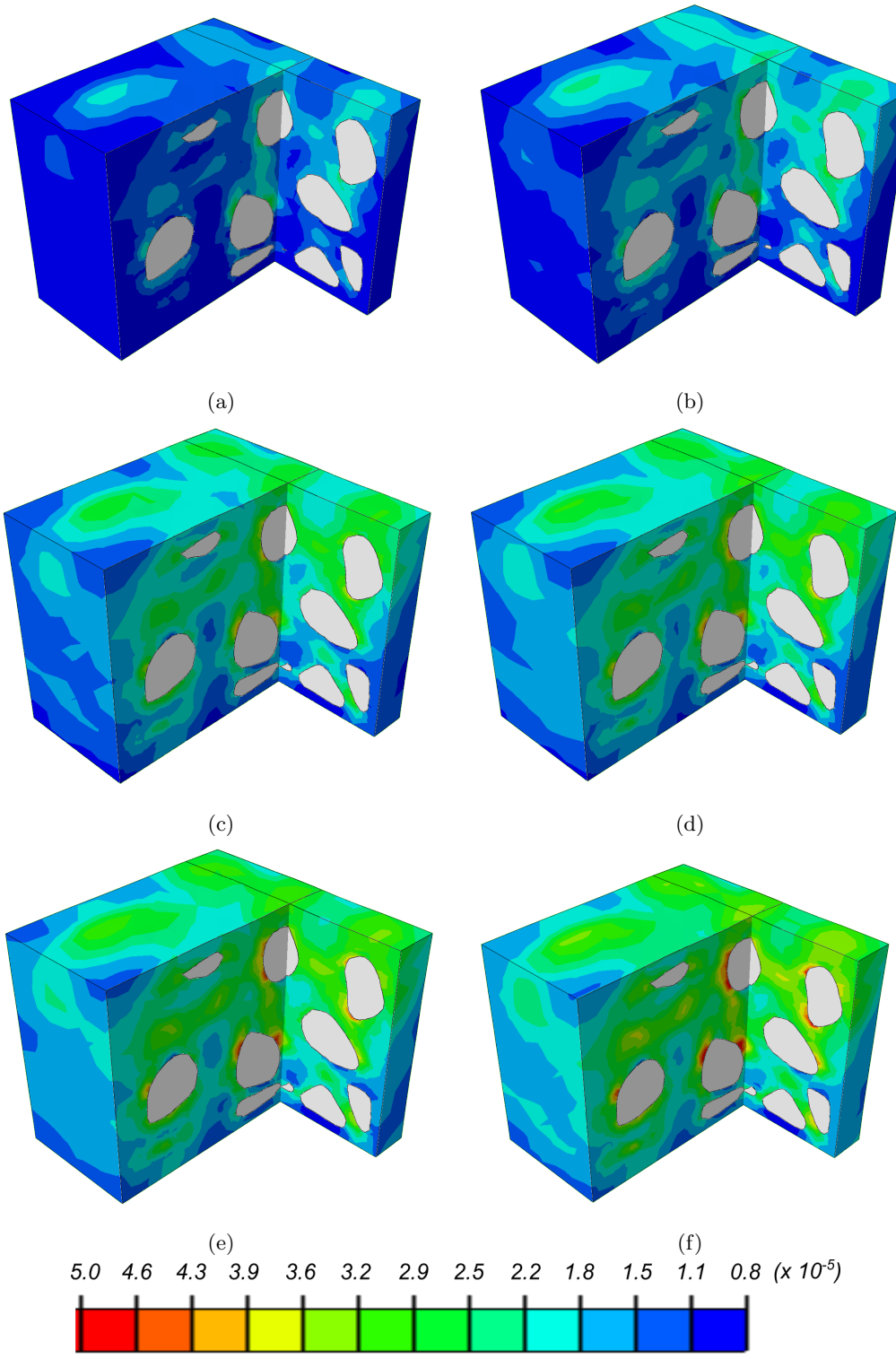

Figure 5.26: Equivalent plastic strain evolution in the sample at different times: at 10% (a), at 20% (b), 50% (c), 60% (d), 80% (e), 100% (f) of the total time for $\sigma_{max} = 40\% f_c$.

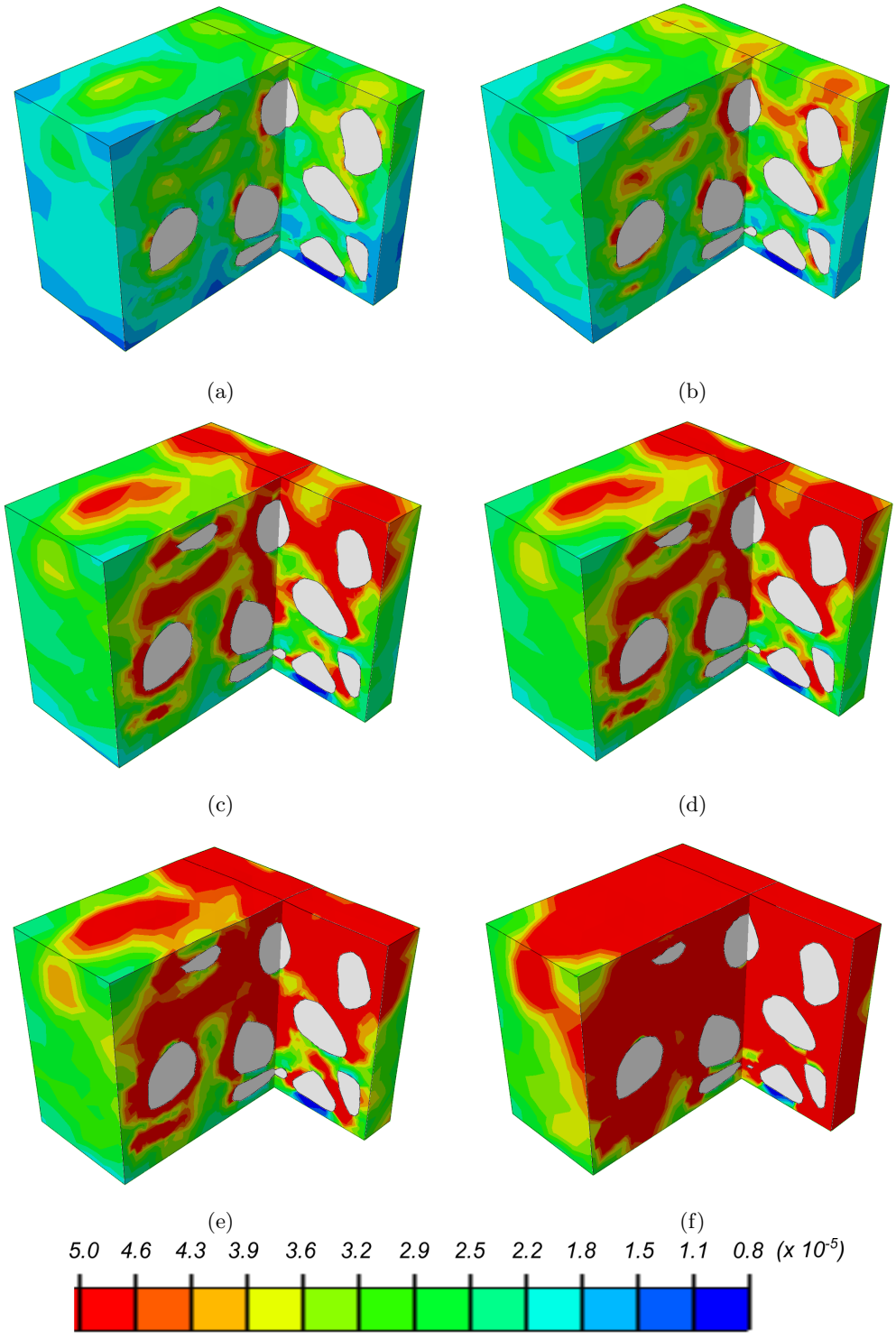

Figure 5.27: Equivalent plastic strain evolution in the sample at different times: at 10% (a), at 20% (b), 50% (c), 60% (d), 80% (e), 100% (f) of the total time for $\sigma_{max} = 75\% f_c$.

Chapter 6

Conclusions

The objective of the present work, was to build a plastic damage constitutive model for concrete, in order to to reproduce its non-linear mechanical behaviour when subjected to long-term and fatigue loadings. The main assumption at the basis of the model is that, the accumulation of inelastic strains is the physical mechanism responsible of the creep failure and fatigue degradation of concrete materials.

As a starting point, a literature review of existing plasticity models combined with the isotropic damage formulation was done. These models were unable to catch the mechanical response of concrete under cyclic loading with constant amplitude. Therefore, several attempts have been made to extend such models, in order to include a fatigue behaviour. A review of such models was done, and it came out the need to develop more comprehensive models for concrete materials that can account for creep and fatigue loadings in a unified manner.

The plastic formulation of the proposed model is based on a modified version of the Ménétrey-Willam failure surface, and the internal variable that controls the plastic flow is defined as the absolute value of the volumetric component of the plastic strain tensor. The damage formulation differentiates between the damage in tension and compression, and follows the scalar isotropic damage formulation of Mazars. The creep behaviour is taken into consideration by the phenomenological B3 model of Bažant. The physical micro-structural degradation due to fatigue is interpreted as a

gradual reduction of the size of the elastic domain as the number of cycles increase. To this aim, a modified version of the Ménétrey-Willam yield surface is proposed, in which a strength degradation function is included in its formulation to account for the effects of fatigue. This allows for plastic flow and damage accumulation, even for stress states initially below the yield surface.

Then, the numerical implementation of each component of the model and the coupling have been discussed. In particular the total stress can be subdivided into a plastic damage component and a creep component. The first component have been evaluated by means of the backward return-mapping algorithm, while the second component have been evaluated via the exponential algorithm. The mathematical expressions of the consistent elasto-plastic tangent operator and the coupled constitutive tangent operator have been derived. Then, a "return to apex" procedure has been implemented to deal with the non-convergence that may arise in case of extreme tensile loads.

Each component of the model have been calibrated and validated against experimental tests from the literature. In particular, then model was able to account for stiffness degradation and the strength loss under cyclic loadings. Furthermore, the model was able to catch the three-stage pattern observed experimentally, for concrete materials subjected to creep and fatigue loadings under multi-axial stress states.

Meso-scale analysis have been performed, in which the cement matrix and the coarse aggregates are differentiated. By performing creep tests at the meso-scale, the proposed model was able to account for the tertiary creep stage, due to an excessive accumulation of plastic strains at the interface between the creeping mortar and the stiffer aggregates, which is not present in the formulation of the B3 model. Furthermore, fatigue tests at the meso-scale have helped to get an insight in the local damaging process that occurs inside the complex heterogeneous structure, for both HCF and LCF regimes.

Although the presented model has shown good capabilities for describing the mechanical behavior of concrete under creep and fatigue loadings, it can still be improved, considering two main aspects. First, a more in-depth understanding of the physical mechanisms underlying the damage initiation and growth could require the consideration of the Interfacial Transition Zones (ITZ) in the meso-scale modeling of concrete. These zones, formed at the interface between aggregates and

mortar during setting, have a chemical composition similar to mortar, but with higher porosity. Therefore, they could be critical zones for the initiation and growth of damage inside the meso-structure of concrete. On the other hand, although the model described herein offers the possibility to track the evolution of plastic strains during cyclic fatigue loading, the conventional cycle-by-cycle integration scheme used to define the evolution of the plastic, damage and fatigue history variables, could be demanding in terms of computational effort. This is especially true for HCF, where millions of cycles can be observed prior to failure. Therefore, a more efficient simulation of concrete subjected to a very high number of cycles of load, would require optimization techniques, such as the cycle or the adaptive jump methods.

Bibliography

[1] F. Z. Kachkouch, C. C. Noberto, L. F. d. A. L. Babadopulos, A. R. S. Melo, A. M. L. Machado, N. Sebaibi, F. Boukhelf, and Y. El Mendili. "Fatigue behavior of concrete: A literature review on the main relevant parameters". In: *Construction and Building Materials* 338 (2022), p. 127510.

[2] K. Aas-Jakobsen. *Fatigue of concrete beams and columns*. Division of Concrete Structures, Norwegian Inst. of Technology, University . . ., 1970.

[3] B. Zhang, D. Phillips, and K. Wu. "Effects of loading frequency and stress reversal on fatigue life of plain concrete". In: *Magazine of concrete research* 48.177 (1996), pp. 361–375.

[4] B. Zhang, D. Phillips, and D. Green. "Sustained loading effect on the fatigue life of plain concrete". In: *Magazine of Concrete Research* 50.3 (1998), pp. 263–278.

[5] A. Khawas and K. B. Thapa. "Fatigue Damage Model in Plain Concrete Utilizing Damage Mechanics Theory". In: *Proceedings of IOE Graduate Conference*. 2016, pp. 147–154.

[6] N. Oneschkow, T. Timmermann, and S. Löhnert. "Compressive fatigue behaviour of high-strength concrete and mortar: Experimental investigations and computational modelling". In: *Materials* 15.1 (2022), p. 319.

[7] J. Zhang, W. Liu, Q. Zhu, and J. Shao. "A novel elastic–plastic damage model for rock materials considering micro-structural degradation due to cyclic fatigue". In: *International Journal of Plasticity* 160 (2023), p. 103496.

[8] J. Lemaitre and R. Desmorat. *Engineering damage mechanics: ductile, creep, fatigue and brittle failures*. Springer Science & Business Media, 2006.

[9] A. Caggiano, D. S. Schicchi, S. Yang, S. Harenberg, V. Malarics-Pfaff, M. Pahn, F. Dehn, and E. Koenders. "A microscale approach for modelling concrete fatigue damage-mechanisms". In: *Key Engineering Materials*. Vol. 827. Trans Tech Publ. 2020, pp. 73–78.

[10] M. Thiele and S. Pirskawetz. "Analysis of damage evolution in concrete under fatigue loading by acoustic emission and ultrasonic testing". In: *Materials* 15.1 (2022), p. 341.

[11] J. McCall. "Probability of fatigue failure of plain concrete". In: *Journal Proceedings*. Vol. 55. 8. 1958, pp. 233–244.

[12] H. K. Hilsdorf. "Fatigue strength of concrete under varying flexural stresses". In: *Journal Proceedings*. Vol. 63. 10. 1966, pp. 1059–1076.

[13] K. Raju. "Prediction of the fatigue life of plain concrete in compression". In: *Building Science* 4.2 (1969), pp. 99–102.

[14] T. T. Hsu. "Fatigue of plain concrete". In: *Journal Proceedings*. Vol. 78. 4. 1981, pp. 292–305.

[15] B. Isojeh, M. El-Zeghayar, and F. J. Vecchio. "Concrete damage under fatigue loading in uniaxial compression". In: *ACI Mater. J* 114.2 (2017), pp. 225–235.

[16] B. Isojeh, M. El-Zeghayar, and F. J. Vecchio. "Simplified constitutive model for fatigue behavior of concrete in compression". In: *Journal of Materials in Civil Engineering* 29.7 (2017), p. 04017028.

[17] K. Keerthana and J. C. Kishen. "An experimental and analytical study on fatigue damage in concrete under variable amplitude loading". In: *International Journal of Fatigue* 111 (2018), pp. 278–288.

[18] L. Lei, S. Xingang, C. Yunhua, W. Lefan, and Y. Xiangcheng. "A new fatigue damage model for pavement concrete beams bearing multi-level bending loads". In: *Plos one* 16.8 (2021), e0255048.

[19] O. Omidi and V. Lotfi. "Finite element analysis of concrete structures using plasticdamage model in 3-D implementation". In: *International Journal of Civil Engineering* 8.3 (2010), pp. 187–203.

[20] J. Lee and G. L. Fenves. "Plastic-damage model for cyclic loading of concrete structures". In: *Journal of engineering mechanics* 124.8 (1998), pp. 892–900.

[21] J. Lubliner, J. Oliver, S. Oller, and E. Oñate. "A plastic-damage model for concrete". In: *International Journal of solids and structures* 25.3 (1989), pp. 299–326.

[22] I. D. Karsan and J. O. Jirsa. "Behavior of concrete under compressive loadings". In: *Journal of the Structural Division* 95.12 (1969), pp. 2543–2564.

[23] V. Gopalaratnam and S. P. Shah. "Softening response of plain concrete in direct tension". In: *Journal Proceedings*. Vol. 82. 3. 1985, pp. 310–323.

[24] O. Omidi and V. Lotfi. "Numerical analysis of cyclically loaded concrete under large tensile strains by the plastic-damage model". In: (2010).

[25] P. Grassl and M. Jirásek. "Damage-plastic model for concrete failure". In: *International journal of solids and structures* 43.22-23 (2006), pp. 7166–7196.

[26] G. Etse and K. Willam. "Fracture energy formulation for inelastic behavior of plain concrete". In: *Journal of engineering mechanics* 120.9 (1994), pp. 1983–2011.

[27] P. Grassl, D. Xenos, U. Nyström, R. Rempling, and K. Gylltoft. "CDPM2: A damage-plasticity approach to modelling the failure of concrete". In: *International Journal of Solids and Structures* 50.24 (2013), pp. 3805–3816.

[28] J. Y. Wu, J. Li, and R. Faria. "An energy release rate-based plastic-damage model for concrete". In: *International journal of Solids and Structures* 43.3-4 (2006), pp. 583–612.

[29] J. Faleiro, S. Oller, and A. Barbat. "Plastic–damage seismic model for reinforced concrete frames". In: *Computers & structures* 86.7-8 (2008), pp. 581–597.

[30] X. Xue and X. Yang. "A damage model for concrete under cyclic actions". In: *International Journal of Damage Mechanics* 23.2 (2014), pp. 155–177.

[31] J. Liang, X. Ren, and J. Li. "A competitive mechanism driven damage-plasticity model for fatigue behavior of concrete". In: *International Journal of Damage Mechanics* 25.3 (2016), pp. 377–399.

[32] A. Sarikaya and R. Erkmen. "A plastic-damage model for concrete under compression". In: *International Journal of Mechanical Sciences* 150 (2019), pp. 584–593.

[33] D. Lu, F. Meng, X. Zhou, G. Wang, and X. Du. "Double Scalar Variables Plastic-Damage Model for Concrete". In: *Journal of Engineering Mechanics* 148.2 (2022).

[34] V. M. Kindrachuk, M. Thiele, and J. F. Unger. "Constitutive modeling of creep-fatigue interaction for normal strength concrete under compression". In: *International Journal of Fatigue* 78 (2015), pp. 81–94.

[35] J. Marigo. "Modelling of brittle and fatigue damage for elastic material by growth of microvoids". In: *Engineering Fracture Mechanics* 21.4 (1985), pp. 861–874.

[36] A. Alliche. "Damage model for fatigue loading of concrete". In: *International Journal of Fatigue* 26.9 (2004), pp. 915–921.

[37] S. H. Mai, F. Le-Corre, G. Forêt, and B. Nedjar. "A continuum damage modeling of quasi-static fatigue strength of plain concrete". In: *International Journal of Fatigue* 37 (2012), pp. 79–85.

[38] S. P. Shah and S. Chandra. "Fracture of concrete subjected to cyclic and sustained loading". In: *Journal Proceedings*. 10. 1970.

[39] G. Kim, G. Loreto, J.-Y. Kim, K. E. Kurtis, J. J. Wall, and L. J. Jacobs. "In situ nonlinear ultrasonic technique for monitoring microcracking in concrete subjected to creep and cyclic loading". In: *Ultrasonics* 88 (2018), pp. 64–71.

[40] Y. Li, S. Qiang, W. Xu, X. Hua, C. Xu, J. Lai, M. Yuan, and B. Chen. "Verification of concrete nonlinear creep mechanism based on meso-damage mechanics". In: *Construction and Building Materials* 276 (2021), p. 122205.

[41] P. Yu, R. Li, D. Bie, X. Yao, X. Liu, and Y. Duan. "A coupled creep and damage model of concrete considering rate effect". In: *Journal of Building Engineering* 45 (2022), p. 103621.

[42] C. Mazzotti and M. Savoia. "Nonlinear creep, Poisson's ratio, and creep-damage interaction of concrete in compression". In: *Materials Journal* 99.5 (2002), pp. 450–457.

[43] J. Saliba, F. Grondin, M. Matallah, A. Loukili, and H. Boussa. "Relevance of a mesoscopic modeling for the coupling between creep and damage in concrete". In: *Mechanics of Time-dependent Materials* 17.3 (2013), pp. 481–499.

[44] Z. Kammouna, M. Briffaut, and Y. Malecot. "Mesos-copic simulations of concrete strains incompatibilities under high creep stress level and consequences on the mechanical properties". In: *European Journal of Environmental and Civil Engineering* 23.7 (2019), pp. 879–893.

[45] X. Ren, Q. Wang, R. Ballarini, and X. Gao. "Coupled creep-damage-plasticity model for concrete under long-term loading". In: *Journal of Engineering Mechanics* 146.5 (2020), p. 04020027.

[46] G. Mazzucco, G. Xotta, B. Pomaro, V. A. Salomoni, and F. Faleschini. "Elastoplastic-damaged meso-scale modelling of concrete with recycled aggregates". In: *Composites Part B: Engineering* 140 (2018), pp. 145–156.

[47] T. Titscher. "Efficient computational meso-scale modeling of concrete under cyclic loading". In: (2019).

[48] L. Contri, C. Maiorana, and B. Schrefler. "A structural inhomogeneous material model for concrete at early ages". In: *Colloque Internationale sur le beton jeune, International Conference on Concrete at early ages-invited paper*. Ed. Anciens ENPC. 1982, pp. 203–213.

[49] L. Contri, C. Maiorana, and B. Schrefler. "Numerical formulation of a multiphase composite material model for concrete". In: *Colloque International sur le beton jeune, Session VI, Modelisation du developpment des proprietes du beton*. Vol. 2. 1983, pp. 198–213.

[50] G. Mazzucco, B. Pomaro, G. Xotta, E. Garbin, C. Majorana, N. De Marchi, and G. Concheri. "Meso-scale XCT-based modeling of ordinary concrete". In: *Construction and Building Materials* 286 (2021), p. 122850.

[51] P. Menetrey and K. Willam. "Triaxial failure criterion for concrete and its generalization". In: *Structural Journal* 92.3 (1995), pp. 311–318.

[52] G. Pijaudier-Cabot and J. Mazars. "Damage models for concrete". In: *Jean Lemaitre Handbook of Materials Behavior Models* 2 (2001), pp. 500–512.

[53] Z. P. Bažant and S. Baweja. "Creep and shrinkage prediction model for analysis and design of concrete structures: Model B3*". In: *ACI Special Publications* 194 (2000), pp. 1–84.

[54] K. Raithby and J. Galloway. "Effects of moisture condition age, and rate of loading on fatigue of plain concrete". In: *Special Publication* 41 (1974), pp. 15–35.

[55] D. Zhao, Q. Chang, and J. Yang. "Analysis for factors affecting fatigue behavior of concrete". In: *Journal of Building Structures. J. Build. Struct* 29 (2008), pp. 102–105.

[56] N. Oneschkow. "Influence of loading frequency on the fatigue behaviour of highstrength concrete". In: *Proceedings of the 9th FIB International PhD Symposium in Civil Engineering. July 22nd to 25th* (2012), pp. 235–240.

[57] N. Oneschkow. "Fatigue behaviour of high-strength concrete with respect to strain and stiffness". In: *International Journal of Fatigue* 87 (2016), pp. 38–49.

[58] R. Lenschow. "Long term random dynamic loading of concrete structures". In: *Matériaux et Construction* 13 (1980), pp. 274–278.

[59] N. Oneschkow, T. Scheiden, M. Hüpgen, C. Rozanski, and M. Haist. "Fatigue-induced damage in high-strength concrete microstructure". In: *Materials* 14.19 (2021), p. 5650.

[60] G. L. Golewski. "The Phenomenon of Cracking in Cement Concretes and Reinforced Concrete Structures: The Mechanism of Cracks Formation, Causes of Their Initiation, Types and Places of Occurrence, and Methods of Detection—A Review". In: *Buildings* 13.3 (2023), p. 765.

[61] E. W. Bennett. "Fatigue in concrete". In: *Concrete; G.B.; DA.* 8 (1974), pp. 43–45.

[62] S.-Q. Yang, P. Ranjith, Y.-H. Huang, P.-F. Yin, H.-W. Jing, Y.-L. Gui, and Q.-L. Yu. "Experimental investigation on mechanical damage characteristics of sandstone under triaxial cyclic loading". In: *Geophysical Journal International* 201.2 (2015), pp. 662–682.

[63] C. Otto, K. Elsmeier, and L. Lohaus. "Temperature Effects on the Fatigue Resistance of High-Strength-Concrete and High-Strength-Grout". In: *High Tech Concrete: Where Technology and Engineering Meet: Proceedings of the 2017 fib Symposium, held in Maastricht, The Netherlands, June 12-14, 2017*. Springer. 2018, pp. 1401–1409.

[64] G. Petkovic. "Properties of concrete related to fatigue damage with emphasis on high-strength concrete." In: (1993).

[65] X. Ren, X. Wei, and R. Ballarini. "A temporal multiscale model for fatigue damage of concrete". In: *Journal of Engineering Mechanics* 148.3 (2022), p. 04021163.

[66] R. C. 36-RDL. "Long term random dynamic loading of concrete structures". In: *Mater Struct* 17.1 (1984), pp. 1–28.

[67] C. U. Grosse, M. Ohtsu, D. G. Aggelis, and T. Shiotani. *Acoustic emission testing: Basics for research–applications in engineering*. Springer Nature, 2021.

[68] T. Scheiden, N. Oneschkow, S. Löhnert, and R. Patel. "Acoustic emission due to fatigue damage mechanisms in high-strength concrete with different aggregates". In: *Advances in Engineering Materials, Structures and Systems: Innovations, Mechanics and Applications*. CRC Press, 2019, pp. 1491–1496.

[69] R. H. Faraj, H. U. Ahmed, and A. F. H. Sherwani. "Fresh and mechanical properties of concrete made with recycled plastic aggregates". In: *Handbook of sustainable concrete and industrial waste management*. Elsevier, 2022, pp. 167–185.

[70] J. O. Holmen. "Fatigue of concrete by constant and variable amplitude loading". In: *Special Publication* 75 (1982), pp. 71–110.

[71] M. Thiele. "Experimentelle Untersuchung und Analyse der Schädigungsevolution in Beton unter hochzyklischen Ermüdungsbeanspruchungen". PhD thesis. Bundesanstalt für Materialforschung und-prüfung (BAM), 2016.

[72] A. Mehmel and E. Kern. *Elastische und plastische Stauchungen von Beton infolge Druckschwell- und Standbelastung*. Deutscher Ausschuss für Stahlbeton. Schriftenreihe, Heft. Ernst, 1962.

[73] R. Tepfers. "Tensile fatigue strength of plain concrete". In: *Journal Proceedings*. Vol. 76. 8. 1979, pp. 919–934.

[74] C. E.-I. du Béton. *CEB-FIP model code 1990: Design code*. Thomas Telford Publishing, 1993.

[75] P. Code. "Eurocode 2: design of concrete structures-part 1–1: general rules and rules for buildings". In: *British Standard Institution, London* 668 (2005), pp. 659–668.

[76] T. T. Hsu. "Fatigue and microcracking of concrete". In: *Materiaux et construction* 17.1 (1984), pp. 51–54.

[77] Q. Zhang and L. Wang. "Investigation of stress level on fatigue performance of plain concrete based on energy dissipation method". In: *Construction and Building Materials* 269 (2021), p. 121287.

[78] A. Mehmel. "Investigations on the effect of frequently repeated stress on the elasticity under compression and the compressive strength of concrete". In: *Institut fuer Benton und Eisenbeton an der Technischen Hochschule, Verlag Julius Springer, Berlin* 74 (1926).

[79] O. Graf and E. Brenner. "Experiments for investigating the resistance of concrete under often repeated compression loads". In: *Bulletin* 1 (1934), pp. 17–25.

[80] M. Awad and H. Hilsdorf. "Strength and deformation characteristics of plain concrete subjected to high repeated and sustained loads (University of Illinois, Urbana)". In: *College of Engineering, University of Illinois at Urbana-Champaign* (1971).

[81] K. Furtak. "Ein verfahren zur berechnung der betonfestigkeit unter schwellenden belastungen". In: *Cement and Concrete Research* 14.6 (1984), pp. 855–865.

[82] P. Desayi, K. Sundara Raja lyengar, and T. Sanjeeva Reddy. "Stress-strain characteristics of concrete confined in steel spirals under repeated loading". In: *Matériaux et Construction* 12 (1979), pp. 375–383.

[83] S. P. Shah, A. Fafitis, and R. Arnold. "Cyclic loading of spirally reinforced concrete". In: *Journal of Structural Engineering* 109.7 (1983), pp. 1695–1710.

[84] O. Buyukozturk and T.-M. Tseng. "Concrete in biaxial cyclic compression". In: *Journal of Structural Engineering* 110.3 (1984), pp. 461–476.

[85] T. T. Hooi. "Effects of passive confinement on fatigue properties of concrete". In: *Magazine of Concrete Research* 52.1 (2000), pp. 7–15.

[86] A. Taliercio and E. Gobbi. "Experimental investigation on the triaxial fatigue behaviour of plain concrete". In: *Magazine of concrete research* 48.176 (1996), pp. 157–172.

[87] Y.-p. Song, W. Cao, and X.-h. Meng. "Fatigue properties of plain concrete under triaxial constant-amplitude tension-compression cyclic loading". In: *Journal of Shanghai University (English Edition)* 9 (2005), pp. 127–133.

[88] H. Wang and Y. Song. "Fatigue capacity of plain concrete under fatigue loading with constant confined stress". In: *Materials and structures* 44 (2011), pp. 253–262.

[89] R. Tepfers, J. Görlin, and T. Samuelsson. "Concrete Subjected to pulsating load and pulsating deformation of different pulse waveform". In: *Nordisk betong* 17.4 (1973).

[90] K. Raithby and A. Whiffin. "Failure of plain concrete under fatigue loading-a review of current knowledge". In: (1968).

[91] A. Baktheer, J. Hegger, and R. Chudoba. "Enhanced assessment rule for concrete fatigue under compression considering the nonlinear effect of loading sequence". In: *International Journal of Fatigue* 126 (2019), pp. 130–142.

[92] G. Mazzucco, B. Pomaro, G. Xotta, V. A. Salomoni, and C. E. Majorana. "An efficient geometric reconstruction of meso-scale concrete structures accounting for confinement sce-

narios". In: *International Journal for Multiscale Computational Engineering* 18.1 (2020), pp. 129–139.

[93] G. Mazzucco, B. Pomaro, G. Xotta, E. Garbin, V. Salomoni, and N. De Marchi. "Experimental and Numerical Characterization of Normal-Weight Concrete at the Mesoscale". In: *Journal of Materials in Civil Engineering* 34.7 (2022), p. 04022121.

[94] A. Wöhler. *Über die festigkeitsversuche mit eisen und stahl*. Ernst & Korn, 1870.

[95] M. Lee and B. Barr. "An overview of the fatigue behaviour of plain and fibre reinforced concrete". In: *Cement and Concrete Composites* 26.4 (2004), pp. 299–305.

[96] A. Palmgren. "Die lebensdauer von kugellargern". In: *Zeitshrift des Vereines Duetsher Ingenieure* 68.4 (1924), p. 339.

[97] M. A. Miner. "Cumulative damage in fatigue". In: (1945).

[98] L. Elfgren. *Fatigue Capacity of Concrete Structures: Assessment of Railway Bridges*. Luleå tekniska universitet, 2015.

[99] T. Eljufout, H. Toutanji, and M. Al-Qaralleh. "Fatigue Stress-Life Model of RC Beams Based on an Accelerated Fatigue Method". In: *Infrastructures* 4.2 (2019), p. 16.

[100] E. Papa and A. Taliercio. "Anisotropic damage model for the multiaxial static and fatigue behaviour of plain concrete". In: *Engineering Fracture Mechanics* 55.2 (1996), pp. 163–179.

[101] I. M. Vega, M. A. Bhatti, and W. A. Nixon. "A non-linear fatigue damage model for concrete in tension". In: *International Journal of Damage Mechanics* 4.4 (1995), pp. 362–379.

[102] F. Richart and N. Newmark. "An hypothesis for the determination of cumulative damage in fatigue". In: *Selected Papers By Nathan M. Newmark: Civil Engineering Classics*. ASCE. 1948, pp. 279–312.

[103] J. Kommers. "The effect of overstress in fatigue on the endurance life of steel". In: *Proceedings-American Society For Testing And Materials*. Vol. 45. Amer Soc Testing Materials 100 Barr Harbor Dr, W Conshohocken, Pa 19428-2959. 1945, pp. 532–541.

[104] J. Bennett. "A study of the damaging effect of fatigue stressing on x4130-steel". In: *Proceedings-American Society For Testing And Materials*. Vol. 46. Amer Soc Testing Materials 100 Barr Harbor Dr, W Conshohocken, Pa 19428-2959. 1946, pp. 693–714.

[105] A. M. Freudenthal. "Physical and statistical aspects of cumulative damage". In: *Colloquium on Fatigue/Colloque de Fatigue/Kolloquium über Ermüdungsfestigkeit*. Springer. 1956, pp. 53–62.

[106] A. M. Freudenthal and R. A. Heller. "On stress interaction in fatigue and a cumulative damage rule". In: *Journal of the Aerospace Sciences* 26.7 (1959), pp. 431–442.

[107] A. Fatemi and L. Yang. "Cumulative fatigue damage and life prediction theories: a survey of the state of the art for homogeneous materials". In: *International journal of fatigue* 20.1 (1998), pp. 9–34.

[108] K. J. Willam. "Constitutive model for the triaxial behaviour of concrete". In: *Proc. Intl. Assoc. Bridge Structl. Engrs* 19 (1975), pp. 1–30.

[109] P. H. Feenstra and R. De Borst. "A composite plasticity model for concrete". In: *International journal of solids and structures* 33.5 (1996), pp. 707–730.

[110] H. D. Kang. *Triaxial constitutive model for plain and reinforced concrete behavior*. University of Colorado at Boulder, 1997.

[111] P. Grassl, K. Lundgren, and K. Gylltoft. "Concrete in compression: a plasticity theory with a novel hardening law". In: *International Journal of Solids and Structures* 39.20 (2002), pp. 5205–5223.

[112] G. Mazzucco, B. Pomaro, V. A. Salomoni, and C. E. Majorana. "Apex control within an elasto-plastic constitutive model for confined concretes". In: *Mathematics and Computers in Simulation* 162 (2019), pp. 221–232.

[113] K. Løland. "Continuous damage model for load-response estimation of concrete". In: *Cement and Concrete research* 10.3 (1980), pp. 395–402.

[114] J. Mazars. “A description of micro-and macroscale damage of concrete structures”. In: *Engineering Fracture Mechanics* 25.5-6 (1986), pp. 729–737.

[115] J. Mazars and G. Pijaudier-Cabot. “Continuum damage theory—application to concrete”. In: *Journal of engineering mechanics* 115.2 (1989), pp. 345–365.

[116] V. Lubarda, D. Krajcinovic, and S. Mastilovic. “Damage model for brittle elastic solids with unequal tensile and compressive strengths”. In: *Engineering Fracture Mechanics* 49.5 (1994), pp. 681–697.

[117] X. Huang, C. Chen, G. Chen, and M. Liu. “Analysis of deformation and failure of polymer-bonded explosives using coupled plastic damage model”. In: *Proceedings of the 20th International Conference on Composite Materials*. 2015.

[118] H. W. Reinhardt. “Fracture mechanics of an elastic softening material like concrete”. In: *Heron, 29 (2), 1984* (1984).

[119] C. Mazzotti and M. Savoia. “Nonlinear creep damage model for concrete under uniaxial compression”. In: *Journal of engineering mechanics* 129.9 (2003), pp. 1065–1075.

[120] N. Challamel, C. Lanos, and C. Casandjian. “Creep damage modelling for quasi-brittle materials”. In: *European Journal of Mechanics-A/Solids* 24.4 (2005), pp. 593–613.

[121] R. Pedersen, A. Simone, and L. Sluys. “An analysis of dynamic fracture in concrete with a continuum visco-elastic visco-plastic damage model”. In: *Engineering fracture mechanics* 75.13 (2008), pp. 3782–3805.

[122] F. Gatuingt and G. Pijaudier-Cabot. “Coupled damage and plasticity modelling in transient dynamic analysis of concrete”. In: *International journal for numerical and analytical methods in geomechanics* 26.1 (2002), pp. 1–24.

[123] J. Cheng, X. Qian, and T. Zhao. “Rheological viscoplastic models of asphalt concrete and rate-dependent numerical implement”. In: *International Journal of Plasticity* 81 (2016), pp. 209–230.

[124] Q. Hu, L. Yun-Gui, and L. Xilin. "A Elastic Plastic Damage Model for Concrete Considering Strain Rate Effect and Stiffness Damping". In: *International Conference on Theoretical and Mathematical Foundations of Computer Science*. Springer. 2011, pp. 425–429.

[125] L. Pereira, J. Weerheijm, and L. Sluys. "A new rate-dependent stress-based nonlocal damage model to simulate dynamic tensile failure of quasi-brittle materials". In: *International Journal of Impact Engineering* 94 (2016), pp. 83–95.

[126] X. Ren and J. Li. "A unified dynamic model for concrete considering viscoplasticity and rate-dependent damage". In: *International Journal of Damage Mechanics* 22.4 (2013), pp. 530–555.

[127] G. Hervé, F. Gatuingt, and A. Ibrahimbegović. "On numerical implementation of a coupled rate dependent damage-plasticity constitutive model for concrete in application to high-rate dynamics". In: *Engineering Computations* (2005).

[128] K. P. Fathima and J. C. Kishen. "A thermodynamic framework for the evolution of damage in concrete under fatigue". In: *Archive of Applied Mechanics* 85 (2015), pp. 921–936.

[129] F. Liu and J. Zhou. "Research on fatigue strain and fatigue modulus of concrete". In: *Advances in Civil Engineering* 2017 (2017).

[130] C. von der Haar and S. Marx. "A strain model for fatigue-loaded concrete". In: *Structural Concrete* 19.2 (2018), pp. 463–471.

[131] B.-T. Huang, Q.-H. Li, and S.-L. Xu. "Fatigue deformation model of plain and fiber-reinforced concrete based on Weibull function". In: *Journal of Structural Engineering* 145.1 (2019), p. 04018234.

[132] D. Pfanner. *Zur Degradation von Stahlbetonbauteilen unter Ermüdungsbeanspruchung*. VDI-Verlag, 2003.

[133] J. Gruenberg, J. Goehlmann, and S. Marx. "Mechanical Models for concrete failure under monotonically increasing as well as cyclic multiaxial loading". In: *Beton-Und Stahlbetonbau* 109.6 (2014), pp. 405–418.

[134] T. Pfister, Y. Petryna, and F. Stangenberg. “Damage modelling of reinforced concrete under multi-axial fatigue loading”. In: *Computational Modelling of Concrete Structures*. CRC Press, 2020, pp. 421–429.

[135] V. S. Kolluru and P. S. Surendra. “Biaxial Tension Fatigue Response of Concrete [J]”. In: *Cement and Concrete Composite* 25.5 (2003), pp. 617–623.

[136] Z. P. Bazant and M. H. Hubler. “Theory of cyclic creep of concrete based on Paris law for fatigue growth of subcritical microcracks”. In: *Journal of the Mechanics and Physics of Solids* 63 (2014), pp. 187–200.

[137] S. Seitl, T. Thienpont, and W. De Corte. “Fatigue crack behaviour: comparing three-point bend test and wedge splitting test data on vibrated concrete using Paris’ law”. In: *Frattura ed Integrità Strutturale* 39 (2017), pp. 110–117.

[138] P. Miarka, S. Seitl, V. Bılek, and H. Cifuentes. “Assessment of fatigue resistance of concrete: SN curves to the Paris’ law curves”. In: *Construction and Building Materials* 341 (2022), p. 127811.

[139] Z. P. Bazant and K. Xu. “Size effect in fatigue fracture of concrete”. In: *ACI Materials Journal* 88.4 (1991), pp. 390–399.

[140] D. Renju and M. Keerthy. “A review on fatigue life prediction of plain concrete”. In: *IOP Conference Series: Materials Science and Engineering*. Vol. 936. 1. IOP Publishing. 2020, p. 012026.

[141] K. Kirane and Z. P. Bažant. “Size effect in Paris law for quasibrittle materials analyzed by the microplane constitutive model M7”. In: *Mechanics Research Communications* 68 (2015), pp. 60–64.

[142] A. Daneshyar and M. Ghaemian. “Coupling microplane-based damage and continuum plasticity models for analysis of damage-induced anisotropy in plain concrete”. In: *International Journal of Plasticity* 95 (2017), pp. 216–250.

[143] E. Papa. "A damage model for concrete subjected to fatigue loading". In: *European journal of mechanics. A. Solids* 12.3 (1993), pp. 429–440.

[144] R. Faria, J. Oliver, and M. Cervera. "A strain-based plastic viscous-damage model for massive concrete structures". In: *International journal of solids and structures* 35.14 (1998), pp. 1533–1558.

[145] M. Seyedi, R. Desmorat, and J. Sermage. "A two scale model for thermo-mechanical high cycle fatigue failure". In: *European Conference on Fracture ECF*. Vol. 15. 2004.

[146] R. Desmorat. "Damage and fatigue: continuum damage mechanics modeling for fatigue of materials and structures". In: *Revue européenne de génie civil* 10.6-7 (2006), pp. 849–877.

[147] R. Desmorat, A. Kane, M. Seyedi, and J. P. Sermage. "Two scale damage model and related numerical issues for thermo-mechanical high cycle fatigue". In: *European Journal of Mechanics-A/Solids* 26.6 (2007), pp. 909–935.

[148] E. a. d. t. Bei, z. druckschwellversuchen zyklischen, and e. überblick ein. "Influencing factors on the temperature development in cyclic compressive fatigue tests: An overview". In: *Otto-Graf-Journal* 19 (2020).

[149] Y. F. Dafalias and E. P. Popov. "Cyclic loading for materials with a vanishing elastic region". In: *Nuclear engineering and design* 41.2 (1977), pp. 293–302.

[150] B.-L. Yang, Y. F. Dafalias, and L. R. Herrmann. "A bounding surface plasticity model for concrete". In: *Journal of Engineering Mechanics* 111.3 (1985), pp. 359–380.

[151] W.-F. Chen and D.-J. Han. *Plasticity for structural engineers*. J. Ross publishing, 2007.

[152] M. N. Fardis, B. Alibe, and J. L. Tassoulas. "Monotonic and cyclic constitutive law for concrete". In: *Journal of engineering mechanics* 109.2 (1983), pp. 516–536.

[153] M. Ortiz. "A constitutive theory for the inelastic behavior of concrete". In: *Mechanics of materials* 4.1 (1985), pp. 67–93.

[154] M. N. Fardis and E.-S. Chen. "A cyclic multiaxial model for concrete". In: *Computational mechanics* 1.4 (1986), pp. 301–315.

[155] W. Suaris, C. Ouyang, and V. M. Fernando. "Damage model for cyclic loading of concrete". In: *Journal of engineering mechanics* 116.5 (1990), pp. 1020–1035.

[156] G. Z. Voyiadjis and T. M. Abu-Lebdeh. "Plasticity model for concrete using the bounding surface concept". In: *International Journal of Plasticity* 10.1 (1994), pp. 1–21.

[157] A. Pandolfi and A. Taliercio. "Bounding surface models applied to fatigue of plain concrete". In: *Journal of engineering Mechanics* 124.5 (1998), pp. 556–564.

[158] P. Lü, Q. Li, and Y. Song. "Damage constitutive of concrete under uniaxial alternate tension–compression fatigue loading based on double bounding surfaces". In: *International journal of solids and structures* 41.11-12 (2004), pp. 3151–3166.

[159] M. Rahimi, D. Chan, and A. Nouri. "Bounding surface constitutive model for cemented sand under monotonic loading". In: *International Journal of Geomechanics* 16.2 (2016), p. 04015049.

[160] C. Wen, S. Yazdani, Y. J. Kim, and M. Abdulrahman. "Bounding surface approach to the modeling of anisotropic fatigue damage in woven fabric composites". In: *Open Journal of Composite Materials* 2.04 (2012), p. 125.

[161] I. N. Yadav and K. B. Thapa. "Fatigue damage model of concrete materials". In: *Theoretical and Applied Fracture Mechanics* 108 (2020), p. 102578.

[162] Z. P. Bazant. "Microplane model for strain-controlled inelastic behaviour". In: *Unknown Host Publication Title*. John Wiley & Sons, 1984, pp. 45–59.

[163] G. I. Taylor. "Plastic strain in metals". In: *J. Inst. Metals* 62 (1938), pp. 307–324.

[164] F. C. Caner and Z. P. Bažant. "Microplane model M7 for plain concrete. I: Formulation". In: *Journal of Engineering Mechanics* 139.12 (2013), pp. 1714–1723.

[165] Z. P. Bažant and B. H. Oh. "Crack band theory for fracture of concrete". In: *Matériaux et construction* 16.3 (1983), pp. 155–177.

[166] Z. P. Bazant and B. H. Oh. "Microplane model for fracture analysis of concrete structures". In: *Proceeding of Symposium on the Interaction of Non-Nuclear Munitions with Structures*. 1983, pp. 49–53.

[167] Z. P. Bažant and P. C. Prat. "Microplane model for brittle-plastic material: I. Theory". In: *Journal of Engineering Mechanics* 114.10 (1988), pp. 1672–1688.

[168] Z. P. Bažant, Y. Xiang, and P. C. Prat. "Microplane model for concrete. I: Stress-strain boundaries and finite strain". In: *Journal of Engineering Mechanics* 122.3 (1996), pp. 245–254.

[169] Z. P. Bažant, F. C. Caner, I. Carol, M. D. Adley, and S. A. Akers. "Microplane model M4 for concrete. I: Formulation with work-conjugate deviatoric stress". In: *Journal of Engineering Mechanics* 126.9 (2000), pp. 944–953.

[170] F. C. Caner and Z. P. Bažant. "Microplane model M4 for concrete. II: Algorithm and calibration". In: *Journal of engineering mechanics* 126.9 (2000), pp. 954–961.

[171] I. Zreid and M. Kaliske. "Regularization of microplane damage models using an implicit gradient enhancement". In: *International Journal of Solids and Structures* 51.19-20 (2014), pp. 3480–3489.

[172] I. Zreid, C. Steinke, and M. Kaliske. "Gradient Enhanced Microplane Models for Concrete". In: *Bauingenieur* 92 (2017), pp. 87–95.

[173] B. R. Indriyantho, I. Zreid, and M. Kaliske. "Finite strain extension of a gradient enhanced microplane damage model for concrete at static and dynamic loading". In: *Engineering Fracture Mechanics* 216 (2019), p. 106501.

[174] N. H. Nguyen, H. H. Bui, J. Kodikara, S. Arooran, and F. Darve. "A discrete element modelling approach for fatigue damage growth in cemented materials". In: *International Journal of Plasticity* 112 (2019), pp. 68–88.

[175] A. Elkadi and J. Van Mier. "Experimental investigation of size effect in concrete fracture under multiaxial compression". In: *International journal of fracture* 140 (2006), pp. 55–71.

[176] Z. Gyurkó, K. Bagi, and A. Borosnyói. "Discrete Element Modelling of uniaxial compression test of hardened concrete." In: *Epitoanyag-Journal of Silicate Based & Composite Materials* 66.4 (2014).

[177] J. Suchorzewski, J. Tejchman, and M. Nitka. "Discrete element method simulations of fracture in concrete under uniaxial compression based on its real internal structure". In: *International Journal of Damage Mechanics* 27.4 (2018), pp. 578–607.

[178] S. Hentz, L. Daudeville, and F.-V. Donzé. "Discrete element modeling of a reinforced concrete structure". In: *Journal of the Mechanical Behavior of Materials* 19.4 (2009), pp. 249–258.

[179] J. Chen, L.-b. Wang, and X.-m. Huang. "Micromechanical modeling of asphalt concrete fracture using a user-defined three-dimensional discrete element method". In: *Journal of Central South University* 19.12 (2012), pp. 3595–3602.

[180] T. Ma, Y. Zhang, Y. Zhao, and X. Huang. "Simulation of four-point bending beam fatigue test of asphalt mixture using PFC3D". In: *CICTP 2015*. 2015, pp. 1016–1027.

[181] W. Shiu, F. Donzé, and L. Daudeville. "Missile impact on a concrete slab: a 3D discrete element study". In: (2005).

[182] W. Shiu, F. V. Donze, and L. Daudeville. "Discrete element modelling of missile impacts on a reinforced concrete target". In: *International Journal of Computer Applications in Technology* 34.1 (2009), pp. 33–41.

[183] S. Sinaie, T. D. Ngo, and V. P. Nguyen. "A discrete element model of concrete for cyclic loading". In: *Computers & structures* 196 (2018), pp. 173–185.

[184] N. H. Nguyen, H. H. Bui, G. D. Nguyen, J. Kodikara, S. Arooran, and P. Jitsangiam. "A thermodynamics-based cohesive model for discrete element modelling of fracture in cemented materials". In: *International Journal of Solids and Structures* 117 (2017), pp. 159–176.

[185] G. Cusatis, D. Pelessone, and A. Mencarelli. "Lattice discrete particle model (LDPM) for failure behavior of concrete. I: Theory". In: *Cement and Concrete Composites* 33.9 (2011), pp. 881–890.

[186] J. J. Smith and J. E. Bishop. *A comparison of the lattice discrete particle method to the finite-element method and the K&C material model for simulating the static and dynamic response of concrete.* Tech. rep. Sandia National Lab.(SNL-NM), Albuquerque, NM (United States), 2013.

[187] Z. Zhu, M. Pathirage, W. Wang, M. Troemner, and G. Cusatis. "Lattice discrete particle modeling of concrete under cyclic tension–compression with multi-axial confinement". In: *Construction and Building Materials* 352 (2022), p. 128985.

[188] Y. Gan, H. Zhang, M. Liang, E. Schlangen, K. van Breugel, and B. Šavija. "A numerical study of fatigue of hardened cement paste at the microscale". In: *International Journal of Fatigue* 151 (2021), p. 106401.

[189] P. Carrara, M. Ambati, R. Alessi, and L. De Lorenzis. "A framework to model the fatigue behavior of brittle materials based on a variational phase-field approach". In: *Computer Methods in Applied Mechanics and Engineering* 361 (2020), p. 112731.

[190] J. Červenka and V. K. Papanikolaou. "Three dimensional combined fracture–plastic material model for concrete". In: *International journal of plasticity* 24.12 (2008), pp. 2192–2220.

[191] J. A. Paredes, S. Oller, and A. H. Barbat. "New tension-compression damage model for complex analysis of concrete structures". In: *Journal of Engineering Mechanics* 142.10 (2016), p. 04016072.

[192] B. Y. Bahn and C.-T. T. Hsu. "Stress-strain behavior of concrete under cyclic loading". In: *Materials Journal* 95.2 (1998), pp. 178–193.

[193] M. Jirásek and P. Grassl. "Evaluation of directional mesh bias in concrete fracture simulations using continuum damage models". In: *Engineering Fracture Mechanics* 75.8 (2008), pp. 1921–1943.

[194] C. A. Coronado and M. M. Lopez. "Numerical modeling of concrete-FRP debonding using a crack band approach". In: *Journal of Composites for Construction* 14.1 (2010), pp. 11–21.

[195] Y. He and W. Fan. "Plastic-Damage Cap Model with Crack Closure Behavior for Concrete Modeling". In: *Journal of Engineering Mechanics* 148.11 (2022), p. 04022067.

[196] Z. P. Bažant and M. Jirásek. *Creep and hygrothermal effects in concrete structures*. Vol. 38. Springer, 2018.

[197] A. Committee. "Building code requirements for structural concrete (ACI 318-08) and commentary". In: American Concrete Institute. 2008.

[198] F. I. du Béton. "International Federation for Structural Concrete Special Activity Group New Model Code". In: *Lausanne: International Federation for Structural Concrete* (2012).

[199] Z. Bažant, R. Wendner, and M. Hubler. "Model B4 for concrete creep including multi-decade prediction: Description and application". In: *RILEM–Materials and Structures* (2014).

[200] L. Dohnalová and P. Havlásek. "Comparison of drying shrinkage and drying creep kinetics in concrete". In: *Acta Polytechnica CTU Proceedings* 15 (2018), pp. 12–19.

[201] Z. P. Bažant and W. P. Murphy. "Creep and shrinkage prediction model for analysis and design of concrete structures-model B3". In: *Matériaux et Constructions* 28.180 (1995), pp. 357–365.

[202] H. Cornelissen and G. Timmers. "Fatigue of plain concrete in uniaxial tension and in alternating tension-compression experiment and results". In: *Report Stevin Laboratory, Concrete Structures 5-81-7* (1981).

[203] J. C. Simo and R. L. Taylor. "Consistent tangent operators for rate-independent elastoplasticity". In: *Computer Methods in Applied Mechanics and Engineering* 48.1 (1985), pp. 101–118.

[204] E. A. de Souza Neto, D. Peric, and D. R. Owen. *Computational methods for plasticity: theory and applications*. John Wiley & Sons, 2011.

[205] Q. Yu, Z. P. Bažant, and R. Wendner. "Improved algorithm for efficient and realistic creep analysis of large creep-sensitive concrete structures". In: *ACI Structural Journal* 109.5 (2012), p. 665.

[206] I. Carol and Z. P. Bažant. "Viscoelasticity with aging caused by solidification of nonaging constituent". In: *Journal of Engineering Mechanics* 119.11 (1993), pp. 2252–2269.

[207] D. Simulia. "Abaqus Software Documentation (Version 6.14). Providence, Rhode Island". In: *US* (2014).

[208] I. Imran and S. J. Pantazopoulou. "Experimental study of plain concrete under triaxial stress". In: *ACI Materials Journal-American Concrete Institute* 93.6 (1996), pp. 589–601.

[209] M. Jirásek and P. Havlásek. "Accurate approximations of concrete creep compliance functions based on continuous retardation spectra". In: *Computers & Structures* 135 (2014), pp. 155–168.

[210] N. Ranaivomanana, S. Multon, and A. Turatsinze. "Basic creep of concrete under compression, tension and bending". In: *Construction and Building Materials* 38 (2013), pp. 173–180.

[211] L. Yin. "Fatigue damage of concrete under uniaxial compression". In: *2018 7th International Conference on Energy and Environmental Protection (ICEEP 2018)*. Atlantis Press. 2018, pp. 933–936.

[212] G. Mazzucco, B. Pomaro, G. Xotta, C. E. Maiorana, and V. A. Salomoni. "Tomography reconstruction of concrete materials for meso-scale modelling". In: *Engineering Computations* 37.7 (2020), pp. 2275–2291.